Transport Properties of Lateral Spin Valves

Georgios Konstantinos Stefanou

University of Leeds

School of Physics and Astronomy

Submitted in accordance with the requirements for the degree of

Doctor of Philosophy

August 2017

Intellectual Property Statement

The candidate confirms that the work submitted is his own and that appropriate credit has been given where reference has been made to the work of others.

Acknowledgements

Thanks everyone! I thought I could keep that as my punchline anyway. There are so many people that helped me during these four years that I'll end up writing a very good book of names that people could use in the case they can't decide a name for their baby or pet..

First of all I'd like to thank my supervisors Prof. Bryan J. Hickey and Dr. Gavin Burnell for putting up with me and my "habit" of always being late (that includes deadlines, meeting times, reports and experiments! Well done me)! Another big thank you to my supervisors for opening a bag of ideas every time I would get stack with my experiments or the interpretation of my results. The discussions on designing new experiments and how to properly analyse most of my data as well as the really motivational enthusiasm are things that helped me move forward. I'd like to personally thank Dr. Gavin Burnell for one more thing. The One Code. Basically 90% of the lab's computers are using lab view and the One Code that Dr. Burnell developed, in order to record our experimental data.

I don't think there is a word I could use to thank Dr. Mannan Ali and Ben Steele as much as feel I should. The reason why, is not only for being around in the labs and offer a helping hand when needed (or not needed!), but also for being there for me in my personal life, whenever a had a problem or just for some drinks, good food and music suggestions!

Talking about food, chocolate was my fuel for the last months.. A huge thanks to Benedikt Boehm for introducing me to (product placement) Ragusa chocolate! That really broaden my horizons on the world of chocolate. I could never thank enough every single person that when going to Switzerland would bring be back some! Dr Fatma Al'Ma Mari, Matt Rogers, Katie Moran, Kowsar Sahbazi and Dr Katharina Zeissler! Fatma, Kowsar and Katharina, I'll never forget the "motivational" photos of you eating Ragusa (a piece per day..) to make me write faster so that you won't eat the "submitting the thesis" prize! To be honest it kind of worked.

My office mates for these four years, Dr Priya Sinha, Dr Rowan Temple, Charles Spencer, Dr Dong Shi, Franz Herling, Matt Vaughan and Greg Simon! All the discussions at random moments in the office were very therapeutic to me whenever I could really do anything but writing or just

complaining about my suicidal devices.

I would also like to thank Dr Joe Batley and Dr James Witt for their help (and patience). For taking me from the hand with every single step in the cleanroom fabrication, sample deposition, bonding a device and finally the actual measurements. Their help was precious for the current project.

The analysis of large amount of files was a bit of a problem, since python should be used for that (or one more year of work..)!Dr Rowan Temple and Katie Moran really saved me with their knowledge on programming and their infinite patience when I kept asking them to help me with the python code! Thanks a million for that.. I know, I need to properly learn python!

Moreover, I owe a huge thank you to Ben Steele, Amy Westerman, Fatma Al'Ma Mari, Katharina Zeissler, Rowan Temple, Risalat Khan, Robert Buda, Katie Moran, Greg Simon, Nicolas Peters and Craig Knox for helping me calm down and relax through discussions, jokes or even pranks (and of course the supply of chocolate!) when things would get difficult. Take care guys...

Furthermore, I want to thank all people from SpinIcur, as the meetings were not only about science but for some social life events as well! Benedikt Boehm, Salvatore Mesoraca, Simon Knudde, Andre Bisig, Thomas Wagner and the rest of the people of the group! Thank you so much for the good and fun times guys!

A huge amount of help was given to me by the members of the Mechanical, Electronic and Cryogenic workshop. In particular John Turton, Brian Gibbs and Luke Bone for never saying no to my continuous requests on cryogenics for the cryostats, Richard Oliver for the design and built of the PCB and Brian Gibbs along with Trevor Haynes for the built of the low temperature sample holder. Dr Mannan Ali contributed in the wiring of the transport stick and the sample holder.

I was given a lot of courage from people outside the uni as well. My family was always helping me by supporting and advising me. My amazing friends Georgios T. and Manolis S. as they were always willing to listen to my rants when things would go south. Elena and Vasilis, for saving my mental health with our Fridays (kind of..)!

Finally, Vaso, for being next to me in every step of mine, I can't thank you enough.

I'm sure I've missed some of you guys and I'm sorry about that! :)

Abstract

The current study is focused on the investigation of the spin and heat properties of a Permalloy/silver/Permalloy, Permalloy/silver (doped with Iron)/Permalloy and Vanadium/silver/Vanadium spin valves in a lateral geometry. The presence of a downturn in the spin-signal of these lateral spin valves at low temperatures, below 30 K, can be avoided by depositing the Ag at a faster rate. This will promote a better microstructure that seems to have a crucial role in systems with very low or no magnetic impurities. A small part of the report is dedicated to test the two different behaviours of the spin signal that have been suggested in the literature, in the case of spin transport through an oxidised normal metal channel. According to literature, it would either remove the downturn of the spin signal at low temperatures, or form one. Our devices exhibited no downturn below 30 K, but by oxidising them, did not lead to the creation of it.

By doping the normal metal channel with a dust layer of magnetic impurities (MIL) one would expect that by increasing scattering centres the spin signal and spin diffusion length would decrease no matter where the MIL would be. Interestingly that was not confirmed, as not only the spin signal and diffusion length vary depending on the position of the MIL in the NM channel, but also in the occasion of the device where the MIL was place right in the middle of the NM channel. At temperatures above 70 K the spin signal presented was bigger than that of the reference device. Moreover, the spin diffusion length presented in the particular set of devices, exceeded that of the reference set of devices for temperatures higher than 140 K.

Finally, thermal effects were also expected to get picked up during the measurements as in order to create the spin accumulation, a charge current of 500 μ A is driven through the resistive Permalloy injector. That would give rise to Joule heating and Peltier effect once it reaches the Permalloy/silver junction due to the mismatch of the Peltier coefficients. Heat would then diffuse along the silver channel and through the substrate and would be detected in the second silver/Permalloy junction. The latter acted as a thermocouple and due to the difference in their Seebeck coefficients the temperature difference that was picked up, was converted to potential

difference.

The Scanning Thermal Microscopy technique was employed to image these effects. Based on the results of the technique, an analytical model that can predict the injector and detector junction temperature increase from that of the substrate was developed. In addition to that, since the voltage output is proportional to the product of the effective Seebeck coefficient with the temperature difference, the detector voltage could be predicted. To test the model a simple system of V/Ag/V device was used to deconvolute the thermal effects avoiding having a spin accumulation in the detector signal. After that, the thermal effects arising in a Py/Ag/Py lateral spin valve were investigated.

Finally, since the Peltier effect was present in the measurements, the non-local resistance, spin signal and baseline resistance were analysed as a function of current direction to find a so far not studied effect. There was a splitting in the non-local and baseline resistance across all different devices that had temperature and current dependence. To confirm that the effect was not an artefact, three cryostats, three transport sticks, two sample holders and two more systems (Py/Cu/Py and CoFe/Cu/CoFe) were studied.

Contents

List of Figures

List of Tables

Abbreviations

AC	Alternating Current	DC	Direct Current
AP	Antiparallel	P	Parallel
DOS	Density of States	δlayer	Delta layer
ECP	Electrochemical Potential	EBL	Electron Beam Lithography
FWHM	Full Width Half Maximum	FM	Ferromagnet
IPA	Isopropyl Alcohol	IL	Impurities Layer
LOR	Lift Off Resist	MR	Magnetoresistance
MMA	Methyl Methacrylate	MI	Magnetic Impurity
PMMA	Polymethyl Methacrylate	NLIV	Non-local IV
NM	Normal Metal	NLSV	Non-local Spin Valve
PCB	Printed Circuit Board	SEM	Scanning Electron Microscopy
SC	Superconductor	SThM	Scanning Thermal Microscopy
UHV	Ultra High Vacuum	VTI	Variable Temperature Insert

Chapter 1

Introduction

This PhD study is focused on two different, but also connected, subjects. These are the spin and heat transport effects measured during the transport measurements using the lateral spin valve geometry. The first one is related to the improvement of the spin signal by growing better material (chapter 4). Furthermore, the spin transport properties are analysed by introducing a dusting layer of magnetic impurities at different vertical positions of the normal metal channel (chapter 6). The second one is related to the heat transport in lateral spin valves (chapter 5). In the same chapter, the thermal properties are also analysed with respect to the applied charge current direction, related to the Peltier effect.

In the second chapter of this study, there is an introduction to the spin dependent phenomena, as well as generation and detection of the pure spin current, according to the literature accompanied with some of the basic equations for the spin diffusion length and the spin signal.

The third chapter is the methods and the techniques used for the measurements and characterisation of the samples and devices.

The fourth chapter is the first main experimental results part. The chapter is split into two sections. The first one is the characterisation of Ag films using X-rays and electron transport measurements. The reason why, is to aid the understanding of the second part which is based on the analysis of the spin transport properties in Ag, when two different deposition rates had been used for the growth of the NM channel.

The fifth chapter is related to the heat transport in the same NM. The Joule heating and the Peltier effect arise in the non-local measurements due the way that the pure spin currents are generated. In the chapter is analysed the generation, propagation and detection of these effects. Moreover, since the Peltier effect is linear to the applied current, that means that depending on the direction of the applied charge current, the heating output should differ. We analyse the non-local IVs as a function of current sign, to find that the Peltier term presents a new behaviour below 30 K that has not been reported in the literature so far.

The sixth chapter which is the last experimental chapter, is related to the spin transport properties in the NM when doped with magnetic impurities. Widely in literature, studies are focused on finding where do the impurities enter the spin valve system from. The difference here, is that we study the behaviour of the spin transport by deliberately doping the NM channel with a dusting layer of magnetic impurities at

different horizontal positions.

The seventh chapter is the last in the thesis and is the conclusions withdrawn from the three experimental chapters.

All the samples that were fabricated by the author had Permalloy (Py) as the ferromagnetic (FM) material, and Silver (Ag) as the normal metal (NM) channel. The reason why these specific materials were chosen, is related to the phenomenon that was planned to study. Py is a very well studied material in the literature and thus its magnetic behaviour could be predicted. On the other hand, since a big part of the study is devoted to spin and heat transport, Ag was the ideal candidate because it presents a very high spin diffusion length and the highest thermal conductivity amongst the normal metals.

All devices were fabricated in the Electronic and Electrical Engineering cleanroom (Wolfson cleanroom nanotechnology) whereas the active part of the devices and the films were deposited using an ultra high vacuum (UHV) evaporator in the department of physics. The X-ray measurements and transport measurements were conducted in the department of physics whereas the scanning electron microscopy (SEM) imaging was conducted in the EEE. The scanning thermal microscopy imaging (SThM) was performed in IBM Zürich by Dr. F. Menges.

Finally, in the duration of the PhD, 3 papers were published the data of which are not included in the thesis as they were not related. The first two "Polyhedral iron oxide core-shell nanoparticles in a biodegradable polymeric matrix: Preparation, characterization and application in magnetic particle hyperthermia and drug delivery" by M. Filippousi et al. and "Tunable AC magnetic hyperthermia efficiency of Ni ferrite nanoparticles" by Stefanou et al. are about magnetic nanoparticles used as hyperthermia agents. The author of the thesis performed the magnetic and hyperthermia characterisation of the samples in both papers. The last one "Achiral tilted domain walls in perpendicularly magnetized nanowires" by Boehm et al. is about Co/Ni magnetic multilayers that were fabricated to nanowires to study domain walls. The author of the thesis grew and optimised the Co/Ni multilayer films and characterise them using X-rays and magnetometry.

Chapter 2

Theory

2.1 Introduction

This chapter is an introduction in the basic phenomena that govern the behaviour of the non-local spin valves. The spin transport electronics, spintronics for short [1–4], based on metals [5], are in particular research interest for various applications [6–11] that started with the pioneering experiments of A. Fert [12] and P. Grünberg [13]. The two groups independently observed a change in the electrical resistance of a multilayer structure in the presence of the magnetic field, related to relative magnetisation orientation of the ferromagnetic (FM) layers, interrupted by a normal metal (NM).

Since by taking advantage of the effect, read heads were created for hard discs and were commercialised within less than ten years from its discovery, a lot of experimental interest [14] was shown on this type of devices, focusing on four different areas. Those were:

- Generation of spin currents
- Transport of spin currents over long distances
- Detection of spin currents
- Manipulation of spin currents

Since charge current was being used in the electrical generation of the spin currents, thermal effects had an effect on the presented properties of the structures, particularly when scaling them down to nanostructures. The thermal properties of a structure are related to the individual materials used and their combinations. They turned important since excessive current densities could lead to electromigration [15], [16–18], or failure [19–21], of the device. The importance of other effects arise and those were:

- Thermal conductivity
- Seebeck effect and Thermopower
- Joule heating and the Peltier effect

All the above are important for the performance of a spintronic device and thus the understanding of the background theory that determines its behaviour is essential.

2.2 Spin currents

The lateral spin valves is a basic structure of spin injection, diffusion and detection device for pure spin currents [22], [23–26]. It consists of two ferromagnetic electrodes used as spin injector (F_1) and detector (F_2), that are bridged by a normal metal channel (NM), used as a spin transport channel. A spin polarised current is injected from the F_1 to the NM and out of the left side of the transport channel [27], depicted in figure 2.1. A spin accumulation is created in the vicinity of the F_1/NM interface that diffuses in both arms of the NM [28]. The second ferromagnet is there to detect the decaying spin accumulation as a potential difference between the F_2 and the NM.

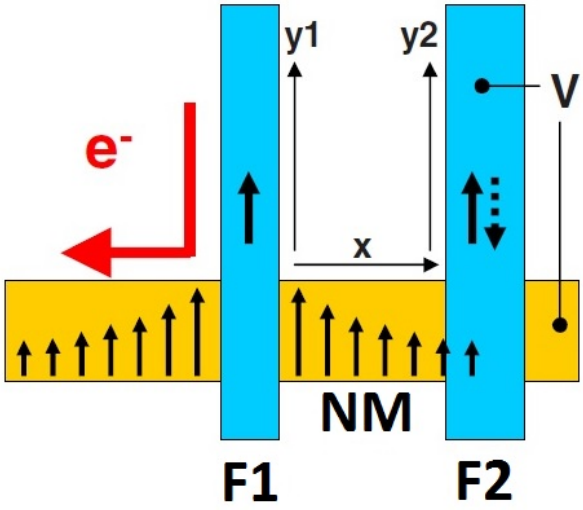

Figure 2.1: *Non-local spin valve and the current direction for the generation of the spin accumulation. F1 and F2 are the ferromagnetic injector and detector respectively, while NM is the normal metal channel, taken from [1]. The diffusion on the left-hand side of F1 is longer since it's a combination of the spin and drift current.*

The phenomenon is broken down in the next paragraphs for the spin current generation, accumulation, diffusion and detection.

2.2.1 Generation of spin currents

The ferromagnetic electrode presents a splitting between the energies for spin up and spin down electrons due to the exchange interaction. Those that are at the Fermi level will present different conduction properties. Since the electrons that are at the Fermi

level are those that carry the electric current, it means that the ferromagnet will present spin dependent electrical conductivity and so when a charge current flows through the F_1 it becomes spin polarised. Using the two current model [29], the spin polarisation in the ferromagnetic injector [30, 31] can be expressed as:

$$a_{FM} = \frac{\sigma_\uparrow - \sigma_\downarrow}{\sigma_\uparrow + \sigma_\downarrow} \tag{2.1}$$

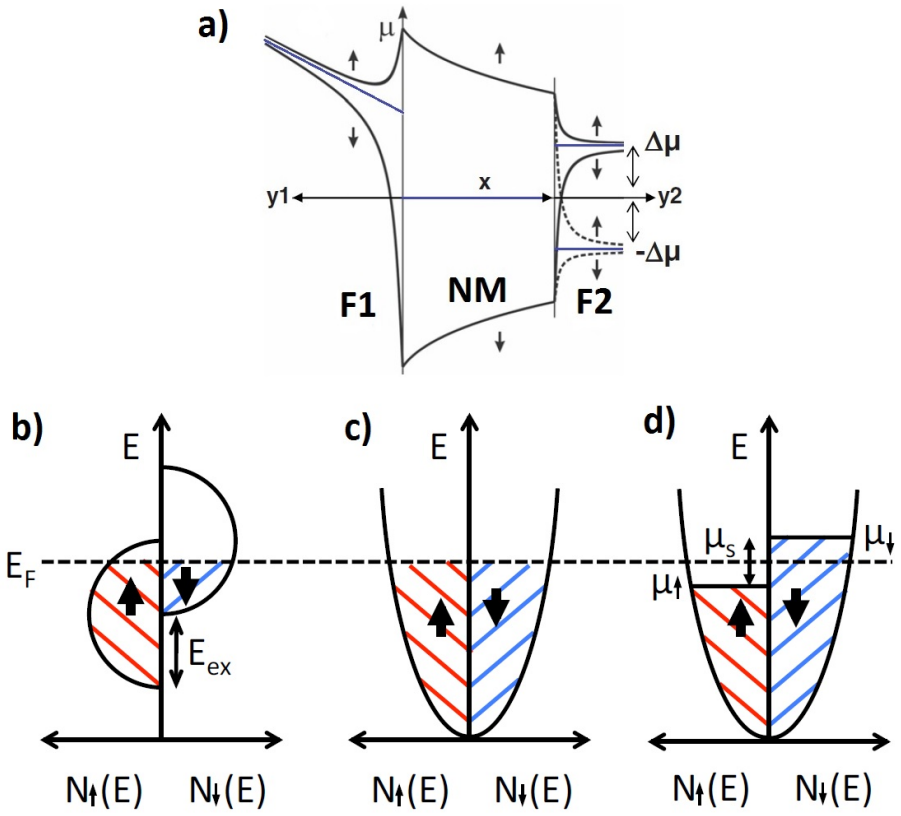

Figure 2.2: *a) Position dependence of the electrochemical potential from the injector, through the NM and to the detector. b) is the DOS for the spin up and spin down sub-bands of the FM, c) is the DOS for the two sub-bands without a spin accumulation and d) right after the spin accumulation. The original can be found in [1, 2].The diffusion away from the FMs is longer since it's a combination and the spin and drift current.*

Given that the NM does not have a spin dependent electrical conductivity σ, that means that the population of the spin up and spin down electrons is the same. The spin polarised current will create a spin imbalance at the vicinity of the F_1/NM interface

leading to a non-equilibrium spin population, defined as spin accumulation. Having no voltage source on the right hand side of the F_1 (see figure 2.1), it means that there is no current going there. The accumulated spins diffuse in both arms creating a spin current accumulation in both sides.

This way since equal numbers flow between the two ferromagnets F_1 and F_2 a pure spin current exist. The driving force of a pure spin current in the NM channel is the gradient in the chemical potential [32–34], μ_{ch} that equals to the density of the excess electrons, n, over the densit of states at the Fermi level, $N(E_F)$. The fact that the electrons are subjected to an electric field leads to an additional potential, the electrical potential V, on top of the chemical potential, called electrochemical potential [35] μ :

$$\mu = \mu_{ch} - eV \tag{2.2}$$

As shown in figure 2.2 a, b and c, the spin polarised current from the F_1 injector meets no spin imbalance in the NM channel. Given that the electrical conductivities for the spin up and down sub-bands are different [29], leads to the non-equilibrium spin accumulation in the NM. The spin accumulation is the difference in the μ between the spin up and spin down population.

$$\Delta\mu = \mu_{\uparrow} - \mu_{\downarrow} \tag{2.3}$$

The spin dependent current density in both FM and NM is described by:

$$j_{\uparrow,\downarrow} = \sigma_{\uparrow,\downarrow}E + eD_{\uparrow,\downarrow}\nabla\delta n_{\uparrow,\downarrow} \tag{2.4}$$

The first term of the equation describes Ohm's law for each of spin dependent conductivity channels, while the second term the contribution of the spin accumulation with a density of $\delta n_{\uparrow,\downarrow}$ and a diffusion constant $D_{\uparrow,\downarrow}$. The diffusion constant satisfies Einstein's relation:

$$D_{\uparrow,\downarrow} = \sigma_{\uparrow,\downarrow}/e^2 N_{\uparrow,\downarrow} \tag{2.5}$$

With $N_{\uparrow,\downarrow}$ the density of states at the Fermi level. For the spin transport part, the spin up and spin down current density is related to the electrochemical potential as:

$$j_{\uparrow,\downarrow} = \frac{\sigma_{\uparrow,\downarrow}}{e}\nabla\mu_{\uparrow,\downarrow} \tag{2.6}$$

Using the spin up and spin down current densities, one can express the total charge and spin current density as:

$$j_c = j_\uparrow + j_\downarrow \tag{2.7}$$

$$j_s = j_\uparrow - j_\downarrow \tag{2.8}$$

Using equation 2.7, the spin current can be expressed as the combination of two charge currents, one for each spin direction, that are flowing in opposite directions.

2.2.2 Transport of spin currents

For spintronic devices and applications, it is essential for the spin transport channel to preserve the injected spin polarisation for long distances. The physical property related to that is the spin relaxation time τ_s, which is the time needed for the spin to lose its spin memory from scattering effects. A different way to express the τ_s is through the spin diffusion length in the transport channel λ_{NM}, which provides information about the actual length the spin current can cover before getting depolarised [36].

These two properties are connected through the diffusion constant D_s, which is strongly related to the material itself and its conductivity as will be shown in chapter 4. These three are connected through the following equation [37]:

$$\lambda_{NM} = \sqrt{\tau_s D_s} \tag{2.9}$$

Given that both D_s and τ_s are correlated to scattering directly or indirectly, it is important that the main mechanism responsible for depolarising the spins to be analysed.

Spin scattering

The spin scattering mechanisms that will be mentioned are related to the current work. An immediate way to see the contribution of these mechanisms in an actual transport measurement is by performing a resistance as a function of temperature measurement for the metallic transport channel. The electron scattering could be either elastic, where no energy is lost during the interaction, or inelastic.

As the electrons are moving through a perfectly structured, bulk metal, they can be scattered either by electric fields, created by charged impurities for example, or phonons, or by magnetic fields, created for example from magnetic impurities.

The impurities in the metal could be either unintentional, hosted in the source material, or even intentional, for example in alloys. There are two types of impurities that could be presented in the metal and are either magnetic or non-magnetic. The presence of both can be seen in comparison to a pure metal, as an increase in the resistance as a function of temperature, but the scattering from magnetic impurities gets more pronounced at low temperatures, where the electron-phonon interaction starts to freeze out.

The effect is called the Kondo effect and was firstly explained by J. Kondo in 1964 [38]. In the resistance as a function of temperature the resistance presents a minimum at a temperature called Kondo minimum. Below that temperature, the resistance increases proportionally to T^2. Depending on the combination of the materials, at a specific temperature the electrons screen the moment and the resistance becomes constant. The temperature where this starts to happen is called Kondo temperature. The temperature dependence of a normal metal with magnetic impurities is shown in figure 2.3.

The imperfections of the crystal on the other hand, is a simpler case. They could be grain boundaries, dislocations or stacking faults, which are temperature independent. As the dimensions of the films are getting smaller or when they are structured in nanowires the scattering from the walls becomes significant as the temperature decreases. This happens because the mean free path of the electrons, the mean distance they can cover between two scattering events, increases with the decrease of temperature. Once the dimensions of the films or nanowires are in the same magnitude with the mean free path of the electrons, the possibility of them getting scattered on the side walls increases dramatically. The resistance as a function of temperature can be described by the Bloch-Grüneisein equation, $\rho = \rho_0 + \mathrm{K}\left(\frac{T}{\Theta_\mathrm{D}}\right)^5 \int_0^{\frac{\Theta_\mathrm{D}}{T}} \frac{x^5\, dx}{(e^x-1)(1-e^{-x})}$ where ρ_0 is the residual resistivity due to non-magnetic impurities and defects, K is a material specific constant and Θ_D is the Debye temperature.

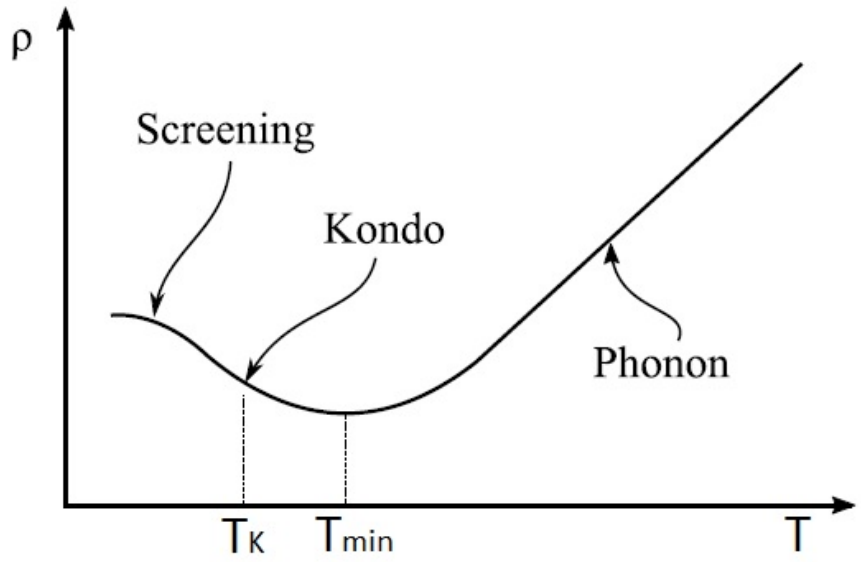

Figure 2.3: *Resistivity as a function of temperature for a metal with magnetic impurities. It can be seen that as the temperature is decreasing, and after T_{min}, the scattering from the magnetic impurities leads to a characteristic increase in ρ. Below the Kondo temperature T_K, the magnetic impurities are getting screened from the electrons and the change in ρ becomes independent to T.*

Spin diffusion

As said in the last paragraph, the spin diffusion length decays through relaxation processes either from impurities, magnetic or non-magnetic, or by scattering by phonons which in the presence of spin-orbit coupling causes a mixing in the spin-up and spin-down states.

The diffusive spin current, which is proportional to the initial spin accumulation in the injector/NM junction can be described by the 1D diffusion equation

$$\nabla^2(\mu_\uparrow - \mu_\downarrow) = \frac{\mu_\uparrow - \mu_\downarrow}{\lambda_{NM}^2} \tag{2.10}$$

The general solution of this equation for the spin up and spin down channels, can be obtained by applying the law of conservation and continuity for the electrochemical potential:

$$\mu_{\uparrow,\downarrow} = a + bx \pm \frac{c}{\sigma_{\uparrow,\downarrow}} exp \frac{-x}{\lambda_{NM}} \pm \frac{d}{\sigma_{\uparrow,\downarrow}} exp \frac{x}{\lambda_{NM}} \tag{2.11}$$

where the coefficients a,b,c and d can be calculated using boundary conditions at the junctions. What is left from the initial spin accumulation in the detector junction, can be calculated by the second part of the equation [35].

2.2.3 Detection of spin currents

Depending on the relative orientation of the ferromagnetic injector and detector, parallel or antiparallel, there will be a different voltage to be detected [39]. This can be seen easier in figure 2.4.

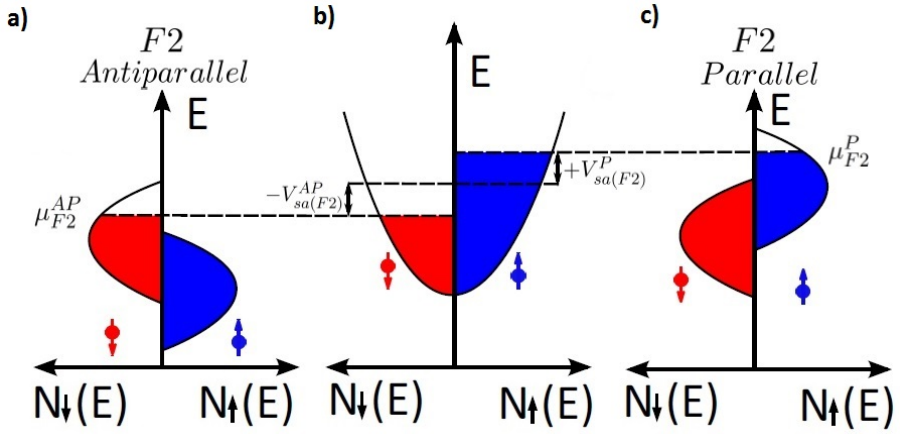

Figure 2.4: *In a) and c) are the spin up and down sub-bands of the detector when it is in the antiparallel and parallel state to the injector respectively. In b) there are the spin sub-bands of the NM channel, where depending on the configuration, it can be accessed against the sub-band. The original can be found in [3, 4].*

According to the equation 2.11, the induced spin accumulation voltage can be calculated as:

$$\Delta V_s = \frac{\Delta\mu}{e} = V_+ exp \frac{-|x|}{\lambda_{NM}} \pm V_- exp \frac{|x|}{\lambda_{NM}} \tag{2.12}$$

where the V± coefficients can be calculated using spin and charge boundary conditions. Depending on the relative magnetisation orientation of the ferromagnets, the Fermi level aligns either in spin-up sub-band (parallel) or in the spin-down sub-band,

resulting to a $V_s{}^{P}$ or a $V_s{}^{AP}$. The total voltage that reflects the initial spin accumulation is thus defined as:

$$\Delta V_s = V_s{}^{P} - V_s{}^{AP} \tag{2.13}$$

The detected voltage depends on the charge current used in the injector to create the initial spin polarised current. In order to compare the non-local voltages for the different currents, in the actual experiment what is measured in the detector is a normalised to the current amplitude voltage, $R_s{}^{PorAP}$ as shown in figure 2.5.

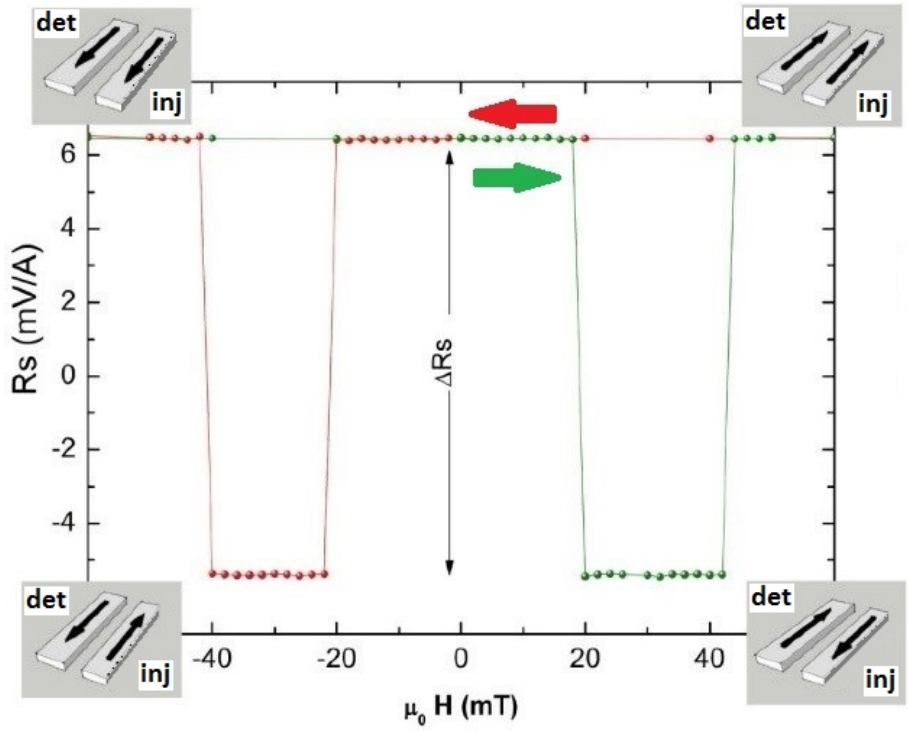

Figure 2.5: *Non-local resistance as a function of external applied field at 5 K. The difference between the non-local resistances for the different states is the spin signal* $\Delta Rs = Rs^{P}$ - Rs^{AP}.

From equation 2.13, the difference of the non-local resistances for the parallel and antiparallel state is called spin signal ΔRs. For transparent interfaces and in the case where both FMs are made out of the same material, it can be correlated to the spin polarisation and the spin diffusion length as follows:

$$\Delta R_s = \frac{4R_{NM}a_{FM}^2}{[2+\frac{R_{NM}(1-a_{FM}^2)}{R_{FM}}]^2 e^{\frac{L}{\lambda_{NM}}} - [\frac{R_{NM}(1-a_{FM}^2)}{R_{FM}}]^2 e^{\frac{-L}{\lambda_{NM}}}} \tag{2.14}$$

In the previous equation R_{NM} and R_{FM} are defined as spin resistances of the normal metal and the ferromagnet respectively. They are defined as:

$$R_{FM} = \frac{\rho_{FM}\lambda_{FM}}{w_{FM}w_N} \tag{2.15}$$

$$R_{NM} = \frac{\rho_{NM}\lambda_{NM}}{2w_{FM}t_N} \tag{2.16}$$

where ρ_{NMorFM} is the resistivity of the NM and the FM respectively, λ_{NMorFM} is the spin diffusion length of the NM and the FM respectively, w_{FMorNM} is the width of the FM and the NM and finally t_{NM} is the thickness of the NM channel.

For the lateral spin valves, the FM and NM nanowires used for the fabricated devices are in the order of a few tens of nanometres width and thickness. That means that the current densities used could generate thermal effects that could contribute to the detected voltage.

2.3 Heat currents

The generation of the heat currents takes place in the injector area and the injector/normal metal junction. The thermal effects are treated as secondary in the lateral spin valve geometry, since the main use of this geometry was to study pure spin currents. The problem arises at lower temperatures where the bulk thermal conductivity of the usual normal metals used, such as Ag, Cu and Al, increase significantly compared to the usual SiO_2 substrate and thus heat can be propagated easier. Some basic concepts about the thermoelectricity are presented in the following paragraphs.

2.3.1 Thermal conductivity

The thermal conductivity K of a solid is defined as the efficiency that a flux of thermal energy $\dot{Q_{in}}$ can be transmitted through the solid, when presenting a thermal gradient dT across its length dx.

$$\dot{Q_{in}} = -K\frac{dT}{dx} \tag{2.17}$$

Since the energy flux depends on the temperature gradient and not only the temperature difference in the two ends of the sample, that means that it propagates in a diffusive and not a ballistic way. The propagation of the energy flux is performed through phonons, magnons and electrons. Since their velocity has a temperature dependence, the thermal conductivity has a temperature dependence as well [5, 40].

2.3.2 Seebeck effect and Thermopower

Warming up a side of a metallic element at a temperature T_2 keeping the other at a lower temperature T_1, will result to an excess energy to electrons of the hot end. These energetic electrons will diffuse to the colder of the metal to reduce their energy.

This process will result to an accumulation of negative charges in the cold end of the bar, creating thus an electric field between the two ends of the bar. The electric field will keep increasing but at the same time the electrons diffusing from the hot end, will experience repulsive force from the accumulated electrons of the cold end. Once the number of electrons flowing down to the cold end through a cross sectional area per unit time is the same with those that are repulsed because of the accumulated electrons in the cold end, the electric field will stop growing.

The velocities of the electrons flowing down and up the cross sectional area are different. That results to heat transfer without charge transfer since a dynamic equilibrium has been achieved. To measure the potential difference created, two electrodes of the same material having one side at the same temperature, T_0, are attached on either side of the bar. The electrodes should be a different material to the measured sample, otherwise no net e.m.f. will be created [5].

In any other case, the e.m.f. E_{AB} created is called Seebeck e.m.f and depends only on the temperature difference between the two ends of the bar and the detecting electrodes. Given the above, the Seebeck voltage will vary even the same materials in the case of a change in either T_1 or T_2. To generalise the outcome and be able to compare with other references, the thermoelectric power or thermopower S_{AB} was created. The thermopower is defined as the derivative of the E_{AB} to the temperature difference:

$$S_{AB} = \frac{\Delta E_{AB}}{\Delta T} \tag{2.18}$$

No charge current is needed in order to measure the aforementioned effects. The

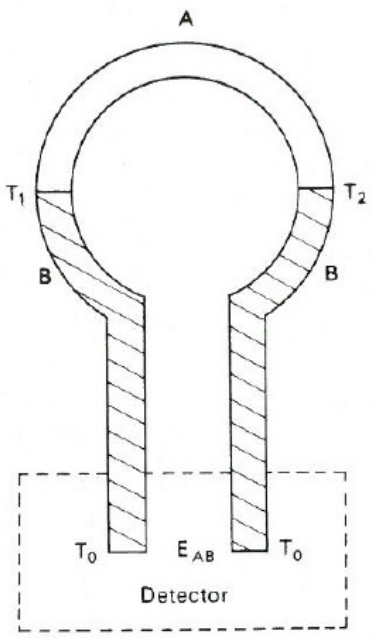

Figure 2.6: *Metallic wire A with a temperature difference in its ends from T_1 to T_2. Both ends are connected with two separate leads made out of the same metal B, having their other end at the detector at the same temperature T_0. The Seebeck e.m.f. E_{AB}, is voltage measured at the detector. The original can be found in [5].*

introduction of a charge current in the circuit will give rise to other effects such as Joule heating, in the case of a single material, or Peltier effect for junctions of materials.

2.3.3 Joule heating and the Peltier effect

Single element

Assuming an electric field in a metallic bar, that will cause an increase in the kinetic energy of the free electrons from point A with a potential V_A to point B with a potential V_B. The acceleration of the electrons will result to collisions between the electrons and the lattice transforming their,or part of their, kinetic energy to thermal energy. The increase in the thermal energy is called Joule heating [5].

The change of the potential energy ΔU in the distance of L_{AB} would be

$$\Delta U = \Delta q \Delta V \tag{2.19}$$

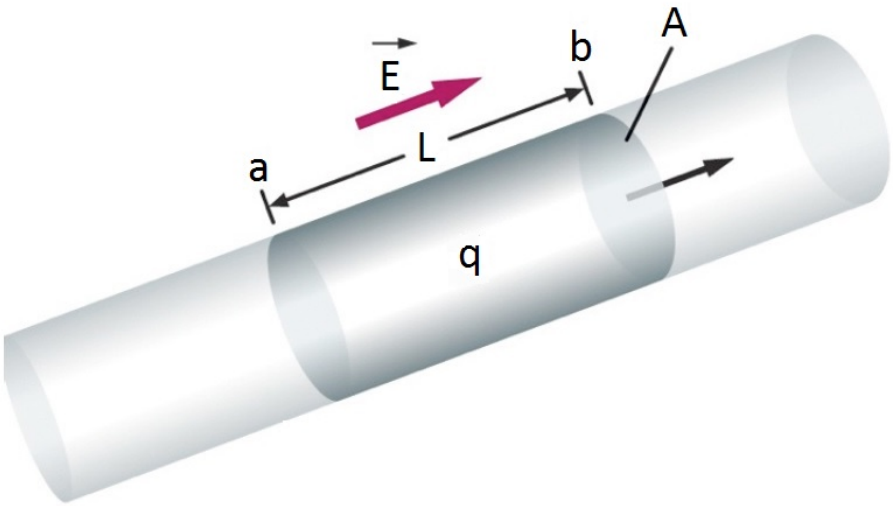

Figure 2.7: *Metallic bar of diameter A, where a charge is moving from position a to position b subject to a potential difference* ΔV.

where Δq is the charge moving from point A to point B and ΔV is V_2 - V_1. Given that V_2 is lower and V_1, that means that $\Delta V < 0$.

Power dissipation

As it has already been mentioned, from the collisions between the accelerated electrons with the lattice there is an increase in the thermal energy, called Joule heating. The power dissipated for a Δt period of time would be

$$\frac{\Delta U}{\Delta t} = \frac{\Delta q}{\Delta t} \times \Delta V \tag{2.20}$$

The amount of charge going through a cross sectional area within a period of time Δt is defined the charge current I thus the power dissipated would be

$$P = I\Delta V \tag{2.21}$$

As it has already been explained, $\Delta V < 0$ and that is why the power P is being dissipated [41].

Metallic junctions

In the case where there are two metals, A and B, connected at the same temperature T and a charge current I is flowing through both, there is another effect arising. Assuming the electric current flow derives from the existence of N_A number of conduction electrons in A and N_B conduction electrons in metal B, the current density in either side of the junction should be preserved.

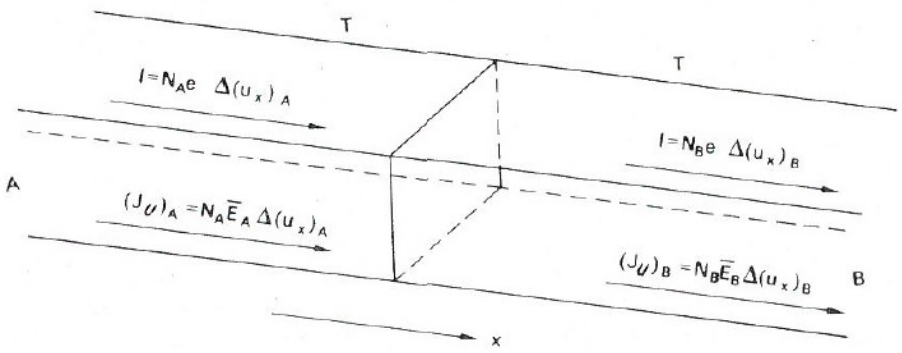

Figure 2.8: *Junction of two metals A and B, connected at the same temperature T. The current densities I are the same but the heat flux densities $(J_U)_A$ and $(J_U)_B$ can differ. The original can be found in [5].*

$$I_{D_A} = I_{D_B} \tag{2.22}$$

where the current density is $I_{DA,B}= N_{A,B}eu_{A,B}$. The electrons have drift velocities of u_A and u_B and due to this motion each electron possess a mean energy of $\overline{E}_A$ and $\overline{E}_B$. Having the current flowing from metal A to B, it brings energy to the junction with a rate of $N_A\overline{E}_Au_A$ and at the same time removes energy from B at a rate of $N_B\overline{E}_Bu_B$. The net rate of change in energy in the junction equals to the change in the total heat flux density ΔJ_u.

$$\Delta J_u = N_A\overline{E_A}u_A - N_B\overline{E_B}u_B \tag{2.23}$$

Using equation (2.7) in (2.8) it results to

$$\Delta J_u = \frac{I}{e}(\overline{E_A} - \overline{E_B}) \tag{2.24}$$

The first conclusion that can be drawn from this equation is that if metals A and B are the same, that means that $\overline{E}_A = \overline{E}_B$ and thus ΔJ_u equals 0. In the case the materials are the same, there is no change in the total heat flux in the junction.

On the other hand, if $\overline{E}_A \neq \overline{E}_B$ then depending on the if $\overline{E}_A$-$\overline{E}_B$ is >or <than 0, it results to release or absorption of heat.

The Peltier term Π between two metals A and B, is defined as the heat absorption or release per unit current.

$$\Pi_{AB} = \frac{\Delta J_{u\,AB}}{I} \tag{2.25}$$

According to equation (2.10) is linear to the current. That means that, in conjunction with Joule heating, the current direction will determine which part of the junction will be warmed up or cooled down [5].

2.3.4 Heat generation, diffusion and detection

According to the above and combined with the non-local spin valve geometry, the heat generation in the system comes from the injection area and injector/normal metal junction. The mechanisms examined in the current study will be Joule heating and the Peltier effect. The propagation of the thermal currents takes place mainly through the normal metal channel, as will be shown in chapter 5, and the detection takes advantage of the Seebeck effect in the detector junction. Furthermore, since according to the theory there is a change in the Peltier output depending on the current direction, it will be shown in chapter 5 that this results to two different signals contributing to the field independent linear term picked up during the non-local measurements.

2.4 Conclusions

The transport of pure spin currents has already been studied in the lateral spin valve geometry. The past few years though, different groups tried to explain the low temperature spin diffusion behaviour and attributed to magnetic impurities. Our approach, in chapter 4, implements the structural features of the transport channel in that. Furthermore, instead of trying to achieve a normal metal channel as clean as possible, we study the diffusive behaviour of the pure spin currents by deliberately introducing magnetic impurities at different positions of the system, in chapter 6.

The main portion of research using the lateral spin valve geometry is on spin currents with only a small number of studies in proportion studying the thermal effects. The thermal effects contributing in the non-local IVs signal, that when properly analysed can explain the behaviour and contribution of those in the behaviour of the signals that are measured. In chapter 5 there is a step forward to this by decoupling the thermal from the spin current effects and study them as a function of temperature and length.

Chapter 3

Methods

This chapter includes the procedure followed in order to move on from a blank Si/SiO_2 substrate to a fully functional device. It starts with the cleanroom fabrication that includes different lithography and deposition steps, followed by the shadow deposition for the growth of the active part of the device, x-ray diffraction for structure characterisation and finally the He gas flow cryostat for the transport measurements.

3.1 Introduction

The careful fabrication of the devices is a very important step. The reason for that is because nanowires can easily get damaged or even blow up during the transport measurements in the case of a bad fabrication. Furthermore, since there are so many geometrical parameters included in the resistance as a function of temperature measurements, there should be a recipe followed precisely so that the wire dimensions are the same within an error. Finally, a robust design is needed to assure an increase in the yield of the functional devices per chip.

The cleanroom fabrication process used, was developed and optimised by Dr J.T. Batley, Dr M.C. Rosamond and Dr G. Burnell. The author added one more step in the cleaning process between the different lithography steps, to ensure minimum, if any, residues of resist on the substrate.

There were three lithography steps for the device fabrication. The first one consisted of the preparation for the inner contacts, the second one for the outer contacts and finally the shadow deposition step. The shadow deposition system was designed and built by Dr M. Ali, Dr G. Burnell and Prof B.J. Hickey. Parts were added by Dr J.T. Batley afterwards.

3.2 Sample fabrication in the cleanroom

3.2.1 Sample preparation

The fabrication of the lateral spin valves was mainly carried out in the cleanroom. A combination of two electron beam lithography and one optical lithography step coupled with e-beam evaporation and sputtering of Cr/Au bilayers was necessary for the completion of the samples.

The SiO_2 substrates were diced using a wafer-saw and cleaned using a combina-

tion of Acetone and Isopropanol, 10 minutes in each, in a ultrasonic bath. Once the substrates were clean, they would be baked on a hot plate at 180 to ensure complete dehydration.

3.2.2 Electron beam lithography and electron beam evaporation

To improve the adhesion of the resist on the surface after the dehydration, a Hexamethyldisilazone (HMDS) primer was used. After spinning the primer on the chip, a baking would follow at 180 for 1 minute, in order to make the surface hydrophobic. The excess amount of HMDS would be removed by dipping the sample in isopropanol and then blow dry it with N_2.

Another baking step would follow at the same temperature and for one more minute. Once this was done, a Methyl-Methacrylate and a Poly (Methyl-Methacrylate) (MMA/PMMA) bilayer were used as e-beam resists. The MMA layer is actually a MMA(8.5)MAA (40/60 dilution) and the PMMA is a PMMA 950k A4. The 950k refers to the molecular weight, while the A4 to the density of molecule. Both resists were spun at 4k rpm and for 40 seconds.

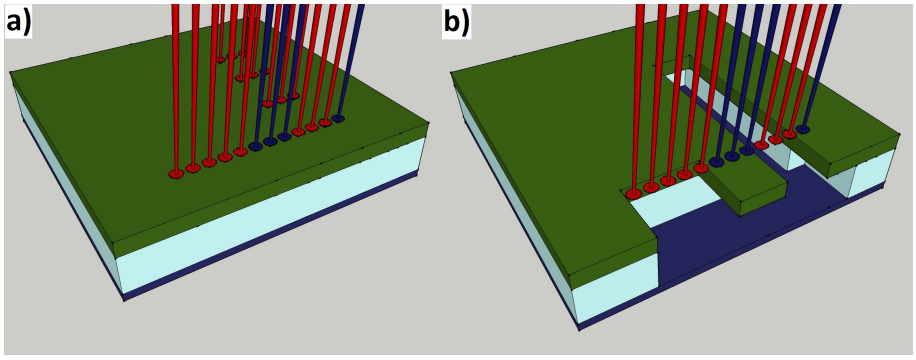

Figure 3.1: *a) MMA/PMMA resist bilayer on top of a SiO_2 substrate. b) Two e-beam doses used to form undercuts. A high one, in red, that penetrates both resists and a low one, in blue, that affects only the MMA layer.*

The reason why a bilayer of resists is needed, shown in 3.1, was because in order to use the shadow deposition feature, undercuts needed to be created. Since the MMA layer is about ten times more susceptible to the electrons than the PMMA, a natural

undercut would be created. The size of the undercut depends strongly on the supporting layer [42–44].

After the patterning in the JEOL for the inner contacts of the device, the sample was developed to clean off the resist. During the patterning, the electron beam breaks the polymer chains and by placing the chip in a solution which is a combination of IPA with water (70/30), the broken chains were washed away within 90 to 120 seconds (depending on the temperature of the solution). The chip was then rinsed in IPA for about 20 seconds and dried with N_2. Before the metallisation for the inner contacts the samples were placed in the O_2 plasma asher for 20 seconds at 50 Watt to ensure that there will be no resist residues on the substrate.

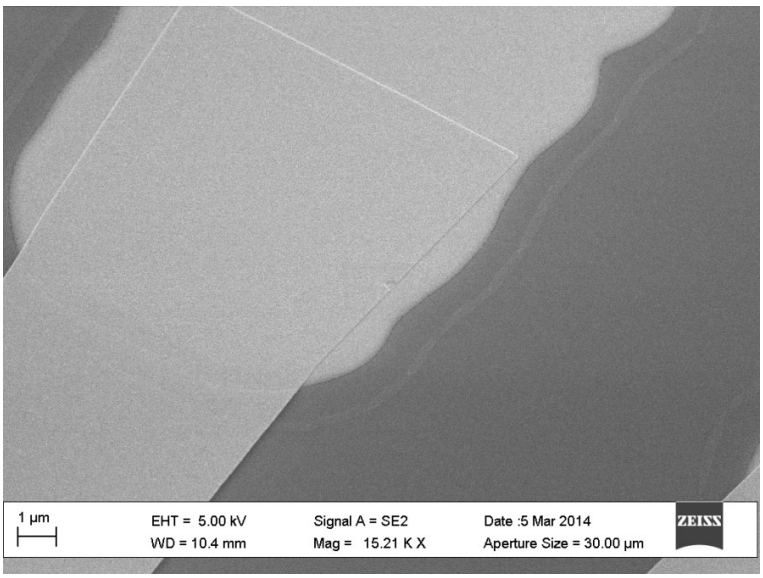

Figure 3.2: *SEM image of the alignment of the inner and outer contacts resulted from the first two metallisation steps.*

Once the broken chains were removed, the substrate with the resist bilayer would follow another cleaning step, an oxygen plasma ashing for 120 seconds. This step ensures maximum removal of resist leftovers on the substrate.

The samples are transferred in a high vacuum (HV) electron beam evaporator and Cr and Ag, 5 nm and 30 nm respectively, were evaporated normal to the sample plane. To remove the excess material and reveal the structure, the samples would be dipped in acetone, known as lift-off. Acetone dissolves the resist layers and thus the excess material that was deposited on top of it. After that they are rinsed in isopropanol and

get dried with N_2.

3.2.3 Optical lithography and sputtering

The samples were placed in the O_2 plasma asher for 2 minutes at 50 Watt power to ensure complete removal of resist residues. The samples would then get dehydrated on a hotplate at 200 for 5 minutes. For the optical lithography step, a lift-off resist (LOR 3A) resist was spun at 4k rpm and for 40 seconds and baked on a hot plate for 5 minutes at 200. After being cooled for 30 seconds, an S1813 optical resist was spun at 4k rpm for 40 seconds and baked on a hot plate for 3 minutes at 110. After that the samples were cooled for 30 seconds and then moved to the mask aligner (Karl Suess) for the optical lithography. The exposure time for the resist bilayer was 3.5 seconds using a power of 26.2 $\pm$ 0.1 mJ/cm^2.

After the exposure, the samples were developed in MF319 for about 120 seconds (depending on the temperature of the solution), and then rinsed in water and dried with N_2. Same as in the previous step, the samples were placed in the O_2 plasma asher for 20 seconds at 50 Watt. The samples were then loaded in a sputtering machine and an argon pre-deposition etch in the system would take place at 50 Watt, with 10 sccm for 1 minute, followed by the deposition of a Cr/Au (5 nm / 50 nm) bilayer and lifted off in pre-warmed NMP at 75. To ensure complete removal of resist that might have reside after the lift-off, the samples are placed in the O_2 plasma asher for 2 minutes at 50 Watt power.

3.2.4 Shadow deposition

Before the shadow deposition and in order to pattern the active part of the device, there was another electron beam lithography step, but with the difference that the MMA resist would be MMA(8.5)MAA EL11 which when spun at 4k rpm for 40 seconds would result in a 500 nm thick layer. The devices were patterned in the JEOL using 500 pA, EOS3, 440 μC/cm^2 base dose and developed in IPA with water (70/30) for about 150 to 240 seconds and a temperature of 20 to 21 [45].

Once the sample were ready to go into the UHV system, they would be accompanied with a 8 mm by 8 mm plain substrate to be used for x-ray characterisation. The base pressure before the deposition was about 2 to 3 $\times$ 10^{-9} mbar. A combination of mechanical pumps, a diffusion pump and cryotraps was used in order to achieve

pressures of this magnitude. The system was also equipped with a load lock, a necessary feature to avoid breaking the vacuum in the main chamber every time that a sample has to be loaded or unloaded.

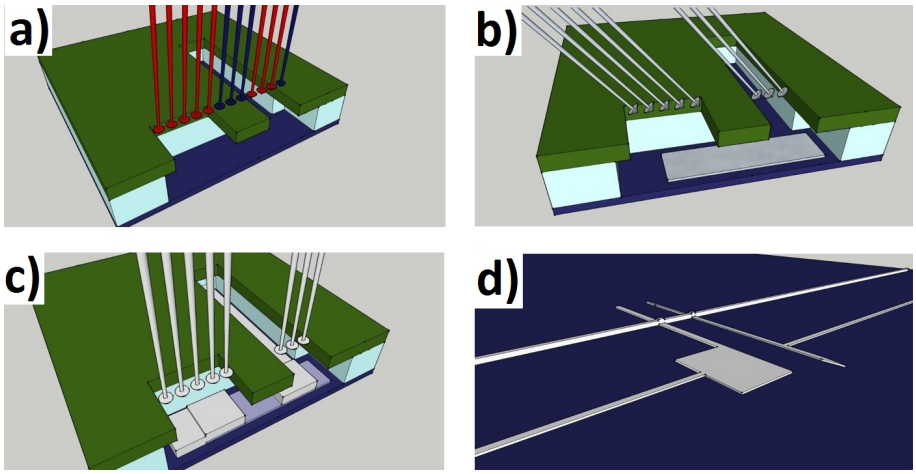

Figure 3.3: *Angular deposition and lift off. In dark blue is the SiO_2 substrate, in light blue the 5000 Å MMA layer and green the 2000 Å PMMA layer. In b), 300 Å of Permalloy were evaporated from the e-gun at an angle of 45° with respect to the substrate. After that, in c), 1000 Å of silver were thermally evaporated from the K-cell, normal to the substrate. Finally, in d), after finishing the evaporation process, the excess material was lifted off in Acetone to reveal the actual device.*

The main feature that allowed the shadow evaporation was the 3-axis sample rotation stage. This sample holder would allow multiple angle deposition whilst retaining very clean interfaces between the different materials.

The system, see figure 3.4, can host up to 4 different materials for electron beam evaporation in a Copper hearth. On top of that, there are two Knudsen cells for thermal evaporation. For the e-beam evaporation, a Tungsten (W) filament of 7 and 1/2 turns was used. Large currents, about 10 A, were driven through the filament in order to thermionically produce the electron beam. To avoid melting the element, W was chosen since it has a melting point of 3422, the highest amongst the metallic elements. The beam was then accelerated at a potential of 7 kV, and then properly aligned on the target.

For the thermal evaporation through the K-cells, a current would be supplied in a Tungsten filament that was wrapped around a Boron Nitride crucible. The reason why a Boron Nitride crucible was selected was because as a ceramic material it can withstand

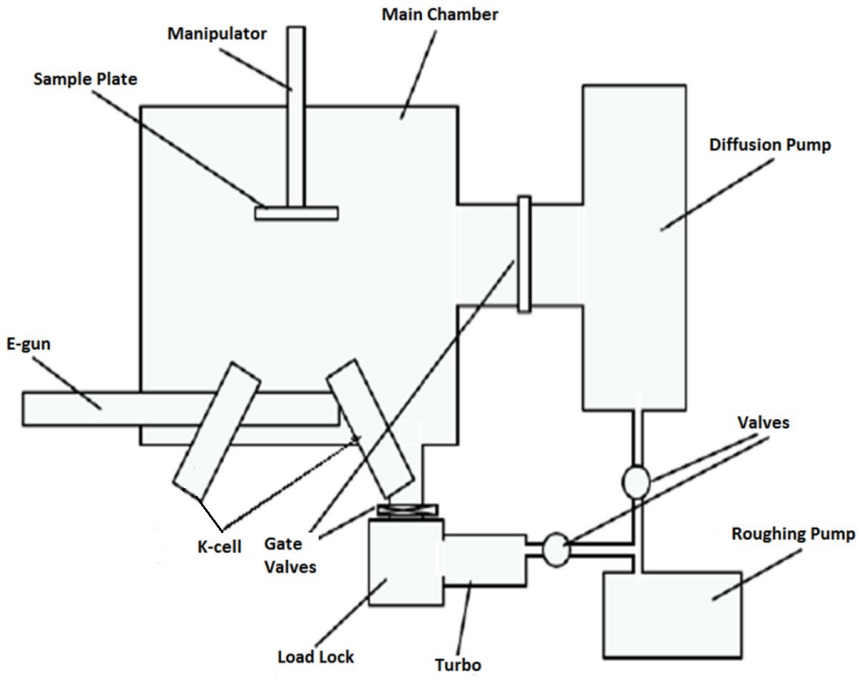

Figure 3.4: *Diagram of the evaporator used for growing all the samples used in this study. The original one can be found in [6]*

high temperatures having a melting point of about 3000 and can be thermally cycled a few times before it has to be replaced. The basic principle of the evaporation is simple. Current is flowing in the W filament, warms the crucible up to the melting point of the metal it's hosting and then the vapours of the material are thermally evaporated to the substrate.

The FM electrodes used for the devices were e-beam evaporated Permalloy (Py). For the normal metal (NM) electrodes Vanadium (V) was used and finally the transport channel was always thermally evaporated Silver (Ag). For the patterned devices, the FMs were evaporated using a power of about 700 Watts. The sample was tilted to 45^o to achieve the shadow evaporation and 300 Å of Permalloy were evaporated. After completing the e-beam evaporation, the sample was tilted in such a way that was normal to the K-cell in order to thermally evaporate Ag. The thickness used in this case was 1000 Å. The steps from the fabrication of the active part of the device to the lift off are summarised in figure 3.3.

Although using the shadow deposition technique one can produce samples with very

clean interfaces by depositing metals at different angles without breaking vacuum in the system, it is vary complicated with a relatively low success rate. About 60 % of the devices produced with this technique where used to obtain the results presented in this study.

3.2.5 Scanning Electron Microscopy

After the growth of the nanofabricated devices and the lift-off in acetone, the devices would be observed in the Scanning Electron Microscope (SEM) to check the yield of the growth. The SEM used for the imaging of the devices was equipped with a field emission gun (FEG-SEM). This is a tungsten wire with a very sharp tip that usually has a size of a few tens of nanometres. It uses field electron emission to produce an electron beam which is then accelerated and directed through a number of lenses and apertures necessary for the beam focusing, before it hits the surface of the sample.

These high energy electrons interact with the sample and produce X-rays, backscattered and secondary electrons, depending on the depth of the interaction. From the above, for the direct imaging of the sample, the secondary electrons are used, while for more surface related information the backscattered electrons are used.

An advantage of the FEG-SEM used for the study was the rotating sample stage. Imaging at an angle allows better understanding of the undercut the overlap of the nanowires as shown in figure 3.5.

In figure 3.5, is the MMA/PMMA resist bilayer before the shadow deposition and after the development. To achieve an imaging on that, a layer of Au was sputtered on the resist. The imaging revealed information about the undercuts, both the natural and the forced one, exaggerated in the pattern of 3.5. Interestingly in the overhung areas, the parts where the MMA was removed and only the PMMA layer remained, were slightly submerged compared to the areas where both resists were present. That could cause shadowing effects during the deposition.

In figures 3.6 a and 3.6 b are the devices after the deposition but before the lift-off. The exact size of the natural undercut can be seen in 3.6 a, which is about 190 nm, and the size of the undercut for the shadow deposition in 3.6 b, about 470 nm. Apart from that, the thickness of the MMA layer measured to be 450 nm and that of the PMMA layer 270 nm.

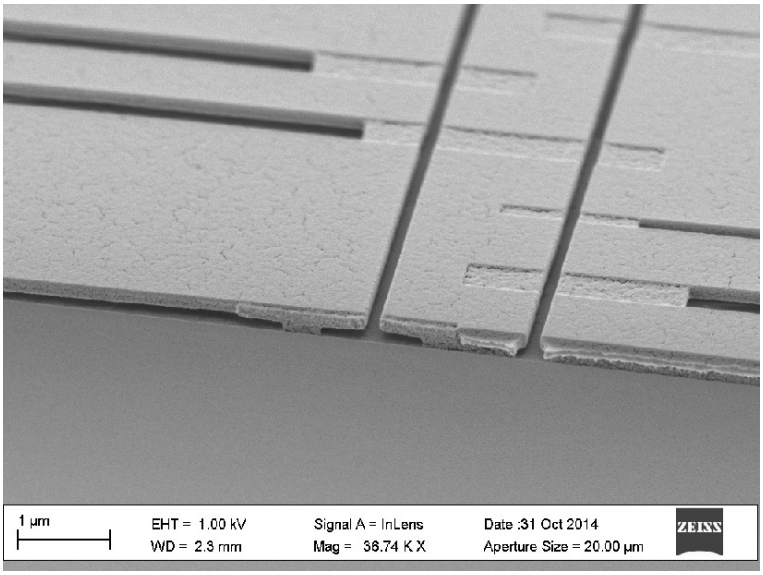

Figure 3.5: *SEM imaging of the MMA/PMMA bilayer at an angle of 60º and before the shadow deposition. The submerged PMMA parts are those where only a low electron dose was used and thus only the MMA layer was affected and developed.*

3.3 Transport measurements

3.3.1 Device characteristics

As found by Lecocq et al. [43], the connecting wires can't be patterned to have any possible width (W). If the width is too big, both materials will be evaporated on the substrate and create a short-circuit on the junction area. The W should satisfy the equation [43, 46]:

$$W < tan(\theta)e_t - \delta_{min} \tag{3.1}$$

Where θ is the angle of deposition, e_t is the thickness of the support layer (PMMA in this case) and δ_{min} the residual undercut depth that's created in the MMA layer by the high radiation dose.

On the geometrical features of the devices there are rules as well. As it has already been mentioned in chapter 2, to measure the ΔRs, the injector and the detector should be able to switch independently. One way to achieve that, is by growing the two FMs to have different thickness. A more interesting way of doing that is to pattern a pad on the end of one of the electrodes [7, 8]. In Shigeto et al. [7], Py/Cu/Co trilayers were

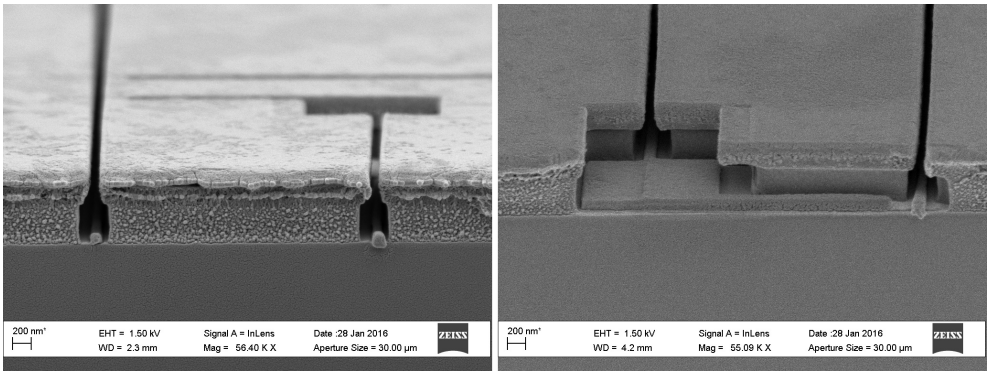

Figure 3.6: *SEM of the undercut of the devices. On the left is a demonstration of the natural undercut, with a size of about 190 nm. On the right is included an undercut used for the shadow deposition with a size of about 470 nm.*

grown in two patterned wires where one of them had a pad at one end, as shown in 3.7.

It was found that a domain wall nucleates in the pad at smaller fields and gets pinned to the mouth of the pad-connection point between the pad and the wire-until the field reaches the switching field of the wire and so it penetrates it, reversing the magnetisation in the wire.

The above was supported by micromagnetic simulations by Kimura et al. [8] a few years later 3.8, using object-oriented micromagnetic framenetwork (OOMMF) software. To make sure that the domain wall will only propagate in the pad, the other end of the wires was patterned to have pointy edges. This is because the domain wall would always nucleate and propagate at the flat edges, as theoretically and experimentally observed by Thomas Schrefl et al [47].

3.3.2 He^4 cryostat

Electron transport measurements were performed in a variable temperature helium cryostat equipped with a superconducting solenoid that can produce magnetic fields of up to 8 T. A variable temperature insert (VTI) immersed in a liquid helium reservoir is used to allow a continuous adjustment of sample temperature over a wide range. The helium reservoir is isolated from the ambient room temperature and surrounded by a liquid nitrogen jacket. To reduce the evaporation loss due to temperature difference, the cryostat is double shielded by a high vacuum space between the walls and liquid nitrogen jacket.

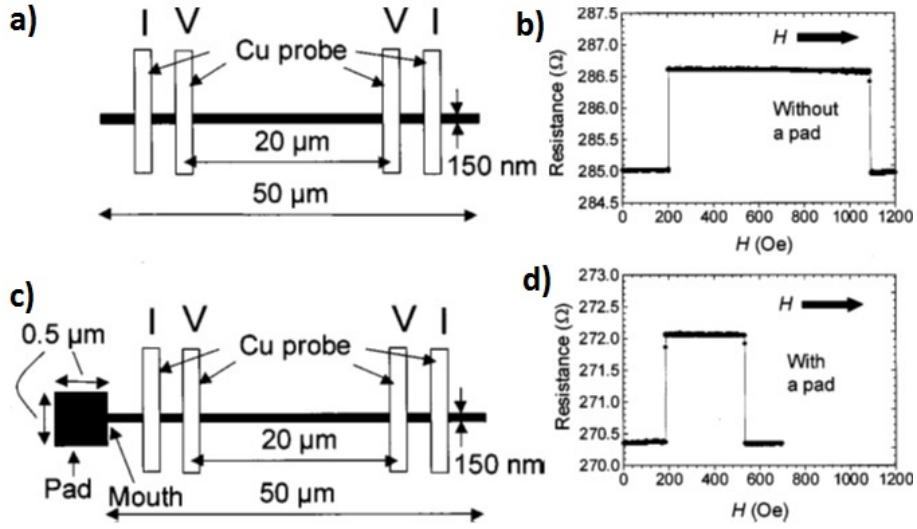

Figure 3.7: *Illustration of the two sets of patterned wires without a pad (a) and with a pad (c) to help in the magnetization reversal. In b) and d)are the corresponding resistances as a function of the external magnetic field H parallel to the wire axis taken from [7].*

The sample temperature can be controlled over the range from 1.5 K to 300 K by balancing the helium flow via an adjustable needle valve as well as the heater and the pumping speed. Temperatures below 4.2 K were obtained by reducing the vapour pressure of liquid helium in the sample space using a pump. The measured sample is mounted on a holder attached to the end of a wired stick sitting at the lower end of the cryostat. There are 20 measurement lines that are fed through the stick to the sample enabling different measurement configurations.

3.3.3 Stick and sample-holder

For the electron and spin transport measurements, a stick and sample-holder were designed and built. The stick is made out of two co-axial tubes made of type 316 stainless steel to ensure it will not get magnetised and interfere with the transport measurements. On the top of the stick is placed the breakout box that carries 20 signal lines plus 8 more contacts on its back. The triax for the current supply that splits to I_{high} and I_{low}, and a four-way lemo for the voltage output that splits to two V_{high} and V_{low} for the two available channels of measurements. There are three reasons why the break out box is on the top of the stick.

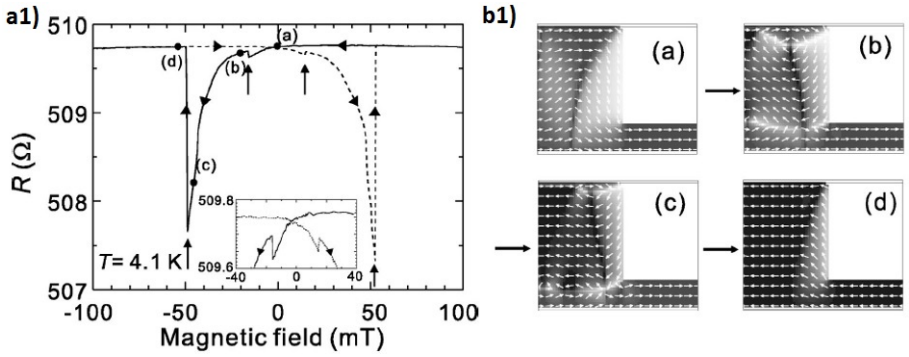

Figure 3.8: *After having the wire and pad saturated, the magnetisation reversal was firstly observed in the pad and then in the wire. The simulation of the steps is on b1), taken from [8].*

- Direct access to the signal lines
- Direct way to minimise the number of connections until the signal is picked up
- Minimise the length of the BNC cables needed in order to connect the voltmeter and source to the signal lines

From each of the 20 connections available on the breakout box, there is a copper line going down the stick, part of a copper loom. The copper loom has 12 twisted pairs, a total of 24 lines. Each pair of lines is used to measure the voltage of the supply current. The lines are twisted non-inductively to minimise pickup noise from the lab [48]. To reduce interference between the signal lines, those carrying current are separated from those used to measure voltage using the 2 extra pairs of lines. The copper loom is fixed on the outer surface of the inner tube using GE varnish, appropriate for measurements at cryogenic temperatures and the outer tube shields the signal lines from external noise.

The thermometer lines are separated from the signal lines as they are not driven from the breakout box. The thermometer was a Cernox and was calibrated by the author, against an already calibrated thermometer. Two lines were used to drive copper cables down the stick to be used as a part of the sample heater. To isolate the temperature and heater lines from the signal lines, they were driven inside the inner tube.

To create a radiation shield, baffles were soldered on the outer surface of the inner tube of the stick. They are half-moon shaped to allow free gas movement and also

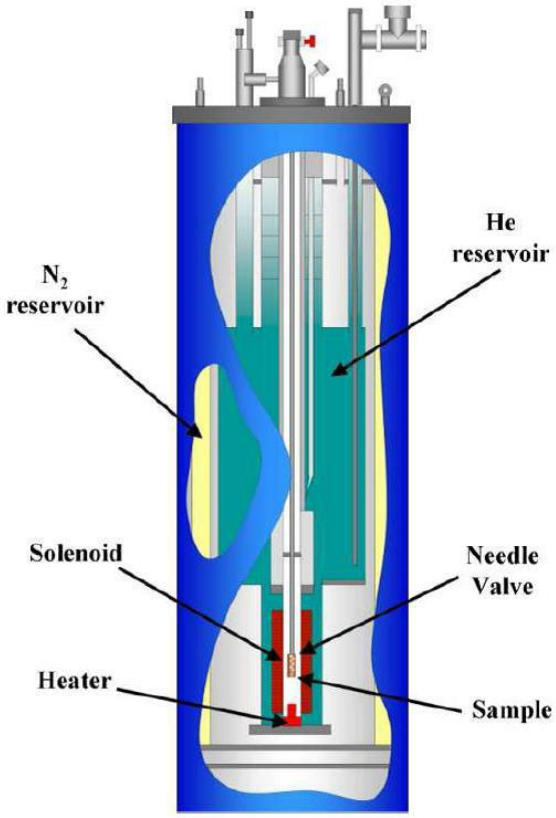

Figure 3.9: *Schematic of the He flow cryostat used for the transport measurements. It can apply a maximum field of 8 T at temperatures between 300 K to 1.5 K [6].*

avoid building pressure between the tubes as the Variable Temperature Insert (VTI) is being pumped. Since there are connections of different metals, emfs can rise. To minimise that, an $In_{97}Ag_3$ eutectic solder was used, as it has thermoelectric properties that are closer to copper's compared to the normal lead/tin ($Sn_{60}Pb_{40}$) solder [48].

The sample-holder was made out of a single piece of oxygen free copper. Copper was chosen because it is non magnetic and also has one of the best thermal conductivities amongst the metals [40]. That means that the whole sample-holder should act as a very efficient thermal bath for the sample, should ensure temperature homogeneity, it should quickly and closely follow the VTI temperature and because of the mass it possesses, the temperature of the sample-holder should be easily stabilised.

To remove problems with static discharges on the sample, a printed circuit board (PCB) with 16 signal lines, was designed and built, each of which carries a low pass

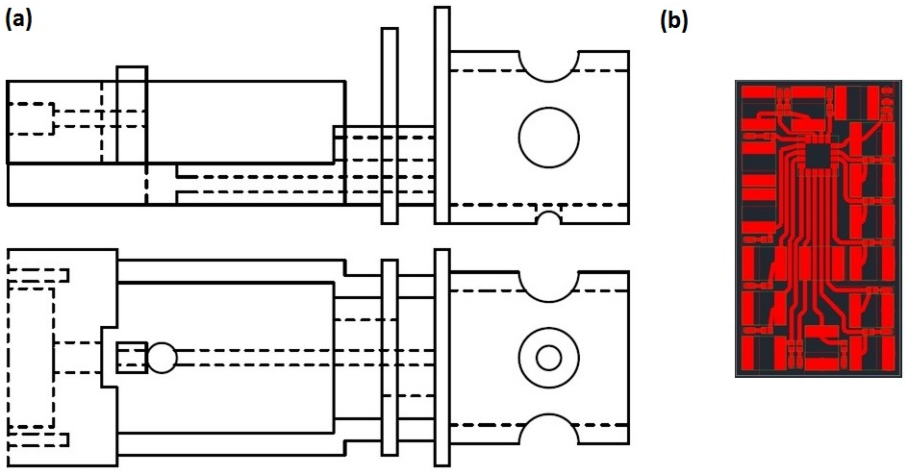

Figure 3.10: *AutoCAD design of the sampleholder and the PCB used for all the measurements in this study.*

RC filter. The values selected for the circuit were R = 110 Ohms, C = 0.47 μF. The cut off frequency can be calculated as

$$f_c = \frac{1}{2\pi RC} \tag{3.2}$$

That results to an f_c of (3000 ± 100) Hz. The capacitors impedance at the cut off frequency is

$$X_c = \frac{1}{2\pi f_c C} \tag{3.3}$$

It is calculated to be (110 ± 7) Ω. So the total impedance of the filter can be calculated as

$$Z = \sqrt{R^2 + {X_c}^2} \tag{3.4}$$

The resulting impedance is (200 ± 7) Ω. Given these values the Johnson-Nyquist noise is calculated by equation (4) and turns out to be (6.0 ± 0.3) nV.

The outer part of the PCB has two lines that work as a common ground for the filters (separated into two groups). The grounds are basically two 50 Ohm resistors, terminators, on the breakout box. The group of thermometry and signal lines were separately heat sunk around the head's top end and soldered in different lines of a printed circuit board (PCB) that lead to a specific part of the sample. The material

used for the heater was a NiCr wire, wrapped non inductively around the sample pillar [48, 49]. To enable easy access for the soldering and also protect the line from being scratched inside the cryostat, holes have been drilled and grooves have been made at the side of the holder, shown in 3.10.

3.4 X-ray reflectivity

X-ray reflectivity and x-ray diffraction are techniques used for characterisation of thin films and depend on the coherent interference of scattered x-rays where information about the thickness, roughness and crystal structure for a film can be obtained. X-rays are short wavelength, high-energy electromagnetic radiation and are produced when high-speed electrons collide with a metal target inside a vacuum tube. This tube contains a tungsten cathode filament, which is heated by an AC voltage and electrons are emitted thermionically. Electrons are accelerated under high potentials, normally a few tens of kVs, toward the target, creating the x-rays during the electron deceleration. The x-ray are collimated through slits and filters before reaching the sample, in order to obtain specific characteristic wavelengths.

When an x-ray beam is accelerated onto a crystalline material, it scattered from the parallel planes of atoms in the crystal. If the scattered waves from these planes interfere constructively, diffraction takes place. The diffraction from successive planes separated by the interplanar distance d obeys Bragg's law:

$$2dsin\theta = n\lambda \tag{3.5}$$

Where n represents an integral number of wavelengths and θ is the angle of incidence. Throughout this work, x-rays are generated from a copper target with a characteristic wavelength of 1.54 Å.

The x-ray reflectivity measurements were carried out by varying the angle of incidence ω (ω=θ) and detecting the reflected x-rays by a movable detector at an angle 2θ. This mode of operation is used to satisfy the specular condition where the incident beam angle and the detector angle are equal, therefore the coherent scattering of x-rays can be probed. The corresponding intensities of the reflected waves were measured as a function of the angle (2θ).

The thickness of a thin film can be determined from the angular positions of the

constructive peaks on the diffraction curve. These peaks arise from interference between x-rays reflected at either the air/film interface or the film/substrate interface. The former emerges at incident angles θ below a critical angle θ_c where total external reflection takes place. Exceeding the critical angle causes the x-rays to enter the film and reflect from the film/substrate interface. Multiple reflections can occur within the film and give rise to interference fringes. The period of the interference fringes in the reflected intensity are known as Kiessig fringes which are related to the thickness and the roughness of the film. The thickness t therefore can be deduced by analyzing the angular distribution of the resulting interference pattern using the Kiessig equation [50]:

$$n\lambda = 2t\sqrt{sin^2\theta_n - sin^2\theta_c} \tag{3.6}$$

3.5 Scanning thermal microscopy

Different thermal responses were detected while measuring the spin signal of the lateral spin valves, as an offset voltage, for the Peltier effect, and the quadratic part in the non-local IVs due to Joule heating. In order to cross-check the two different contributions and their magnitude, the scanning thermal microscope technique (SThM) was employed. The measurements were performed at IBM, Zürich by Dr F.R. Menges.

SThM's working principle is based on the scanning of a thermal sensor with a sharp thermally conductive tip that is also used as a heater, across a sample surface. The tip is mounted on a force sensitive cantilever and the feedback loop is used in order to maintain a constant tip-surface force while scanning across the sample surface in a raster way. With the tip in contact with the sample, that has a different temperature, the heat transfer between the tip and the surface changes the sensor temperature.

To map the temperature distribution of the nanowires, two different steps required. At first a heat flux related signal is measured of the scanning probe in contact with the sample surface for a known temperature difference. The second measurement is at an unknown temperature difference and the change in the heat flux signal gets related to the changes in the sample temperature.

At first the cantilever temperature needs to be calibrated. The calibration relies on measuring the current-voltage response of the cantilever and relating it to the power that is dissipated to the temperature of the heater using the assumption that all the

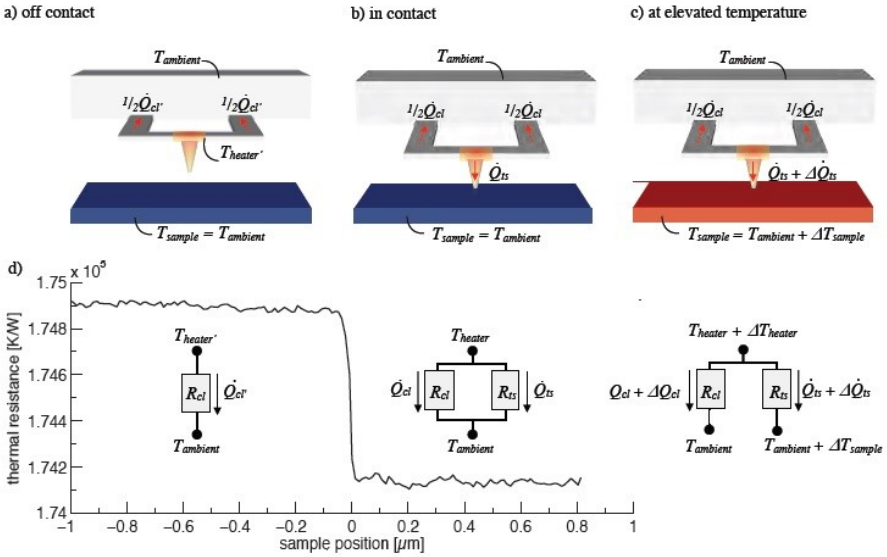

Figure 3.11: *Tip-sample arrangement for the temperature evaluation. a) Tip not in contact with the sample, the temperature of which is the same with the environment. b) Tip in contact with the sample at the temperature of the environment. c) Tip in contact with the sample at a temperature of the environment plus a small ΔT. d) Thermal resistance of the cantilever as a function of the relative position of the tip and the sample. When the tip is in contact with the sample surface, the measured thermal resistance drops [9].*

electrical power that is dissipated, leads to the increase of the heater temperature. Thus, the resistance measured can be correlated to the temperature of the heater.

The second step is to calibrate the changes in the heat flux by approaching the tip to the surface as shown in figure 3.11. If the sample temperature change by a small amount, the heat flux will change in relation to the sample and heater temperature. Given that the heater temperature difference can be calculated, as it is related to its thermal resistance, that can be measured, it means that the only unknown is the elevated sample temperature.

Chapter 4

Spin diffusion properties of a Py/Ag/Py lateral spin valve

In this chapter, we analyse the spin diffusion properties in the Py/Ag/Py lateral spin valve system. We use a 4 point method to obtain our characteristic non-local IVs, where we separate the contribution of the spin (linear, field dependent term) from the thermal component (linear and quadratic field independent terms). Using the spin related part of the linear term, we study the diffusive behaviour of spins as a function of ferromagnetic separation and temperature, from 270 K down to 2 K. We find that by increasing the deposition rate of the normal metal channel, we increase the spin signal and diffusion length in Ag. The lab-view software "The one code", that was used to record all the transport data presented in the experimental chapters of this thesis, was developed by Dr. Gavin Burnell.

4.1 Introduction

The spin signal and spin diffusion length of normal metals were found to present interesting features that deviate from the expected behaviour when measured using lateral spin valves.

In 2008, Kimura et al. [51] presented for the first time the temperature dependence of the spin signal and spin diffusion length measured in a Py/Cu LSV deposited using multi-angle deposition (single step), followed by Casanova et al. in 2009 [1]. They used Cu as their normal metal and as expected the spin signal in the high temperature regime was dictated by the electron-phonon interaction. At low temperatures where the electron-phonon interaction in suppressed, they expected that the spin signal would saturate, but instead they got a characteristic downturn [1, 34, 42, 52–56] at about 30 K. They explained their data saying that the external sides of the Cu nanowires were oxidised. As the temperature is decreasing the mean free path of the electrons is increasing and thus the scattering there is more pronounced.

In 2012, Idzuchi et al. [57] studied the spin-flip mechanisms in Ag using two sets of Py/Ag LSVs, with and without an MgO capping layer (on top of the structure), to find that the surface spin scattering was suppressed with the capping and the spin-flip probability would follow the Elliot-Yafet mechanism. Although it was not discussed if there were an upturn in the resistivity at low temperatures, the devices without the capping layer exhibited a downturn in the spin diffusion length, which was absent in the ones with the MgO. It is worth mentioning that the FM and NM channels were deposited in separate, though connected vacuum chambers.

In the same year, Zou and Ju [52] studied the origin of the spin-flip rate independently in Py/Cu LSVs. They suggested the existence of magnetic impurities in the NM channel, specifically at the edges, saying that because of the fact that the FM layer was deposited first, FM impurities would accumulate in the PMMA overhang and then be redeposited in the side wall of the NM during its deposition. That would lead to the conclusion that with a two-step deposition, one could avoid the incorporation of the impurities and thus the abnormal downturn in the spin signal and spin diffusion length. To further support that, they oxidised a device in ambient conditions and managed to increase the spin signal and avoid having a downturn as well.

In 2013, Villamor et al. [58], in their study concluded that the strongest component of scattering was not from the walls of the NM but from the grain boundaries (GB) in the NM channel. Furthermore, their spin valves were grown in two steps but the downturn in the SDL and the spin signal [59], was still apparent, result that contradicted the prediction of Zou et al [52].

Liam O'Brien et al. [60] after a long study of different combination of the FMs and NMs, all grown using a single step shadow deposition, concluded that the reason why the spin diffusion length in the NM deviated from the simple EY model is because of the existence of Kondo impurities. These could be hosted in the vicinity of the NM/FM interface and their effect would be pronounced or not, depending on the Kondo temperature of the FM impurity in the NM.

The Yi Ji group from Delaware published a study in the same year [61], using a single step deposition of their Py/Ag LSV with the difference that a 2 nm thick AlOx layer was deposited between the Py and Ag layer. Their spin signal exhibited no downturn and was attributed to the fact that for energy reasons, the FM impurities would migrate to the grain boundaries and since the scattering from these is stronger, the impurities would be screened. The introduction of an AlOx layer though was discussed in [60], as the Kondo temperature of Fe in Al is very high and the impurities would be screened anyway.

A year later, Pan et al. [62], prepared two sets of Py/MgO/Ag LSVs, one with an MgO cap and the other without. He found out that the SDL of the devices with MgO as a capping layer was a lot longer. The reason for that was because by adding an MgO capping layer the surface spin scattering at room temperature decreased by a factor of ten leading to the increase of the diffusion length.

In the same year, Isasa from the Casanova group prepared a study that was inspired by [58] where they found out that the main scattering mechanism was not from the NM side walls, but from the crystal grain boundaries [63]. They prepared two sets of devices. A polycrystalline one using a two-step fabrication technique, and another one, where the NM was grown in film form using MBE and patterned from there. The mean grain size was 19 ± 6 nm against 41 ± 4 nm respectively. In the end they managed to improve the diffusion length in Ag by a factor of 2, by decreasing the spin relaxation from the grain boundaries, without showing data of its temperature dependence.

Finally in 2015, Batley et al. [64], proved that the temperature dependence of the diffusion length and spin signal derives from the fact that magnetic impurities pre-exist in the source material of Cu used. The result was that by increasing the purity of the source material, the Kondo scattering was reduced and the spin diffusion length and spin signal were proportionally increased.

The overall purpose of the chapter is to compare the spin transport properties in Ag using two different deposition rates, 0.2 Å/s and 0.4 Å/s. The idea behind that is that the downturn in the spin signal is created by magnetic impurities but can be affected by the structure of the transport channel. Before the spin transport analysis, x-ray reflectivity and diffraction as well as electron transport data are presented. The study includes measurements in films and nanowires.

4.2 Structural and electron transport properties of Ag, depending on the growth rate

4.2.1 X-ray reflectivity, diffraction and SEM of films

Two thick Ag films were deposited in the evaporator at a base pressure of less than 3×10^{-9} mbar in the same vacuum cycle. The substrate used in both films was SiO_2, and was cleaned using the same standard process of cleaning with acetone and isopropanol. Two different deposition rates were used for the two films of Ag that were grown under similar conditions, having the same thickness of about 1000 Å and 0.2 Å/s and 0.4 Å/s of thermally evaporated Ag through the K-cell. The samples had their thickness measured using low angle X-rays (where 2θ is less than 10 degrees) and fitted to extract the composition of their surface, related to the critical edge of the low angle spectra, their roughness. Finally at high angles, the data revealed the main direction of the

crystal growth in c axis and the mean size of the grains in this direction. The same deposition rates used for the growth of the spin transport channel of the nanofabricated devices and will be discussed later on in this chapter.

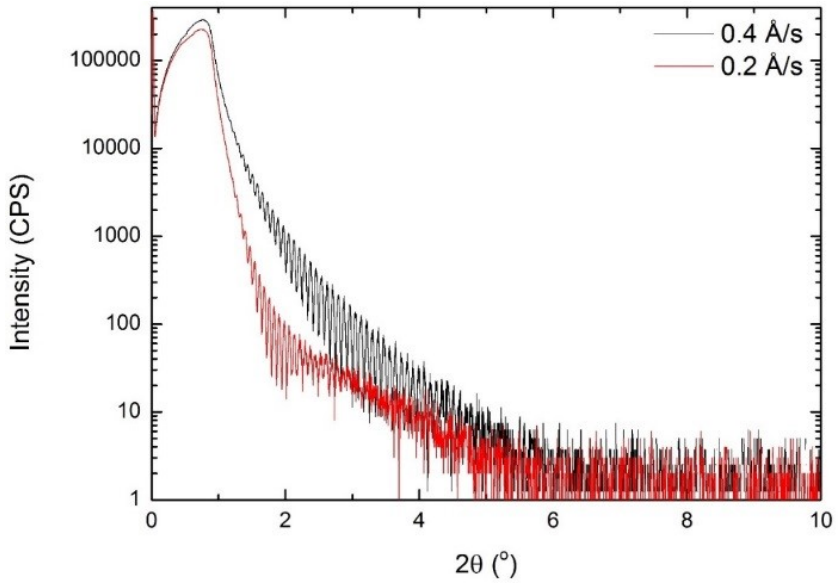

Figure 4.1: *Reflectivity data of the films where there is a striking difference of the spectra with the change in the deposition rate.*

The low angle X-ray data shape, shown in figure 4.1, revealed some interesting things directly. The critical edge is at the same angle for the two samples, as expected, meaning that the composition of the surface layer is the same. The critical edge of an XRR spectra is the angle that the beam starts to penetrate the surface of the sample and is related to the refractive index of the top layer and in extension the layer itself. Apart from that, the intensity of the sample grown using a lower rate drops faster than that that was grown using double the rate. That means that the roughness of the slowly grown sample is larger. Furthermore, the fact that the samples have exactly the same amount of material, but only one of them presents a modulation envelope, a sign of oxidation, it indirectly implies that there is a larger number of grain boundaries, since Ag oxidises through those [42, 65, 66]. Moreover, a larger number of grain boundaries means that in the transport measurements it is expected that the resistivity will be higher in this one leading to the conclusion that the RRR value, and thus the actual structure, is not as good as the one that was deposited with a higher rate.

The reason behind that is mostly because the atoms of the sample grown with a higher rate had larger kinetic energy, since to achieve a high rate means to have a higher temperature in the K-cell (1050 K to 1100 K). Once the more energetic atoms reach the substrate, they still possess enough energy to move to a preferential position before they condense. Otherwise, they condense mostly in positions where a nucleus has already been formed. That will lead to island growth (Volmer-Weber) and not a combination of island and layer by layer (Stranski-Krastanov).

To quantify the information that can be extracted from the reflectivity data, the low angle scans of the two films were fit using the X-Ray software BEDE.

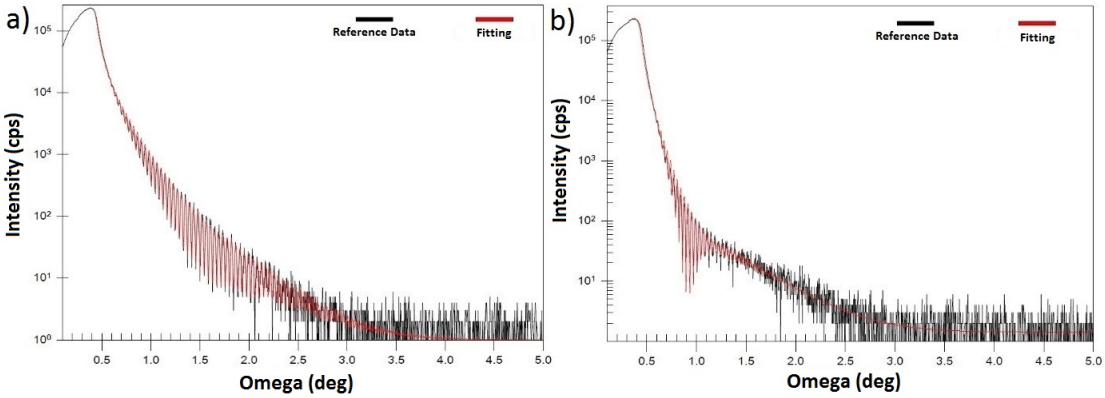

Figure 4.2: *Fittings of the two Ag films with the different deposition rates. In a) is the one grown using a rate of 0.4 Å/s, while in b) is the one with 0.2 Å/s. The line in black is the experimental measurement, while the one in red is the fitting produced using the software BEDE.*

From the low angle scan fittings, depicted in figure 4.2, the thicknesses, roughness and top layer material were extracted. The thickness of the two films was found to be about the same of 1000 ± 50 Å. The roughness though changes dramatically with the deposition rate. Both films were found to have a AgO layer on top (11 Å and 19 Å respectively) and the roughness of these was 3 Å and 14 Å respectively. The depth of the fringes for the 0.4 Å/s samples, was translated as crystal planes parallel to the top surface, leading to a smooth surface.

The high angle scans of figure 4.3 revealed structural features. Since the samples were grown on a substrate that is cooled to about 270 K, they are expected to have been grown in a polycrystalline way [67, 68]. The alignment was performed on the surface of the sample. The high angle scan revealed the (111) Ag peak at 38.1^o and

the difference in the intensity and FWHM of the peak of the two samples lead to the calculation of the grain size in c axis. The crystal size was calculated using Scherrer's formula to be about 36 nm for the 0.4 Å/s and 24 nm for the 0.2 Å/s one, a difference of about 30%.

$$t = \frac{K\lambda}{dcos\theta} \tag{4.1}$$

where t is the mean size of the crystal, K the shape factor, λ is the X-ray wavelength, d is the full width at half maximum (FWHM) intensity of the peak and θ is the diffraction angle. The constant K, depends on the shape of the crystal and the size distribution. Assuming spherical crystals with cubic symmetry, the K factor was set to 0.94 for the size determination.

Bigger grains, means smaller number of grain boundaries and thus smaller resistivity is expected in the electron transport measurements. The step size that was used was 0.002^o and the counting time per step was 2 seconds.

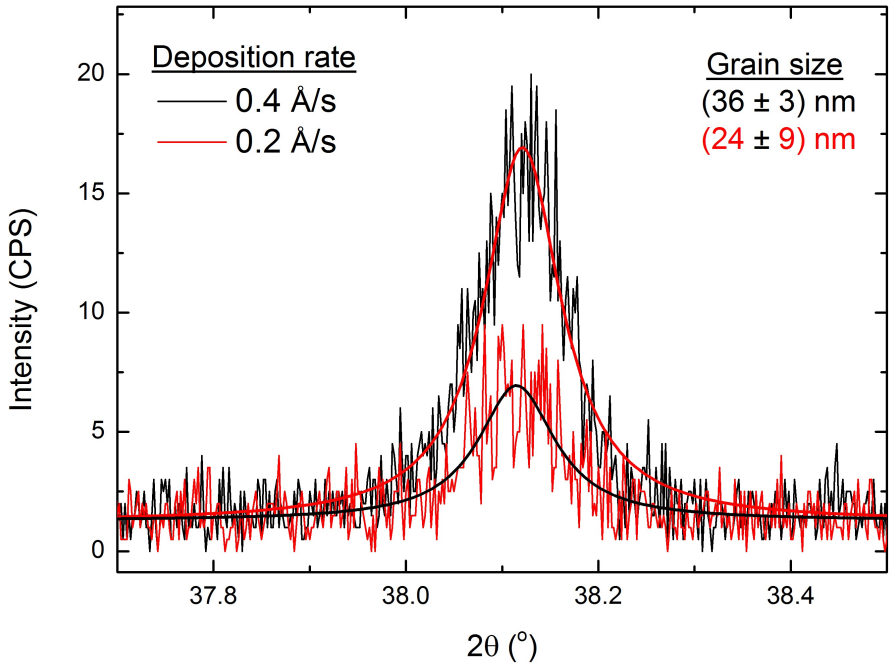

Figure 4.3: *High angle X-rays of the films, where it can clearly be seen that the grain size in the faster deposited NM is almost double, along with the 38.13^o peak, that corresponds to Ag (111).*

The actual size of the grains that the electrons experience during the transport measurements though, is the lateral size. The two Ag films had their grain size measured laterally using Scanning Electron Microscopy (SEM) as presented in figure 4.4.

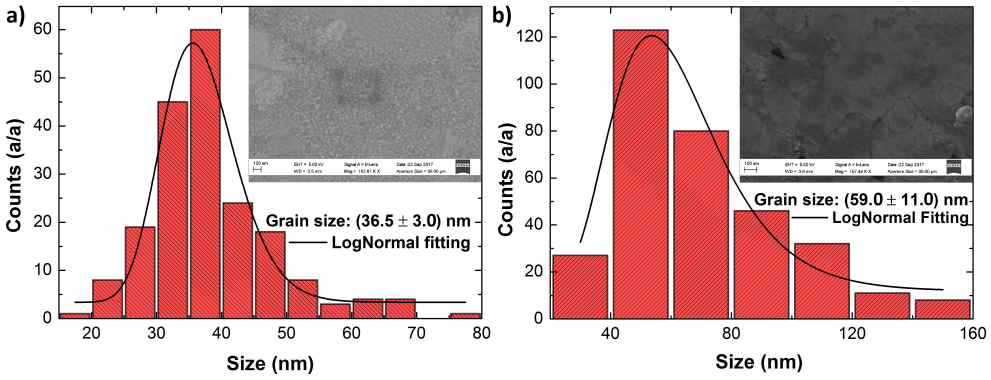

Figure 4.4: *In (a) is the lateral grain size distribution for the SEM images for the film grown using 0.2 Å/s rate. The mean size of the grains was measured to be (36.5 ± 3.0) nm. In (b) is the lateral grain size distribution for the SEM images for the film grown using 0.4 Å/s rate. Most of the film consists of large grains but there are areas where smaller grains were formed. The distribution presented is for these grains. It came out to be (59.0 ± 11.0) nm.*

The SEM imaging revealed that in the film deposited using a lower deposition rate, the mean size of the grain was (36.5 ± 3.0) nm. On the other hand, the 0.4 Å/s sample formed quite large grains, bigger than 300 nm. There were areas of the film though, that smaller grains had formed, possibly because of impurities, on the substrate. The mean size of these was measured to be (59.0 ± 11.0) nm.

The SEM imaging was the second non-destructive technique that proves that the deposition rate strongly affects the microstructure of the film and in extension that of the nanowires.

4.2.2 Electron transport properties of films

Both films had their resistivity as a function of temperature measured using the Van der Pauw technique [69]. The reason why electrical transport measurements are important is because we can get valuable information about the scattering in the sample and the mean free path of the electrons as a function of temperature. The scattering of the electrons in a metallic system at high temperatures is primarily due to lattice vibrations. The contribution of defects, impurities and grain boundaries on the other hand, can

determine the residual resistivity. Shrinking the dimensions to nanowires, geometrical parameters start to affect the transport behaviour. If the thickness and geometrical characteristics of the material are larger than the mean free path of the electrons, there is not a big contribution from scattering of the electrons on the surface of the film to the resistance. Reducing the dimensions of the specimen to a size that is comparable, if not smaller, to that of the mean free path, it means that the contribution from scattering to the surfaces of the sample is increased dramatically.

The temperature range used for the transport measurement of the films was from about 290 K down to liquid helium temperature.

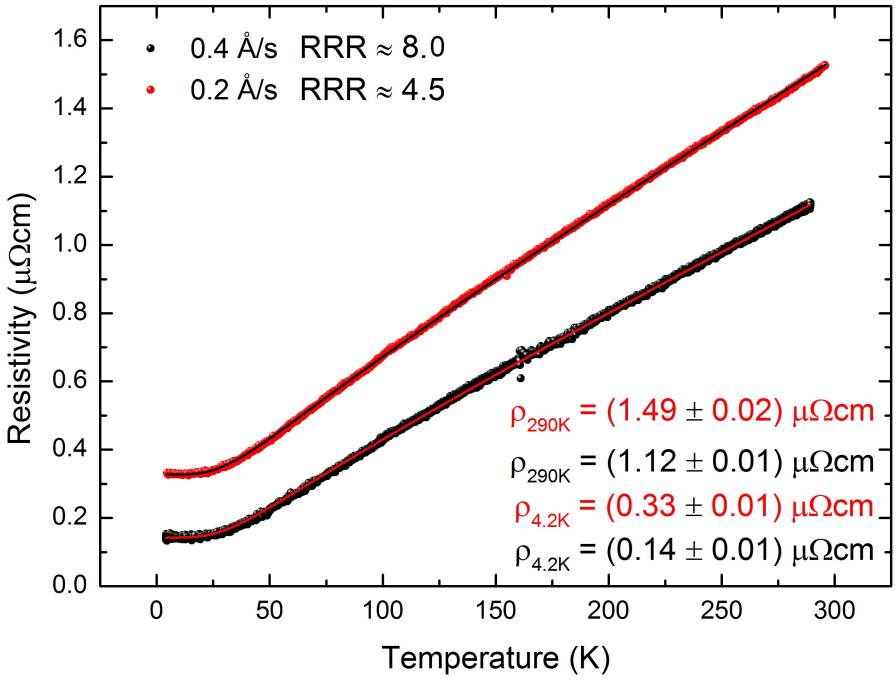

Figure 4.5: *Resistivity as a function of temperature for the two Ag films. There is an obvious difference in the resistivity with the deposition rate.*

As shown in figure 4.5, the resistivity of the films at 290 K is quite different, about 1.5 $\mu\Omega$cm and 1.1 $\mu\Omega$cm for the slow and fast grown sample. As the samples are cooled down to 4.2 K the difference in the quality of the structure can be seen in the residual resistivity. The resistivity at LHe temperature is about 0.33 and 0.14 $\mu\Omega$cm. The difference might look small but leads to a $RRR_{0.4}/RRR_{0.2}$ of 1.77, given that the $RRR_{0.4}$ was 8 and the $RRR_{0.2}$ was 4.5. The RRR value of a material is defined as the

ratio of the resistivity at room temperature over the resistivity at 0 K (or at 4.2 K in our case, as there were no signs of Kondo effect and hence the scattering was dominated by the lattice faults and impurities and thus the residual resistivity shouldn't change below 4.2 K).

The RRR value is a rough indication of how good a structure is. Since the structure is better with fewer grains and thus fewer grain boundaries, the residual resistivity is smaller as well. That means that in the lateral spin valve geometry, both the spin signal and spin diffusion length should increase by increasing the deposition rate. Fitting the resistivity data to the Bloch Grüneisen function the Debye temperature can be obtained. For the two samples the Θ_{Debye} was (186.8 ± 0.6) K and (185.7 ± 0.7) K compared to the bulk value of 225 K [40].

There are several features related to the material that can be calculated such as the relaxation time and the mean free path of the electrons, the diffusion constant and finally the DOS at the Fermi level. Given that the Fermi velocity for Ag is 1.39×10^{6} m/s and the number density of electrons is n = $5.85\times10^{28}\mathrm{m}^{3}$ [40], the momentum relaxation time can be calculated through:

$$\sigma = \frac{ne^2\tau_p}{m} \tag{4.2}$$

In equation 4.2, σ is the conductivity of the sample, e and m are the charge and mass of the electron (9.11×10^{-31} kg) and finally τ_p is the momentum scattering time. If the momentum scattering time is known, one can calculate the mean free path of the electrons by just using the equation:

$$\lambda_p = \tau_p u_f \tag{4.3}$$

With these values, the calculation of the diffusion constant is now available using:

$$D = \frac{1}{3}\tau_p\lambda_p \tag{4.4}$$

The last step is to use the diffusion constant and the temperature dependence of the resistivity to calculate the states at the Fermi level as a function of temperature. To connect them together we can use the

$$\sigma = e^2 g(E_F) D \tag{4.5}$$

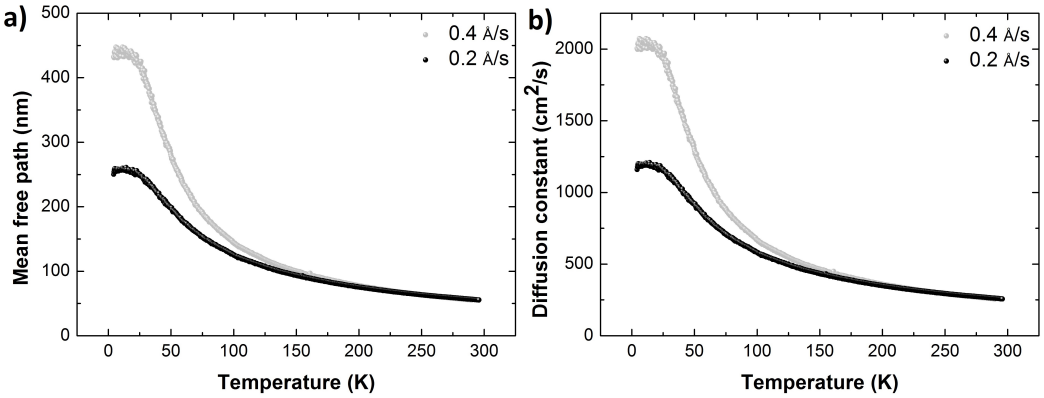

Figure 4.6: *Mean free path of electrons and the diffusion constant of the two films. Since all the aforementioned are directly or indirectly linked to the resistivity measured, both the mean free path and the diffusion constant are bigger for the one grown using a faster deposition rate.*

Combining the equations 4.1, 4.2, 4.3 and 4.4 we can find that the diffusion constant has a ρ (T) dependency since

$$g(E_F) = \frac{\sigma}{e^2 D} \tag{4.6}$$

Thus the number of states deriving from the calculation should be temperature independent and is about 10^{47} states per m^3.

The mean free path of electrons and the diffusion constant of the films are summarised in figure 4.6. It can be seen that they have the same increasing trend with decreasing temperature until about 30 K, where they turn temperature independent. In both cases the films where Ag was deposited faster, present longer mean free path and larger diffusion constant.

4.2.3 Electron transport properties of nanowires

For control samples, both FM and NM nanowires with dimensions similar to the ones used in the study were fabricated a SEM image of the nanowires along with the resistance as a function of temperature measurement is presented in figure 4.6. There is still no upturn below 10 K that could indicate the Kondo effect.

From the resistance as a function of temperature measurements the mean free path of the electrons and their diffusion constant were calculated as shown in figure 4.8.

A difference in the values compared to those obtained from the films is expected.

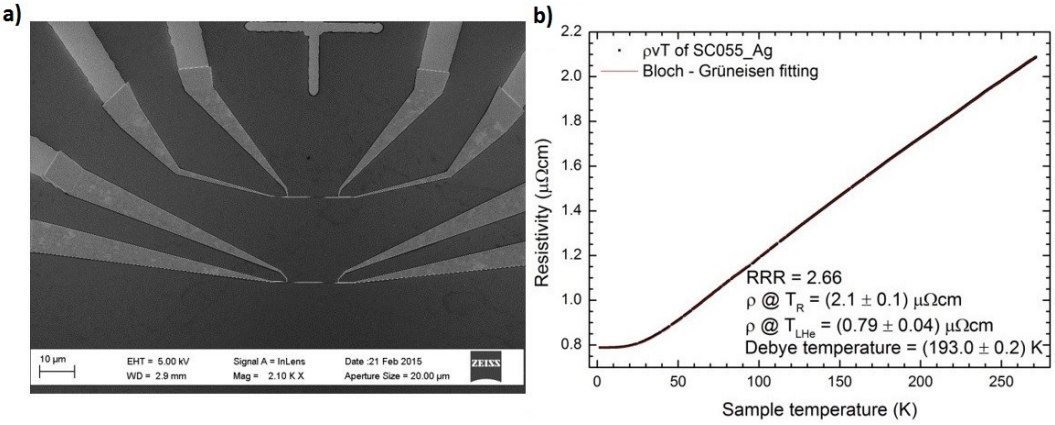

Figure 4.7: *In a) is a SEM image of two silver nanowires of different widths and 800 Å thick. In b) is a resistivity as a function of temperature measurement of one of the nanowires. By fitting the resistivity data to the Bloch Grüneisen function, we obtain a Debye temperature of 193 K for the nanowire. The value obtained for all the nanowires measured returned a Debye temperature of 196 ± 2 K while the bulk value is 225 K.*

The reason is related to the mean free path of the electrons. Since at temperatures below 50 K, figure 4.8, it is close the dimensions of the nanowires, the scattering from the wall on the normal metal channel is more pronounced.

The calculated relaxation time exhibited the expected behaviour. It increases with decreasing the temperature and the trend it presents follows the $1/\rho$ of the material. The above is concluded through equations 4.2, 4.3 and 4.4.

Work has been done using a permalloy nanowire as well. From the resistivity as a function of temperature data and using the empirical relation [36], the spin diffusion length in the ferromagnetic materials, and hence in Py, can be calculated and be used for the calculations of the spin diffusion length in Ag. It is shown in figure 4.9.

$$\lambda_{FM} = C_{FM} \frac{1}{\rho_{FM}} \tag{4.7}$$

with C_{FM} being a constant of 67.3 μ Ωcm^2 according to [70]. The calculated diffusion length was found to be close to values other studies had used [1, 51, 58, 64, 71, 72] for liquid helium temperature.

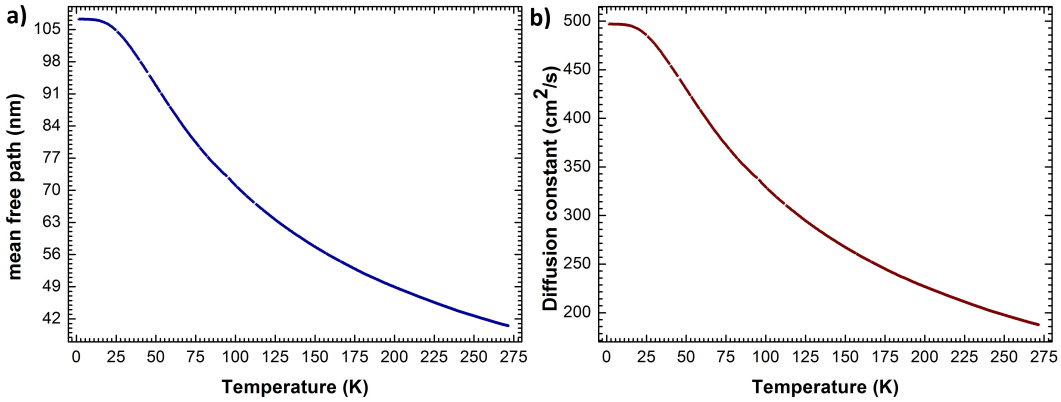

Figure 4.8: *Calculations of the diffusion constant and the mean free path of the electrons for a 80 nm thick and 100 nm wide silver wire. Both graphs exhibit the same behaviour having their lowest values at the high temperature regime and then plateau below 20 K. At that temperature regime, the mean free path is more than 100 nm.*

4.3 DC reversal method and analysis of the spin dependent part of the non-local IVs

4.3.1 DC reversal

The description of the DC reversal method has broadly been discussed in [1, 2]. It's a method suggested when using a set of a 6221A current source coupled to a 2182 nanovoltmeter in order to decrease the level of thermal noise in the measurement. Given that the signal that needs to be detected in the non-local measurements could be as low as nV, it is vital to minimise the level of noise. A very effective method used is called DC reversal and essentially it works as follows: A DC current is applied to the sample of interest in one direction and the voltage output is measured. After that the sign of the current is reversed and the voltage is remeasured. The difference of these two measurements divided by two is the voltage output for the sample. The error in the measurement decreases through averaging.

4.3.2 Electron transport in the normal metal channel

Before the spin transport measurements, an important parameter to be measured both for the calculation of the diffusion length and to confirm that the spin transport channel behaves in an ohmic way, is the transport channel resistance. Four out of the eight

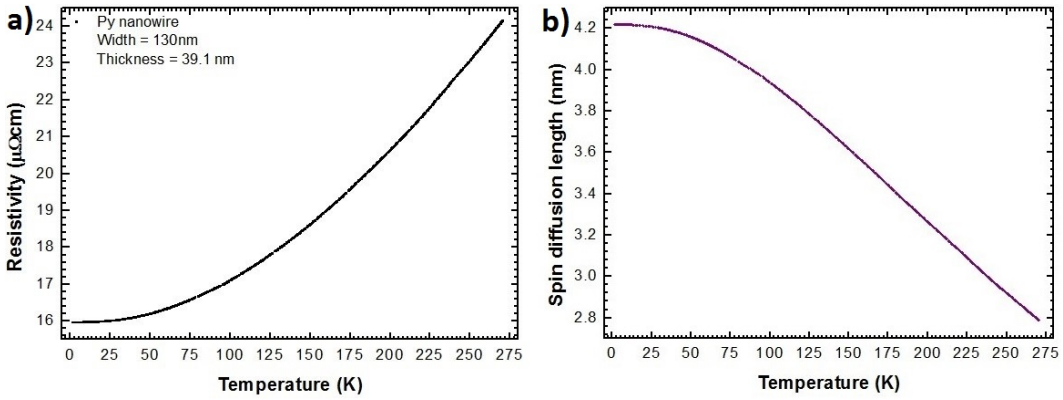

Figure 4.9: *Resistivity as a function of temperature of a 130 nm wide and 39 nm thick Py nanowire. The calculation of the spin diffusion length of the ferromagnet is on the right. It increases up to more than 4 nm at liquid helium temperature.*

contacts present in each device were used for the four point measurements. To measure the resistance of the spin transport channel, the contacts were chosen in such a way that local measurements were enabled. Given that the sample consists of nanowires, the resistivity should follow the

$$\rho = \frac{A * R}{L} \tag{4.8}$$

where ρ is the resistivity, A is the cross-sectional area, R is the resistance of the area of interest and L is the centre to centre ferromagnetic separation.

As expected for a sample that behaves normally, see figure 4.10, resistance increases in a linear way with the separation and the resistivity the devices present is 2.80 ± 0.03 $\mu\Omega$cm and 3.18 ± 0.03 $\mu\Omega$cm at 250 K. There is only one point that does not follow the trend that the rest of them present and that corresponds to the 1400 nm separation.

As explained in the previous paragraph, a quick way to find out how good a structure is using the electron transport data, is the RRR values the normal metal channels present.

In figure 4.11 is the RRR value of the devices across the different FM separations. The broad lines are the standard deviation of the means. The mean value of the RRR point of the devices grown slowly is 2.33 ± 0.06, smaller by 25% compared to the 3.06 ± 0.18 calculated for the fast grown samples. Although the RRR distribution of the latter is more scattered compared to the 0.2 Å/s, it is also undeniably bigger. This

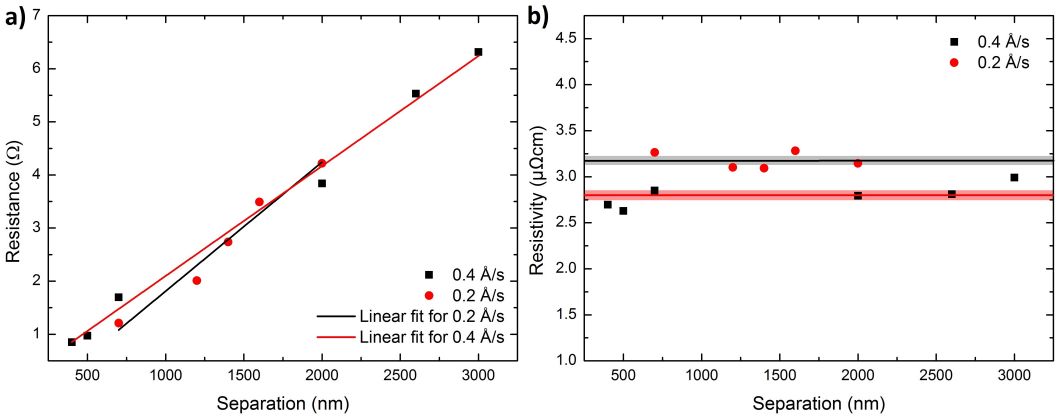

Figure 4.10: *Testing the devices to confirm ohmic behaviour across the different separations. In a) is the change of resistance as a function of FM separation at 250 K for the two sets of devices used, where its linear trend can be seen. In b) is the resistivity of the NM channel for the two sets of devices at 250 K. The difference in ρ is clear depending on the deposition rate used.*

means that since the channels should be geometrically identical, the pressure conditions were similar during the independent growths, and the source material was the same; the difference in the resistivity is related to the size of the grains and in extension the number of the grain boundaries.

Since the number of grain boundaries contributes highly in the spin scattering in the devices [58], it is expected that the spin signal of the two sets of devices, will be higher in these where the larger deposition rate used for the NM channel.

For all the lateral spin valves, the resistivity of the Ag channel was measured for each device, from 270 K down to 2 K. The resistivity of the clean channels exhibited no upturn, for example in figure 4.12, signature of the Kondo effect due to magnetic impurities. The Bloch Grüneisen function was fitted to the data to obtain a Debye temperature of about 190 ± 4 K, close to the 225 K of the bulk Ag [40].

For the comparison of the two samples of 2000 nm separation, figure 4.12 , the resistance of the sample grown with a lower rate, is bigger in the whole temperature range used. Furthermore, the residual resistance is lower, almost half the value.

To measure the spin diffusion length in the different sets, for the pure spin currents, the measurement configuration has to change to the one for non-local measurements. The reason why this IV type of measurements is called non-local, is because there is

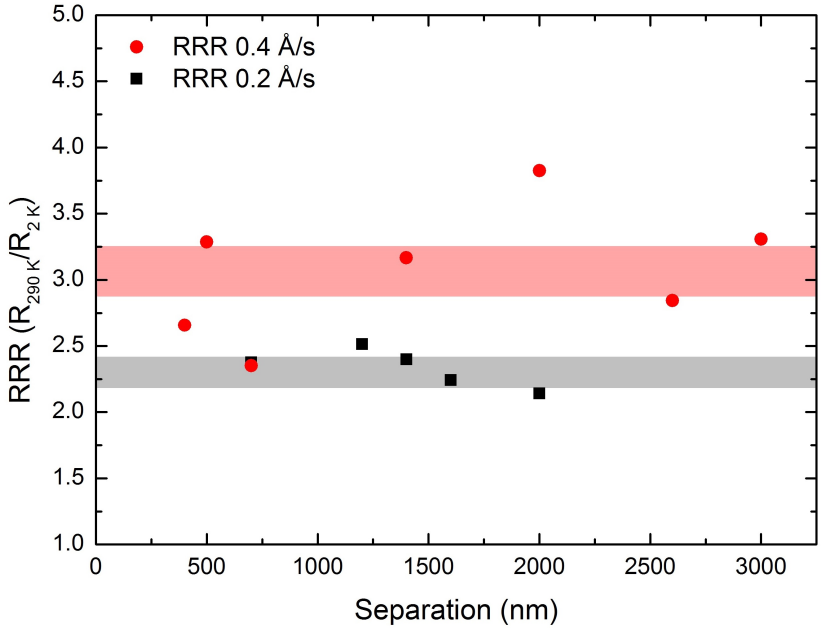

Figure 4.11: *RRR values of all the ferromagnetic separations for the two different batches of devices, where the points in red correspond to the high deposition rate and black the low.*

no crossover between the current and the voltage paths. At that point it is vital to understand what are the different contributions and voltages picked up by a non-local IV. A part of this contribution will be analysed in the following paragraph, while the other part will be analysed in chapter 5.

4.3.3 Linear component of the non-local IVs and spin related phenomena

Transport measurements were performed in a He gas flow cryostat. The techniques used for the measurements are the DC reversal and 4 point measurement. An external magnetic field of 100 mT was applied, as it was strong enough to fully saturate the ferromagnetic electrodes along their easy axis, and then swept to -100 mT and finally back to 100 mT to complete a full loop of the measurement. The reason why these field points were selected is because the ferromagnetic electrodes have a coercive field of 40 mT and 20 mT for the hard and soft pad respectively. The two ferromagnetic electrodes switch independently due to shape anisotropy. To measure the temperature dependence of the spin signal of the devices, the temperature is being stepped from 2

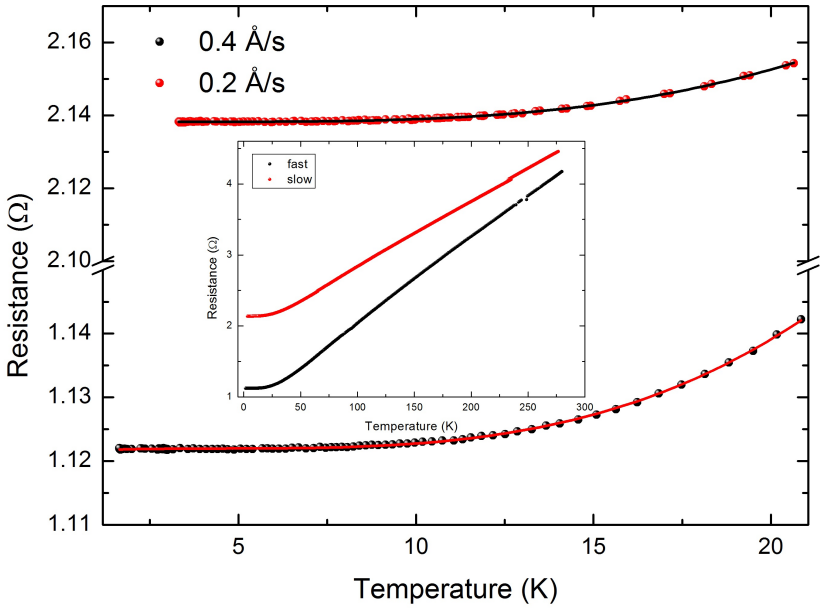

Figure 4.12: *Resistance as a function of temperature for two samples with the same 2000 nm ferromagnetic separation. In the whole temperature range the resistance of the samples grown with a higher rate is lower and since the high temperature slope is bigger, the RRR value is bigger as well.*

K up to 270 K. Once the rate of change in the temperature is less than 20 mK/min, full non-local IVs as a function of the external magnetic field were recorded.

For each field point a non-local IV was recorded and fit to a second order polynomial equation $V_s = aI + bI^2 + c$ [73], where V_s is the non-local voltage, I is the applied current, a is the coefficient of the linear component, b the coefficient of the quadratic component and c is an offset related to the nanovoltmeter.

From the measurements of the IVs and fittings can be obtained three different components. The field independent terms related to the heat transport effects are a linear term (a, due to the Peltier effect in the injector/normal metal junction), a quadratic term (b, due to the Joule heating effect) and a constant (c, offset from the nanovoltmeter). These terms are summarised in figure 4.13.

The average of the slopes of the parallel and antiparallel linear terms is a constant value for each field and temperature that derives from the Peltier effect and is called baseline resistance (BLR). The thermal related effects will be analysed properly in chapter 5.

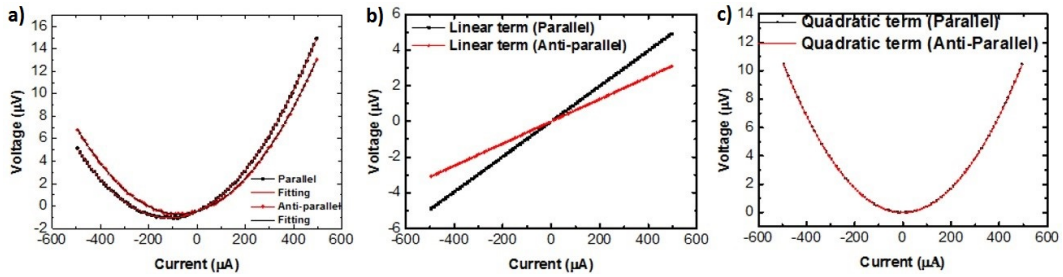

Figure 4.13: *In a) are the non-local IV characteristics of the Py/Ag/Py lateral spin valve for the parallel and antiparallel state. From the shape of the IV one can tell that it's a combination of two different contributions. A linear component (b), related to the spin signal, and a quadratic one (c) related to Joule heating while measuring.*

The field dependent terms related to the spin transport effects are a linear term (a, which is non-zero and related to the spin transport in the device), a quadratic term (b, constant at a fixed temperature as the dependency of Joule heating in our devices to field is zero) and a constant (c, offset from the nanovoltmetre).

The difference in the slope between the parallel and the antiparallel linear terms, that correspond to the non-local resistance for the parallel (R_P) and antiparallel state (R_{AP}), is called the spin signal [71]. It is proportional to the initial spin accumulation in the injector/normal metal vicinity [71], and can be written as:

$$\Delta R_s = R_P - R_{AP} \tag{4.9}$$

The difference of the non-local resistances between parallel and the antiparallel state, shown in figure 4.14 is the spin signal (ΔR_s) which is a normalised voltage, the non-local voltage divided by the applied charge current, as current is not applied directly on the parts where the potential difference is recorded. The FM electrodes are saturated at 100 mT and as the field is moving to -100 mT (red arrow) the soft pad reverses first, leading the system to the antiparallel state. By decreasing the field even more, the second FM reverses as well bringing the system back to the parallel state. The procedure is repeated by setting the field to 100 mT (green arrow) to repeat the phenomenon. By repeating the field sweeping at different temperatures such as from 2 K up to 270 K, one can get the temperature dependence of the spin signal accompanied with a thermal offset that will be explained in the next chapter. The magnitude of the spin signal is related to the initial spin polarisation and the quality of the NM channel.

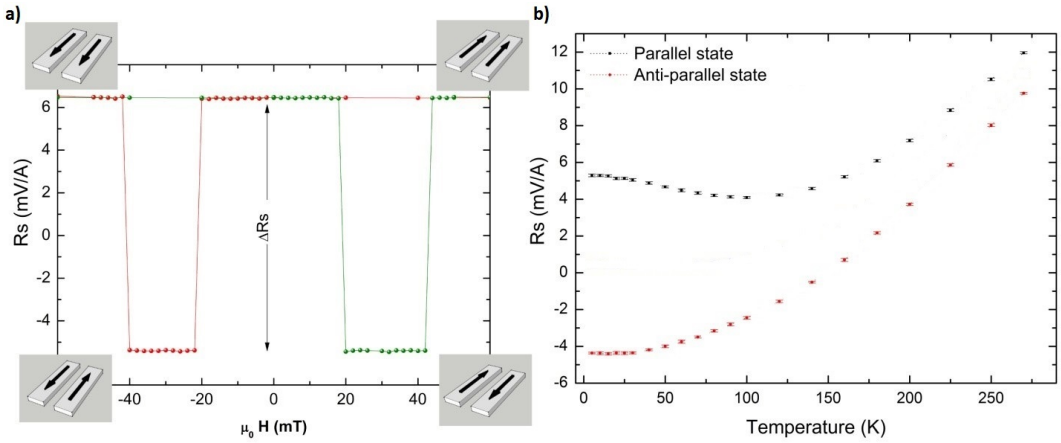

Figure 4.14: *A typical non-local resistance measurement in a lateral spin valve is presented in a). Following the red line and by sweeping the field to the negative values and back to positive ones, we push the electrodes through both parallel and antiparallel state. In b), is the R_s as a function of temperature.*

By plotting the spin signal at different separations of the ferromagnetic electrodes in this same temperature range, the spin diffusion length in the non magnetic metal can be calculated as shown later in this chapter.

As expected, the mean free path of the electrons is inversely proportional to temperature. This fact derives from equations (4.2) and (4.3) that were mentioned earlier. In (4.2) one can see that the momentum scattering time is inversely proportional to the resistivity. Given that in metals the resistivity is proportional to the temperature, the momentum scattering time should increase by decreasing the temperature. From equation (4.3) we have that the mean free path of the electrons is proportional to the momentum scattering time and thus proportional to the temperature as seen in figure 4.15.

4.4 Spin transport properties dependence on the growth rate of the normal metal channel

4.4.1 Spin signal

In all the R_s versus temperature measurements, as well as in the spin diffusion length calculation of the literature, there is an apparent downturn below 30 K [51, 52, 59,

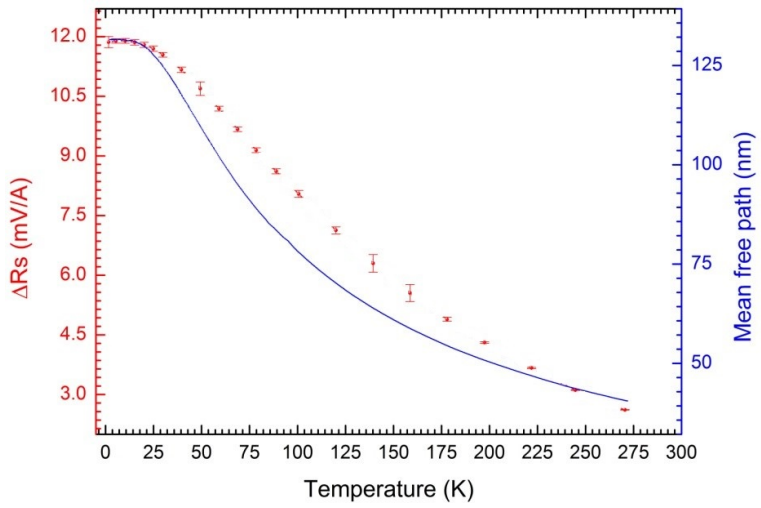

Figure 4.15: *A comparison between the spin signal and the calculated mean free path of the electrons in one of the devices. ΔR_s is simply proportional to the mean free path, where both plateau out below 20 K.*

64]. Many theories have been suggested so far to explain the behaviour but can be summarised into two categories: one that is related to the microstructure of the normal metal and the other one to the magnetic impurities in the system. Scattering that occurs in the oxidised outer sides of the normal metal channel (NM) or on the grains of the material belongs to the first one and another that it derives from scattering from magnetic impurities either in the edges of the NM or in the bulk. The suggestion in this study is that the answer is related to both the amount of magnetic impurities in the source material and the microstructure of the NM.

Two sets of devices were grown, the same 0.2 Å/s and 0.4 Å/s deposition rates that were used during the growth of the films, were used for the lateral spin valves as well. For those that the NM was deposited using a 0.2 Å/s rate the mean value of the RRR is 2.33 ± 0.06 while for those with 0.4 Å/s is calculated to be 3.06 ± 0.18 represented by the solid blue and red line accordingly in figure 4.11. Better crystal structure means less spin scattering from the grain boundaries and given that the source material was not changed and so the amount of magnetic impurities entering the system from the source is the same for the two sets of devices as it has already been suggested from Batley et al [64], a longer spin diffusion length.

By growing the Ag using a relatively high deposition rate (0.4 Å/s) as suggested

by Sennett et al. [68], the microstructure of the NM channel was improved. Surface diffusion causes Ag to agglomerate in islands when deposited, so a faster growth rate promotes the formation of continuous films and thus gives a higher quality structure. After the growth and the lift off, a 200 nm thick PMMA layer was spun on top of the devices to protect them from further oxidation. Interestingly, when the transport efficiency of the devices was measured, there was no downturn in the spin signal at low temperatures.

The spin signal has increased as can be seen in figure 4.16 for two devices with a FM separation of 1400 nm. In some cases the increase was more than a hundred per cent compared to the previous set and in all cases, for the common separations, the spin signal was bigger in the last set. Apart from that, the downturn recorded at about 30 K is present in the spin valves that were grown at a low rate, but absent in the ones with the higher rate. As there was no change in the purity of the material used for the growth of Ag in the K-cell, it means that the only thing changed is not the percentage of magnetic impurities, but the structure of the NM. Better structure would lead to less scattering from grain boundaries and so enhanced spin signal and spin diffusion length.

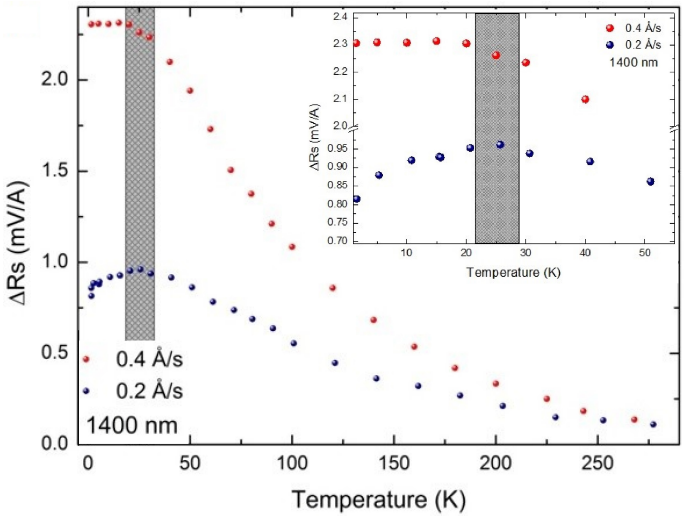

Figure 4.16: *A comparison of the spin signal between a slow (blue) and a fast (red) grown device with a separation of 1400 nm. The spin signal has significantly increased in the new samples and there is no apparent downturn below 30 K as shown in the inset of the image.*

According to R. S. Sennett and G. D. Scott [68] when silver is grown slowly (rate

0.2 Å/s) it tends to form islands that aggregate and grow in height before they join together (Volmer-Weber type) to form a continuous film. In the same paper, that happened approximately when 560 Å of Ag were deposited on the substrate while thinner films were discontinuous. Using a higher deposition rate the physical properties of silver would drastically change leading to a continuous film at thicknesses below 300 Å. Although a set of the devices in the current work were grown using a deposition rate of 0.4 Å/s and the other one 0.2 Å/s, the thickness of Ag that is evaporated is 1000 Å, thick enough to avoid discontinuities in the films.

4.4.2 Spin diffusion length

The transport properties of the devices that were fabricated using the high rate, compared to the ones that were made using the low rate, drastically improved leading to a diffusion length more than twice as long. As explained earlier, to calculate the spin diffusion length in Ag, what is needed is the fitting of the 1D transport equation in the spin signal as a function of the separation. The temperature dependence of the diffusion length can be obtained by fitting the data in the full temperature range that was used for the transport measurements.

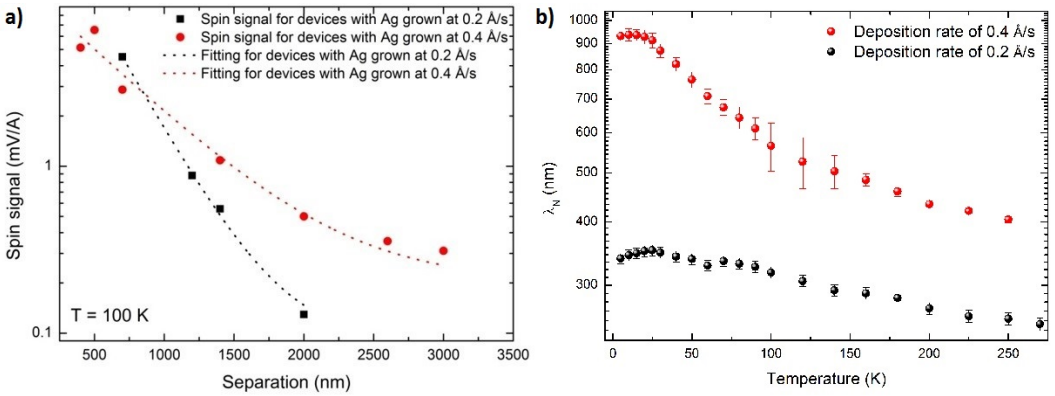

Figure 4.17: *In a) is the spin signal of the two sets of devices, as a function of separation, along with the fittings for sdl calculation. In b) is the diffusion length of those, with that of the fast grown devices to be larger in the whole temperature range. The striking feature is the lack of downturn at low temperatures.*

Figure 4.17 a is a comparison of the spin signals measured for different separations at 100 K for the slow (black) and fast (red) deposition rate devices. The non-local spin

signal of the devices with the slow rate dies off faster than those grown using a higher rate, for the whole temperature range. It is thus expected that the spin diffusion length of the devices with the 0.4 Å/s rate would be longer.

Finally, figure 4.17 b is a comparison on the spin diffusion length of the two sets of devices as a function of temperature. In the fast grown ones, where the deposition rate of silver was doubled, the diffusion length has increased and in some cases by more than 100% (low temperatures). Interestingly the spin diffusion length of the devices with 0.2 Å/s rate increases as the temperature decreases and peaks at approximately 25 K with λ_N to be 351.4 $\pm$ 8.6 nm. Below that temperature there is a monotonic decrease in the sdl. On the other hand, the sdl of the devices with 0.4 Å/s presents a similar behaviour but the peak has moved to 15 K. Below that temperature, the sdl decreases with a change of about 5% and within the experimental error.

Through the fittings, spin polarisation of the 0.4 Å/s samples was extracted as well the temperature dependence of which is shown in figure 4.18.

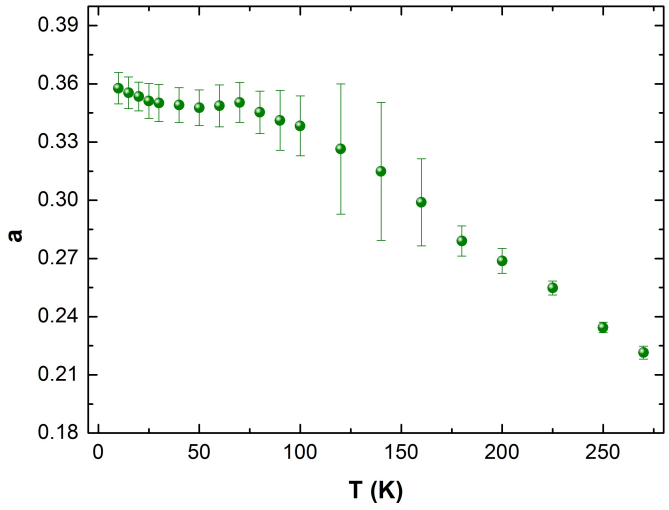

Figure 4.18: *Spin polarisation as a function of temperature in green, for the Py electrodes.*

The response of the spin polarisation is increasing as a function of decreasing temperature and at about 50 K the signal stabilises at about 35%, value that agrees with values obtained from other groups that used Py as the FM electrodes.

In figure 4.19 is a direct comparison of the mean free path of the electrons and the spin diffusion length of the devices with 0.4 Å/s deposition rate as a function of temperature. The two features present a similar trend as a function of temperature.

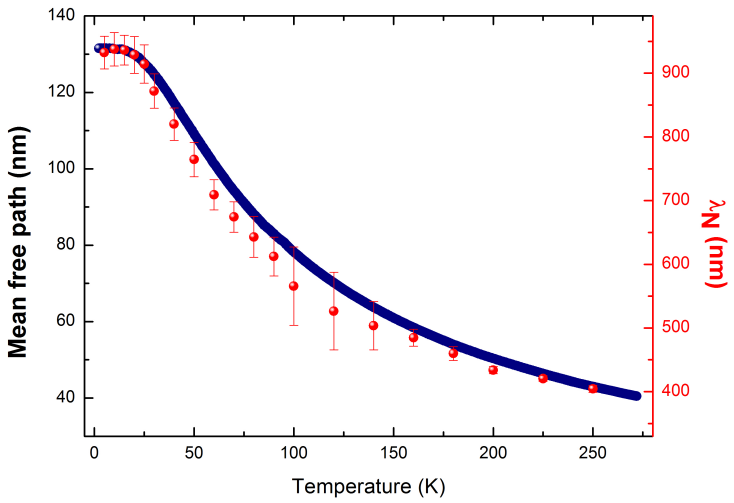

Figure 4.19: *Comparison of the spin diffusion length as the devices where a high deposition rate was used, against the mean free path of the electrons.*

The reason is that since the spin diffusion length can be calculated as:

$$\lambda_{NM} = \sqrt{\tau_s D} \tag{4.10}$$

Combining equation 4.9 with 4.4 leads to a direct comparison of the two where the diffusion length is proportional to the mean free path.

4.5 Conclusions

Two sets of lateral spin valves were grown using 0.2 Å/s and 0.4 Å/s deposition rate for the NM channel, while 0.1 Å/s was used in both growths for the FM electrodes. The idea of the experiment was to test how much the diffusion properties in the NM channel can be affected by its structure given the existence of magnetic impurities in the source material.

The interesting thing that can be concluded from the measurements of the films and the nanowires is related to the resistance and the spin signal as a function of temperature. There was no upturn at low temperatures in the resistance measurements in any of the two sets that would indicate scattering from magnetic impurities. The devices that were grown using a low rate presented a downturn in the spin signal. That could be an indication that the spin transport measurements are more sensitive to the magnetic impurities than the electron transport measurements. Behaviour that agrees with the observations of Villamor et al. [2].

It has already been proven that the downturn in the ΔR_s is related to the existence of magnetic impurities in the NM channel [52, 60, 64] and that the spin scattering from the grain boundaries is stronger than that from the walls [58, 62, 63]. The latter combined with the fact that the purity of the source material used for all the films and LSVs was the same 99.99 % and that impurities tend to segregate to the grain boundaries [74] can lead to two more conclusions.

By growing faster the Ag channel, we can improve the structure, the grain size and in extension the resistivity and the spin diffusion length. Furthermore, the small amount of magnetic impurities that pre-exist in the source have enough energy to migrate to the grain boundaries of the structure, when the source temperature is higher in order to achieve a higher rate, where the scattering from the grain boundaries prevails leading to the absence of downturn in the spin signal.

Chapter 5

Heat diffusion properties of lateral spin valves

In this chapter, we analyse the heat diffusion in lateral spin valves. We use the linear and quadratic field independent parts of the non-local IVs that are related to the thermal effects of the system. We separate the Joule heating and Peltier effect contribution from 270 K down to 2 K and measure their diffusion lengths in the same temperature range. Finally, we map their heat spatial distribution at room temperature for the first time in a lateral spin valve.

We also investigate the possibility of the influence of the Peltier effect. The aim is to understand the thermal effects in LSVs where spin currents flow. However, in order to remove the spin-dependence of the Seebeck effect and study just the heat flux, we fabricated V/Ag LSVs.

5.1 Introduction

The thermal properties and generated voltages of non-local spin valves are crucial as in delicate devices heat could lead to electromigration in the NM channel, which in turn could potentially be fatal for their performance [1, 18, 75–77]. The non-local geometry is ideal to study that, as one can separate heat, charge and spin currents and thus it is possible to study the effect of those independently [73, 78–81]. What is missing so far from the literature, is the deconstruction of the NLIVs to their spin and thermal components with a focused interest on the temperature dependence of the latter.

Garzon et al [82] in 2005, observed an asymmetric temperature dependence of the non-local resistance for the different relative magnetisation orientation of the injector and detector. A temperature dependent spin-flip interfacial scattering model was used for the interpretation of the data collected. This idea has since been discarded.

In 2007, Johnson and Silsbee [10] suggested that as the lateral spin valves are far from the ideal 1-D model; the spin injection and detection is not homogeneous across the width of the normal metal wire. This deviation from the ideal case, leads to local variation of the voltage that appears in the measurements as an offset in the non-local resistance as a function of temperature, known as the baseline resistance (BLR).

Casanova et al [1] observed two different background signals. Aside from the explanation of Johnson and Silsbee [10], Joule heating was suggested as a contribution to the thermoelectric voltage that was picked up.

Bakker et al [73], demonstrated that thermal effects are responsible for the baseline resistance. As in the non-local geometry the applied charge current and measured

voltage paths are completely separated, in the absence of spin accumulation there should be no voltage drop in the detector. However, the non-local resistance R^P and R^{AP} as a function of temperature, present a shift in their signal as the temperature increases. That means that the detector voltage is not purely from the spin transport.

Finally, Kasai et al [83] studied the non-local spin transport in Py/Cu/Py LSVs using thermally oxidised SiO_2 and MgO substrates. It was concluded that the spin signal was the same within the error in both cases, irrespective of the substrate used. However, using a substrate with high thermal conductivity, it was managed to dramatically decrease the magnitude of the baseline resistance.

The thermal effects picked up during the non-local measurements have been given little attention in the literature [73, 79, 81, 83–86] compared to the spin transport properties.

Here we present a deconvolution of the thermal effects using the non-local geometry and a study of their behaviour as a function of temperature and separation. Furthermore, Scanning Thermal Microscopy was used for the first time on lateral spin valves to map the temperature topography of the Joule heating and Peltier effect generated in one of the measured devices.

Furthermore, we explore the behaviour of the thermal effects by changing the parameters used during a measurement. What can be controlled and altered are the temperature, external magnetic field, including magnitude and direction, current sign or the combination of those. The temperature and external magnetic field behaviour have been studied and presented in chapter 4 for the spin transport and in this chapter for the heat transport and the current sign dependency of the effects. Since the Peltier effect is linear in the current [5, 73, 79], it is expected that the BLR behaviour should depend on whether we apply the positive or negative counterpart of the current.

Different combination of materials that were measured across 3 different cryostats with 3 different transport sticks and 2 different sample holders are included in this chapter to support the phenomenon. The $Co_{70}Fe_{30}$/Cu/$Co_{70}Fe_{30}$ LSVs were fabricated and measured by my colleague, Miss Katie A. Moran, the Py/Cu/Py LSVs were fabricated and measured by my former colleague Dr. Joe T. Batley and the Py/Ag/Py, Py/Ag(Fe)/Py, LSVs along with the V/Ag/V devices in the lateral geometry were fabricated and measured by the author. The analysis of the data obtained from all the different devices was completed by the author.

5.2 Heat related phenomena in non-local spin valves

5.2.1 Joule heating and Peltier Effect

The reason why thermal effects are present in the measurements, is related to the way that the pure spin currents are excited in the non-local spin valve geometry [71]. The fact that a charge current is flowing through a metal (Permalloy injector) will give rise to Joule heating the outputs of which is proportional to I^2R. The charge current will flow through both Py and Ag, but since the resistivity of Py is an order of magnitude higher than that of Ag as shown in figure 5.1, it can be considered as the main Joule heating source of the circuit.

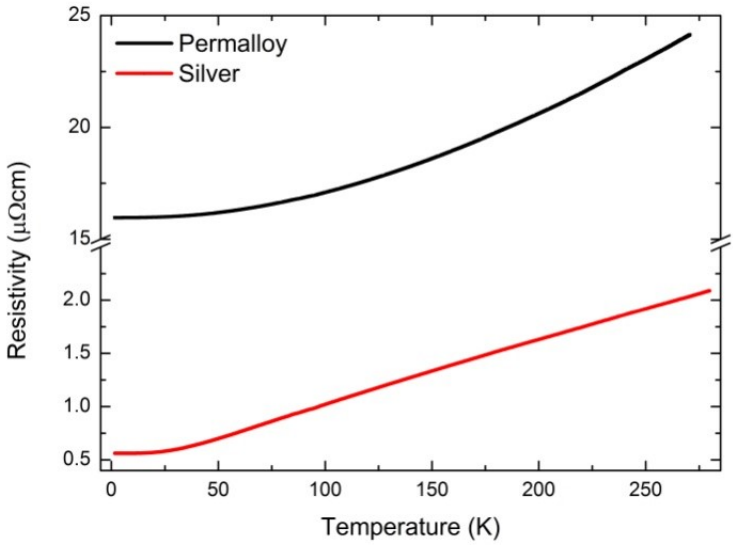

Figure 5.1: *Comparison of the resistivity of a Ag and a Py nanowire, with geometrical features close to the nanowires of the LSVs. The resistivity of Py is more than an order of magnitude larger.*

Because of the shadow deposition [45], there is a part of the circuit just before the junction, where only Py has been deposited. Current will flow through the less resistive part of the device, but since only Py has been deposited there, it has to pass through that part. As it will be shown later, that is the part that heats up the most.

Following the current path as presented in figure 5.2, it flows through the first

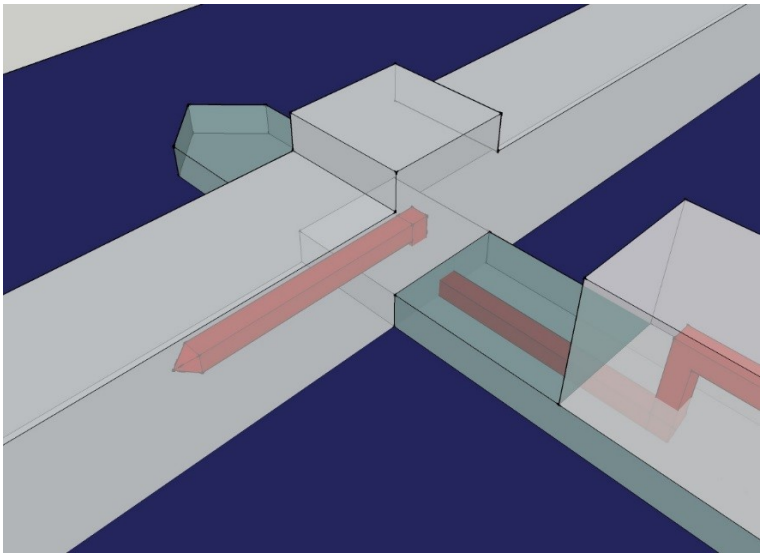

Figure 5.2: *Cartoon of the Py/Ag junction at the injector side. In red is the current path from the injector (green), through the NM (grey) and out from the left hand side away from the area between the FMs.*

bimetallic junction (Py/Ag in our case). The different metals have different number of conduction electrons and in order to maintain the current density between the two metals, energy has to be transfered from one part of the junction to the other [5], as it has already been presented in chapter 2. That means that a part of the junction is being cooled down (energy transfer) whilst the other is being warmed up (energy absorption). As the Peltier effect is linear to the applied current, it transfers energy to one side of the junction and removes energy from the other side depending on the current direction [5].

The heat current produced by both Joule heating and the Peltier effect diffuses along the normal metal channel and into the substrate. Although the thermal conductivity of Ag is about two orders of magnitude higher than that of the SiO_2 [5, 84, 87], their areas are very different. For that reason a K_{eff} will be defined. The first question that arises is, how does that heat flow propagate along the device? The easiest way to get an answer on that, is to actually image it. The method selected here was through the Scanning Thermal Microscopy.

5.3 Scanning thermal microscopy imaging of the NLSVs

Thermal imaging was taken using Scanning Thermal Microscopy (SThM) imaging technique. The measurements were performed in IBM Zürich, by Dr Fabian Menges and Dr Bernd Gotsmann. A detailed explanation of how the technique works can be found in Dr Menges's PhD dissertation [88] and related articles [9, 89, 90]. In two words though, the apparatus behaves like an Atomic Force Microscope (AFM), with an adjusted tip. The tip is covered with Palladium (Pd), a resistive element that can heat up its surroundings with Joule heating when a current is flowing through. To calibrate the instrument, the resistance of the tip is being measured while the tip is being warmed up. To make sure that the tip is in thermal contact with the sample, the thermal conductance between the two is measured and once a drop is picked up, it means that the tip has reached the sample or the area of interest in general. The device is supplied with current that will lead to a temperature increase. Scanning the sample at the elevated temperature region with the tip will lead to the change in resistance of the active part of the tip. As the tip has already been calibrated, the difference in resistance can be matched to temperature difference across the device.

The key point of the apparatus is that the measurements were performed under high vacuum conditions and thus oxidation phenomena can be avoided. The drawback of this technique is that once a part the sample/device is scanned, it cannot be re-scanned with the same tip for the sake of statistics. The reason why is because as the tip scans the sample, it wears off. That will modify the tip and so the temperature profile will eventually differ.

For the data that were recorded by the SThM an AC current source and a lock-in amplifier were used to pick up the signal. The amplitude of the signal was 1.6 mA, three times larger compared to what used for the non-local measurements, in order to increase the magnitude of the thermal signal. The measurements were performed at room temperature in a high vacuum chamber, in order to avoid heat conduction through air between the tip and the sample. The method used can detect independently the two thermal components as the Peltier term is linear to the applied current whereas the Joule heating term has a quadratic dependence and can be detected via the higher harmonic response of the probe.

Joule heating as a heat source is related to the resistance of the metals as the produced heat is proportional to I^2R, where I is the charge current used and R the

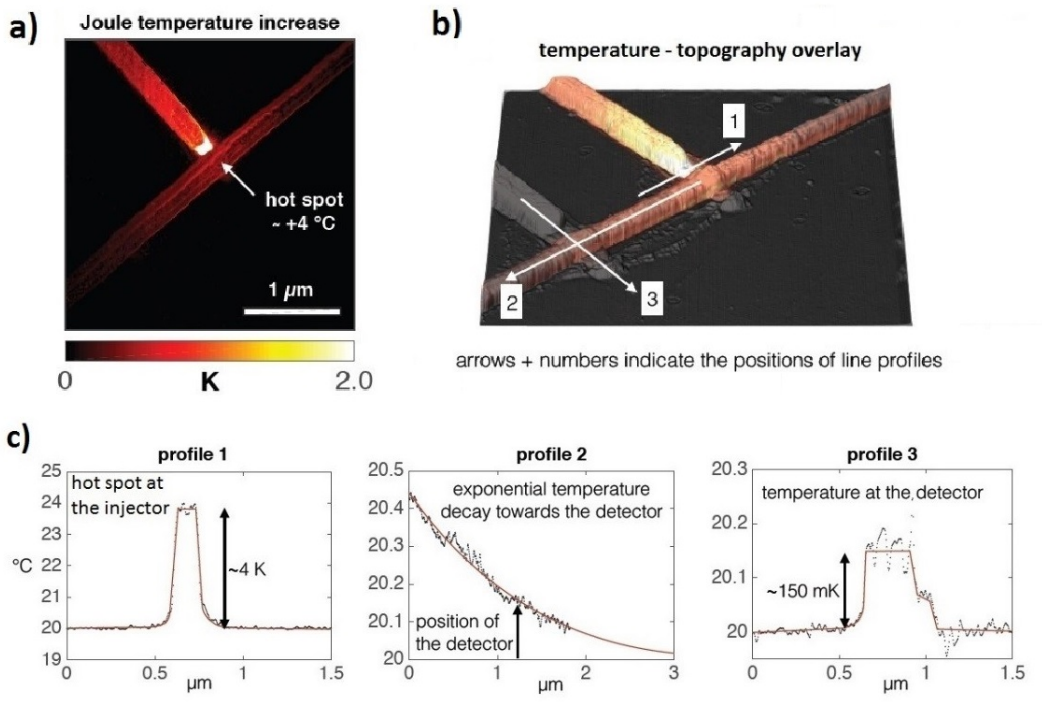

Figure 5.3: *Top row a) and b, is an image obtained using the Scanning Thermal Microscope technique focused on the quadratic term. The arrows on the different parts of the device indicate where the temperature profiles where measured. Finally in c) is the temperature distribution across the main parts of the device.*

resistance of the element. The thermal imaging, confirmed that the warmest part of the circuit was the spot where only Py had been deposited, due to the shadow evaporation, as the temperature increased by 4.4 ^{o}C (arrow 1 in figure 5.3) at this specific part. The images can confirm that heat transfer through the substrate is negligible compared to that along the normal metal channel, as expected.

The temperature decay along the silver channel as shown in figure 5.3 is represented by arrow 2. The temperature decays in an exponential way agreeing with the theoretical predictions. Following arrow number 3, one can see how the temperature profile changes across the detector FM_2. The temperature is almost constant before reaching the junction with a tiny increase of about 16 mK/μm. At the detector junction the temperature difference increases by 150 mK and fluctuates until the end of the junction. The signal is followed by a shoulder of about half the difference in temperature, indicating that the tip is above the clean Py a bit closer to the front end of the arrow.

After that, scanning the substrate, the temperature difference levels at zero.

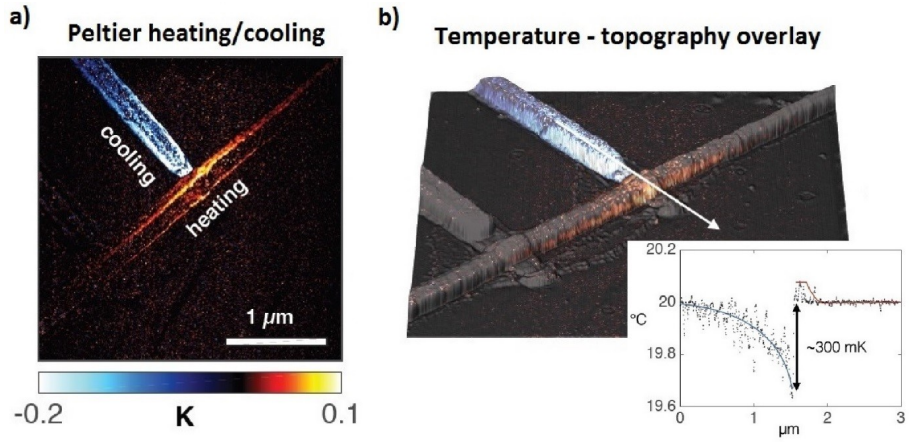

Figure 5.4: *a, b) Imaging of the Peltier cooling and heating of the injector of a Py/Ag/Py LSV of 1200 nm separation measured at room temperature. The device acts as a temperature dipole between the injector and Ag. c) Exhibits how the temperature is evolving across the arrow from the Py/Ag bilayer to the pure Py, where we have the coldest part, and then to the Ag/Py junction.*

In the Peltier term in figure 5.4, the temperature is decreasing as the scan approaches the injector/NM junction. There is a temperature drop from 20 ^{o}C down to almost 19.6 ^{o}C and then once it's on top of the junction the temperature increases up to about 20.1 ^{o}C only to drop back down to 20 ^{o}C for the substrate. This thermal component exhibits some heat spreading on the substrate as shown in figure 5.4 that is negligible due to two different reasons. Firstly is because of the fact that the heat conductance of the SiO_2 layer is a lot smaller compared to Ag and secondly because the holder used for the transport measurements is made out of oxygen free Cu and acts as a very efficient thermal bath [48]. Unfortunately the temperature drop in the detector junction cannot be resolved as it is not in the resolution limits of the experimental apparatus. Given that the relative temperature drop in the detector and injector junctions due to the different thermal effects should be the same, it is possible to calculate the ΔT in the detector junction due to the Peltier term. The temperature change in the two junctions due to Joule heating presents a difference of about 34%. That means that since the temperature change in the injector junction due the Peltier term is about 300 mK, the ΔT in the detector should be about 90 mK.

To complement the collected data, at least one more technique is needed and also

a theoretical model that predicts the heat dissipation along the NM channel. An analytical model was developed for that reason and also transport measurements were performed on the lateral spin valves used.

5.3.1 Heat propagation and detection

An analytical model was built in order to predict the temperatures of the injector and detector junctions, along with the heat diffusion along the NM channel.

Considering a cell of length dx, width w and thickness t, the heat diffusion into the channel can be calculated. The heat flow into the cell is $\dot{Q_{in}}$ and will equal the sum of the heat that flows through the substrate $\dot{Q_s}$ plus the heat flow that leaves the cell $\dot{Q_{out}}$. The total expression is:

$$\dot{Q_{in}} = \dot{Q_s} + \dot{Q_{out}} \tag{5.1}$$

The heat flow that comes out of the cell will be:

$$\dot{Q_{out}} = \dot{Q_{in}} + \frac{d\dot{Q_{out}}}{dx}dx \tag{5.2}$$

The heat flow through the substrate will be:

$$\dot{Q_s} = wh(T - T_s)dx \tag{5.3}$$

where h is $\frac{K_s}{\delta}$, K_s is the thermal conductivity of the substrate and δ is the interface width between the substrate and the cell. Considering a point far away from the heat injection, we should have:

$$\frac{d\dot{Q_{in}}}{dx}dx + wh(T - T_s)dx = 0 \tag{5.4}$$

Since the heat flow that enters the cell is related to the temperature change as a function of distance and the thermal conductivity of the material with

$$\dot{Q_{in}} = -KA\frac{dT}{dx} \tag{5.5}$$

where K is the thermal conductivity of the wire and A is the cross-sectional area that equals to tw. Differentiating the above will lead to:

$$\frac{d\dot{Q_{in}}}{dx} = -KA\frac{d^2T}{dx^2} \tag{5.6}$$

Using equation (5.6), the equation (5.4) changes to:

$$\nabla^2 T - \frac{wh}{KA}(T - T_s) = 0 \tag{5.7}$$

Writing T' = T-T_s and $\frac{wh}{KA}$ equals to α ^{2} we can write:

$$\nabla^2 T' - a^2 T' = 0 \tag{5.8}$$

which is Fourier's law. The general solution to the equation is:

$$T'(x) = B_1 e^{ax} + B_2 e^{-ax} \tag{5.9}$$

Two boundary conditions can be used. The first one is at the heat flow injection point, x = 0, and the second one is at a position far away from the injection point, x = L, where the change of the temperature as a function of distance would be zero. The last equation combined with T' = T-T_s will give

$$T'(0) = T_{in} - T_s = B_1 + B_2 \tag{5.10}$$

and

$$\frac{dT'}{dx}|_{L=x} = 0 \implies B_1 a e^{aL} - B_2 a e^{-aL} = 0 \tag{5.11}$$

which means that

$$B_1 = B_2 e^{-2aL} \tag{5.12}$$

Using equation (5.12) in (5.9) leads to:

$$B_1 e^{aL} + B_2 e^{aL} = B_2 e^{-aL} + B_2 e^{aL} \implies e^{aL}(B_1 + B_2) = 2B_2 cosh(aL) \tag{5.13}$$

It has already been calculated that $B_1 + B_2$ is T_{in} - T_s so that last equation changes to:

$$e^{aL}(T_{in} - T_s) = 2B_2 cosh(aL) \implies B_2 = \frac{e^{aL}(T_{in} - T_s)}{2cosh(aL)} \tag{5.14}$$

The coefficient has already been calculated in relation to the B_2 coefficient through equation 5.12 and so by replacing B_2, B_1 is:

$$B_1 = \frac{e^{-aL}(T_{in} - T_s)}{2cosh(aL)} \tag{5.15}$$

Replacing B_1 and B_2 in $T^{'}(x)$ results in:

$$T'(x) = \frac{T_{in} - T_s}{2cosh(aL)}[e^{-aL}e^{ax} + e^{aL}e^{-ax}] = (T_{in} - T_s)\frac{cosh(a(x-L))}{cosh(aL)} \tag{5.16}$$

and since $T^{'}$ = T - T_s, T(x) is finally

$$T(x) = (T_{in} - T_s)\frac{cosh(a(x-L))}{cosh(aL)} + T_s \tag{5.17}$$

The last equation predicts an exponential decay type of heat flow along the normal metal channel as a function of separation. The prediction agrees with experimental data both from the scanning thermal microscopy (see figure 5.3, 5.5) and the transport measurements as will be shown later on the chapter. It is important to mention here, that equation (5.17) has only one fitting parameter, δ. The latter, is related to α through equation 5.8. That is the interface width for the temperature gradient between Ag and the substrate and resulted to be about 50 nm.

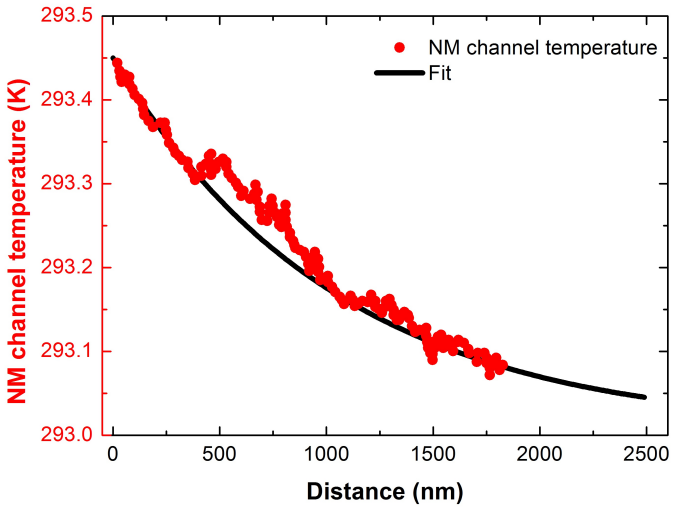

Figure 5.5: *Fitting of the experimental data recorded using the SThM, with equation 5.17.*

To find the injector temperature as a function of sample temperature it is assumed that the steady state has been reached. At that point, the sum of the Joule and Peltier

terms generated at the injector, should be equal to the heat dissipation to the substrate and the metal surroundings:

$$i^2R + iT_iS_{eff} = \zeta K_{eff}(T_i - T_s)$$

where S_{eff} is the difference in the Seebeck coefficients of Py and Ag. The injector circuit has a large surface area with the substrate but a low thermal conductivity, as opposed to the NM channel that has a very large thermal conductivity but a rather small area. An effective thermal conductivity (K_{eff}) and $\zeta = A/\delta$ are defined, where A/δ is the ratio of the area to the interface width. Since the temperature of the injector was measured from the SThM, the K_{eff} can be determined by choosing a value that gives a detector voltage that is typically measured. Term ζ is related to δ which depends on the K_{eff}. That means that by determining K_{eff}, ζ can be calculated and should also be temperature independent.

$$\zeta = \frac{i^2R(T_o) + iT_i(T_o)S_{eff}(T_o)}{K_{eff}(T_o)(T_i(T_o) - T_o)}$$

where $T_o = 300$K is the temperature used in the SThM. The temperature of the injector $T_i(T)$, can be calculated using:

$$T_i(T) = \frac{i^2R(T) + \zeta T_s(T)K_s(T)}{\zeta K_s(T) - iS_{eff}(T)} \tag{5.18}$$

Therefore ζ scales the substrate thermal conductivity to take account of the higher losses. Equations 5.17 and 5.18 can be used to determine the detector temperature (T_d) as a function of temperature which is then used to predict the detector voltage as:

$$V(T) = S(T) * (T_d - T_s) \tag{5.19}$$

Where $S(T)$ is the effective Seebeck coefficient of the detector junction (S_{Ag}-S_V) and T_s is the substrate temperature.

The model predicts that the temperature difference between injector and detector as well as detector and substrate for the Py/Ag system, is almost constant down to about 100 K as presented in figure 5.6. Below 100 K, the temperature difference increases significantly to up to 3 K above the substrate temperature for the injector and more than 1.5 K for the detector at 8 K.

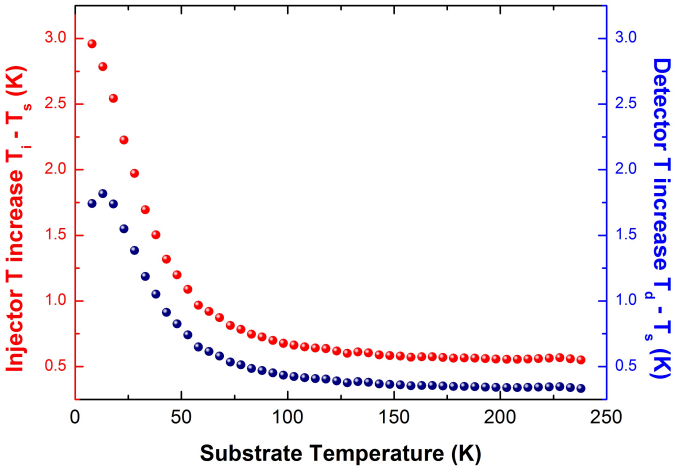

Figure 5.6: *Temperature increase for the injector above the substrate (in red) and the detector from the substrate (in blue) as a function of temperature, as predicted by equations (5.17) and (5.18).*

5.4 Manipulation of the thermal response with the Seebeck effect

Since what transforms the temperature difference to potential difference in the detector junction is the Seebeck effect, that implies that by choosing the correct combination of materials the sign and the magnitude of those can be manipulated. Ag was the transport channel but Vanadium (V) was chosen as the thermal injector and detector instead of Py. The change was performed due to the fact that without Py and the resulted spin accumulation, two NM in contact can provide a simpler system to study the Peltier and Joule heating effects.

The combination of materials selected was 60 nm of Vanadium (V) for heat injector and detector and 120 nm of Ag for the heat transport channel. The widths of the nanowires were the same as those used for Py in chapter 4 and the SThM experiment. The geometry used for the experiment was the same as the lateral spin valve geometry.

The idea behind the experiment was two-fold. Firstly to confirm that the linear, Peltier related part of the non-local IVs is field independent and not affected by the presence of a FM. Secondly, since the effective Seebeck coefficient of a bimetallic junction defines the conversion of the temperature gradient through the junction to potential difference, by carefully selecting the materials of the junction one can manipulate the

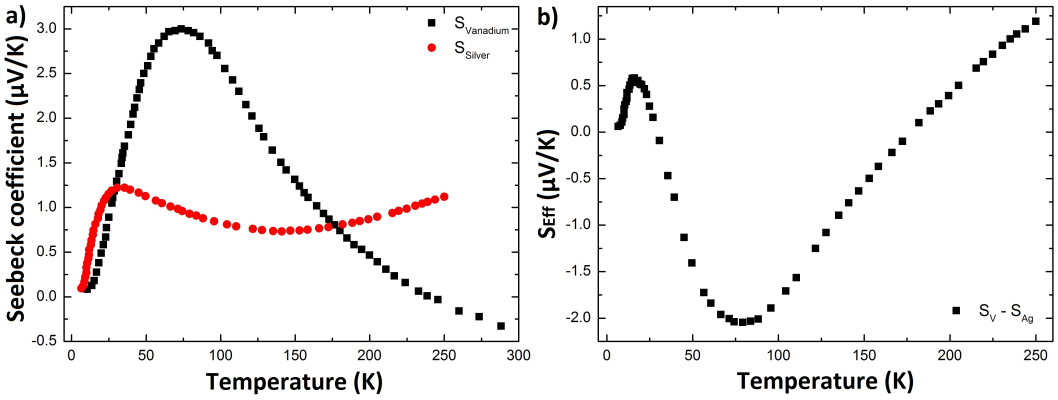

Figure 5.7: *In a) is the temperature response of the Seebeck coefficients for V and Ag. In b) is the effective Seebeck coefficient of the Ag/V system using bulk values. The S_{Ag} and S_V were digitised from [5].*

response of the thermal effects in such a way that voltage picked up can change sign with temperature or even equal zero.

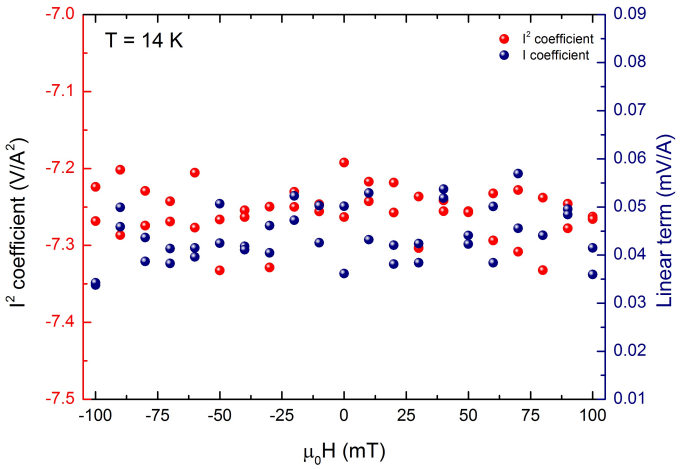

Figure 5.8: *Magnetic field response of both Joule and Peltier coefficients at 14 K. It can be seen the the external field has no effect on the linear and quadratic coefficients.*

Digitising the Seebeck coefficients [5] of the elements and calculating the effective Seebeck coefficient of the detector junction, the temperature dependence response changes from positive to negative, shown in figure 5.7. That means that the sign of the non-local IV after a certain temperature will reverse. Furthermore, in the transition from positive to negative, there is a temperature where the S_{eff} is zero. At that specific

temperature the response of the Joule and Peltier terms should be switched off in the detector.

The non-local IVs present the exact same shape to what was presented in chapter 4. They can be decomposed into a quadratic and a linear term that appears due to Joule and the Peltier effect.

In figure 5.8 is the magnetic field response of both I^2 and I coefficients at 14 K. The range of the field used was the same with what was used for all the transport measurements of chapter 4, for comparison. In the devices measured, there is no field dependence of the coefficients.

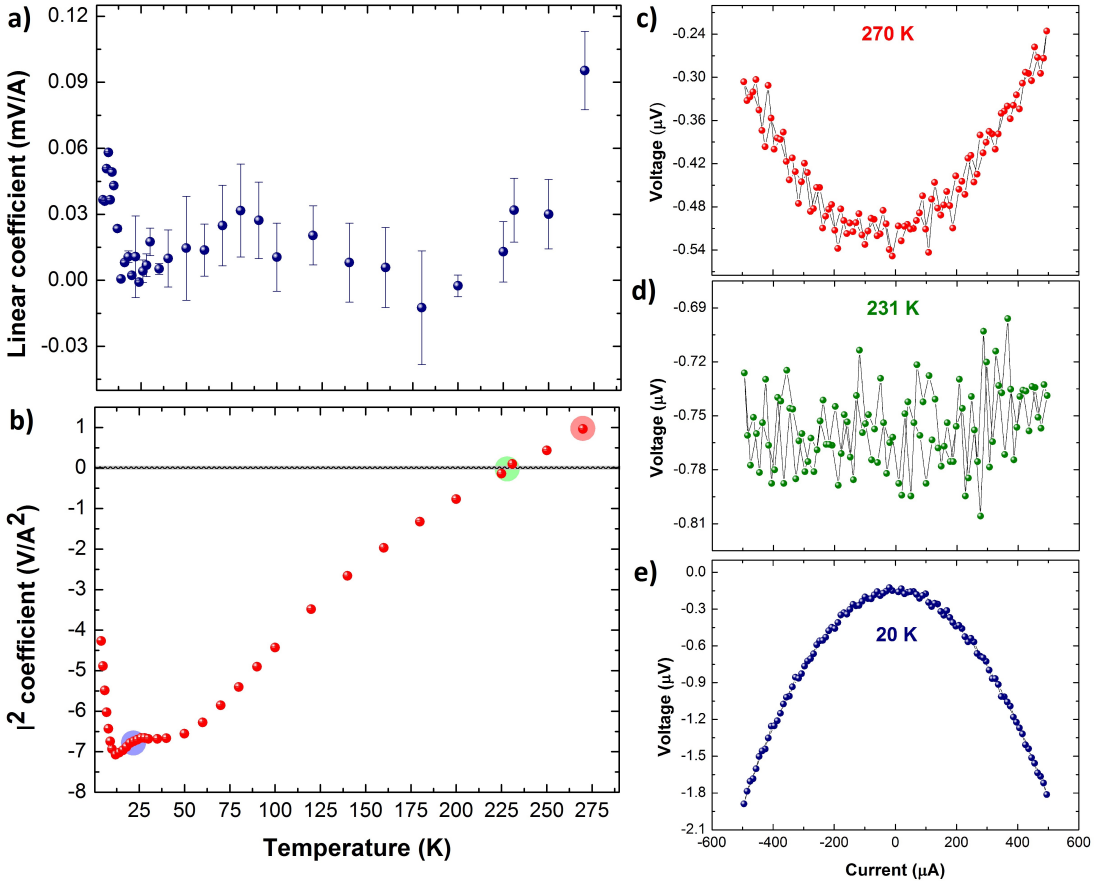

Figure 5.9: *Temperature response of the linear (a) and quadratic (b) coefficient and the corresponding non-local IVs at 270 K (c), 231 K (d) and 20 K (e). The three temperatures were selected in order to present how the detected signal of the thermal effects can be modified using an appropriate combination of materials.*

The temperature response of the coefficients presents interesting features that are summarised in figure 5.9. As it was predicted, the I^2 coefficient had a positive value for temperatures close to room temperature. The sign of the IV in this occasion is positive. While cooling down both components reduce in magnitude and at about 231 K the I^2 and I coefficients are zero. This was observed in the non-local IV response with a signal of a straight line within the noise. That is the exact temperature that the S_{eff} equals zero.

The reason why the detector voltage is not zero at 231 K, can be explained by the c term in the second order polynomial used for the fittings. As it was explained in chapter 4, the c term of the polynomials is an offset in the measurement, probably a heat leak from the nanovoltmeter.

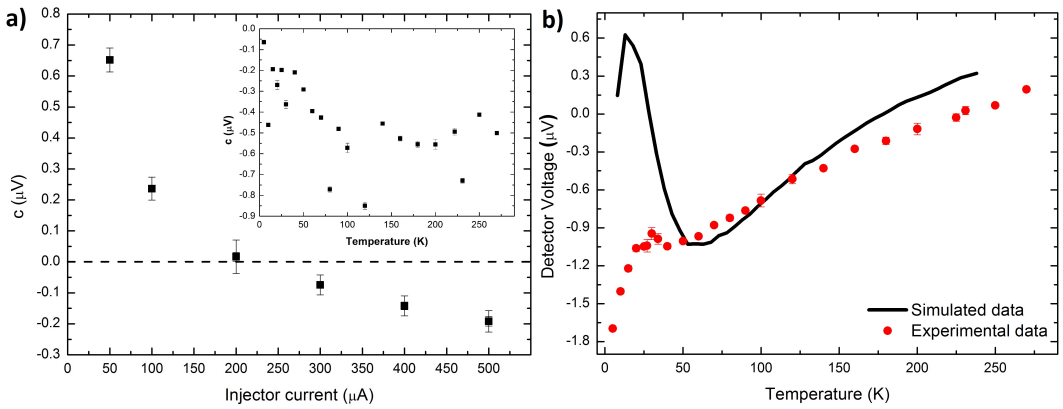

Figure 5.10: *In a) is the change of the constant c as a function of applied charge current. At 200 μA is 0 V, which means that the offset voltage from the nanovoltmeter got cancelled. The inset of figure a), is the temperature response of the c term. Using that and subtracting it from the non-local voltage, the actual detector voltage can be measured as in b), at 400 μA current (in red). In black is the prediction of the voltage from the analytical model. The data are in a good agreement from 250 K down to 50 K. After that they differ, but still preserve the same trend.*

As presented in the inset of figure 5.10, the term c is at about -0.5 μV in the temperature range used for the measurements.

Below that temperature the S_{eff} has a negative value and thus the sign of the non-local IVs in the corresponding temperatures reverses. That means that by increasing the magnitude of the applied charge current (absolute value), the detected voltage increases. As the S_{eff} keeps decreasing with temperature, the absolute value of the

detected voltage increases as well.

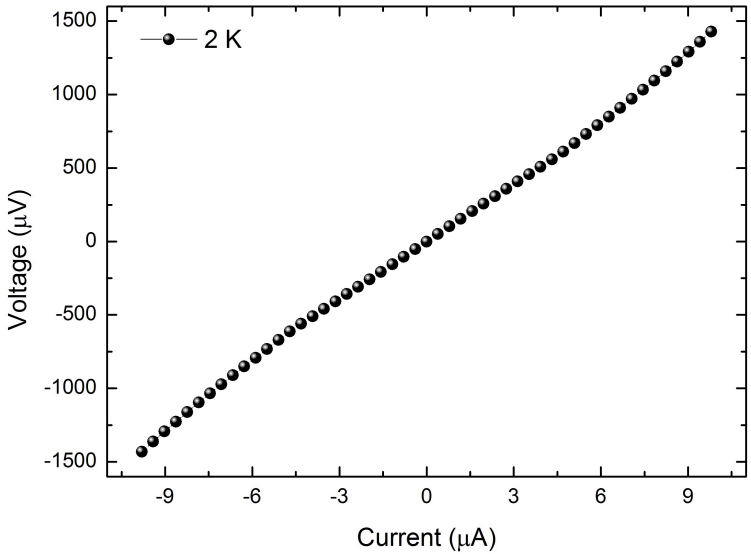

Figure 5.11: *This is the local IV of the injector at 2 K. The IV is not linear but has two deflection points at ± 4 μA, signs that it is partially in the superconducting state. The value of 4 μA is the critical current at 2 K.*

Cooling down the sample to 2 K, the local IV of the injector was not linear any more, but presented features of a combination of an Ohmic and partially superconducting metal. The resistance as a function of temperature measurement of the injector electrode revealed that the circuit starts to enter the superconducting regime at about 3 K, but even down to 2 K the vanadium injector did not fully superconduct. The current used for the measurement was 3 μA, since the local IV of the injector presented Ohmic behaviour above this current.

The non-local IVs, on the other hand could provide interesting information. In figure 5.12 are presented the non-local IVs as a function of the applied charge current, at 2 K. In 5.12 a the non-local IV is essentially bias independent up to about 20 μA and then, depending on the current direction it increases (decreases) for negative current sign (positive). First of all, that means that the V in the detector was superconducting. Increasing the applied charge current in the injector to above 20μA, the quadratic term is large enough to contribute to the detected signal. The peak (dip) of the signal was always at the same current value of 41.78 ± 1.81 μA (-41.78 ± 1.81 μA).

Secondly, the detector voltage at zero current changes as a function of the injector

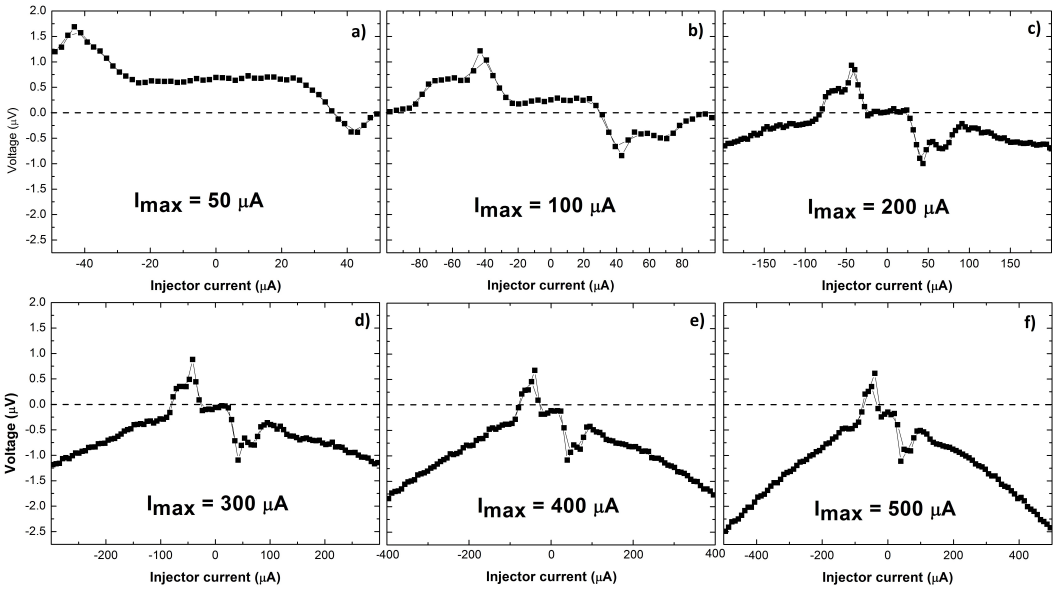

Figure 5.12: *Non-local IV as a function of the applied current at 2 K. The offset at zero bias is changing as a function of the applied current from positive to negative.*

current from positive to negative as shown in figure 5.12. That means that even when the current is at zero Amps, the nanovoltmeter dissipates power in the device. According to 5.10, that is being cancelled out at 200 μA current supplied in the injector. In addition, from the temperature dependence of the term c, the actual detected voltage purely from the thermal effect can be calculated. In figure 5.10 b in red, is the measured voltage for a current of 400 μA. The data in black represent the expected voltage using the analytical model developed at the beginning of the chapter. They are in good agreement from 250 K to about 50 K. After that, although the prediction is not the same with the experimental data, they still present a similar trend.

The non-local IVs at that temperature revealed a regime where the voltage is almost constant as a function of current. After a critical current two voltage peaks presented in either side. Above that temperature the NLIVs had the normal quadratic behaviour. This is a new way of dragging the detector electrode out of the superconducting regime using a combination of Joule heating and Peltier generated in the injector.

The NLIVs are inverted due to the temperature behaviour of the S_{eff} of the system. Furthermore, the spikes in the NLIVs just before the Joule heating term starts to contribute in the voltage are similar to the heat capacity behaviour of a superconductor

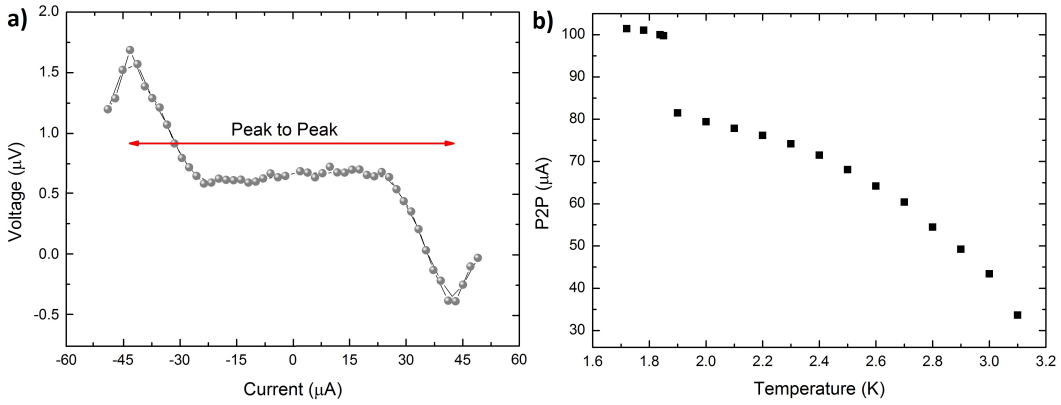

Figure 5.13: *In a) is the non-local IV of the V/Ag detector at 2 K and at 50 μA current amplitude. There are two deflection points right before the quadratic term starts contributing to the IV. The peak to peak distance was measured as a function of temperature, plotted in b).*

[91], [92] that increases in the transitions from a SC to a NM.

A more detailed measurement revealed that the peak to peak distance, measured in μA and summarised in figure 5.13, increases as the temperature decreases. The behaviour is similar to that of the energy gap as a function of the temperature that a BCS superconductor presents. Heating the device in the injector side is probably increasing the temperature of the detector. Just before the transition of the vanadium detector from a superconductor to normal metal, the heat capacity increases presenting a peak, same with the one measured in the NLIVs measurements. The behaviour is still not fully understood.

5.4.1 Detection and analysis of the effects in the Py/Ag/Py NLSVs

From the simpler system of two NM as thermal injector and detector, we moved on to the actual LSVs with FM electrodes to decouple the contribution of the spin and thermal transport.

Once the heat flow reaches the second heterojunction in the Py/Ag/Py, due to the difference in their Seebeck coefficients, this temperature gradient will transform into a voltage difference. This happens using the relation of S_{eff} = -ΔV/ΔT [80], where S is the effective Seebeck coefficient of the junction, ΔV is the electric potential difference and ΔT the temperature difference. As the Seebeck coefficient is not linear in temperature, the potential difference that is transformed from the temperature differ-

ence changes in a non-linear way as a function of the sample temperature. The second junction acts effectively as a thermocouple.

$$V_s = aI^2 + b(B)I + c \tag{5.20}$$

Fitting the measured non-local IVs [73] with (5.20) will result in three terms. The b(B) term is the spin signal. The I^2 coefficient, related to Joule heating in the injector part, is field independent as shown in figure 5.14.

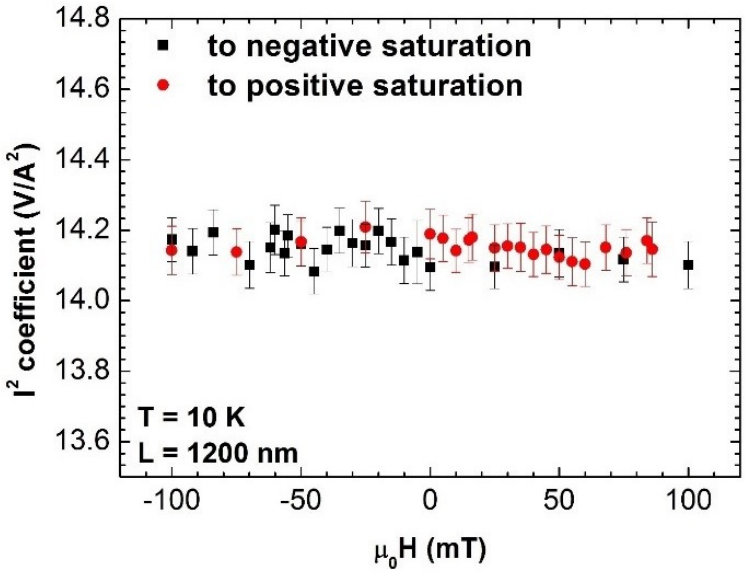

Figure 5.14: *Field dependent measurement of the I^2 coefficient of a device with a ferromagnetic separation of 1200 nm at 10 K. It can clearly be seen that there is no field dependence of the response in this device, and those included in the present study.*

The baseline resistance is defined as the average of the two states (thermal offset) and is related to the Peltier effect. According to the 1D transport equation the non-local voltage detected in the parallel and antiparallel configuration should be equipotential, which means that the signal for the distinguished states should have the same magnitude and opposite sign at different temperatures. What is observed is that there is a background signal that shifts the non-local voltage at higher potentials, shown in figure 5.15. The baseline resistance is presented in a solid red line.

$$BLR = \frac{R_P + R_{AP}}{2} \tag{5.21}$$

The field independent part of the coefficients, on the other hand, has a strong temperature dependency.

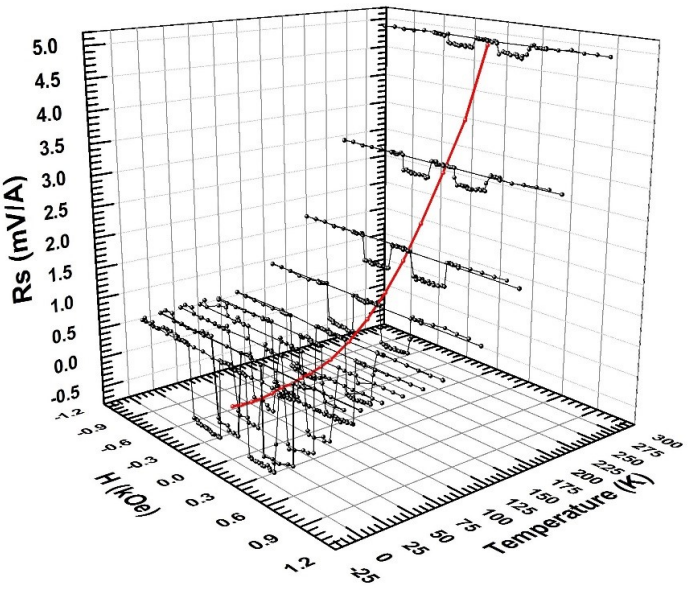

Figure 5.15: *Parallel and antiparallel state of the non-local resistance as a function of field and temperature. The two voltages are not symmetric either side of zero, but there is an offset the shifts the potentials to higher values as the temperature increases.*

5.4.2 Temperature dependent analysis of the coefficients

In the response of the thermal effects, there is an increase in the signal as the sample temperature is rising and as the separation of the ferromagnets is decreasing. The trend, temperature wise, can be separated into two regimes; the high temperature one for T $>$ 100 K and the low one, for T $<$ 100 K.

In the high temperature regime, the signal monotonically increases from 100 K up to 270 K. In the low temperature regime the trend is intriguingly reversed. The signal picked up from the Joule heating increases at low T, as shown in figure 5.16. Given that the resistivity of Py has almost no change below 20 K and that Py has already been suggested as the main Joule heating source, the signal should reach a constant value because the Joule heating term returns a constant value. The reason why this upturn exists, may be related to the thermal conductivity of Ag which increases at low temperatures [93]. This means that although the heat dissipation is the same, the

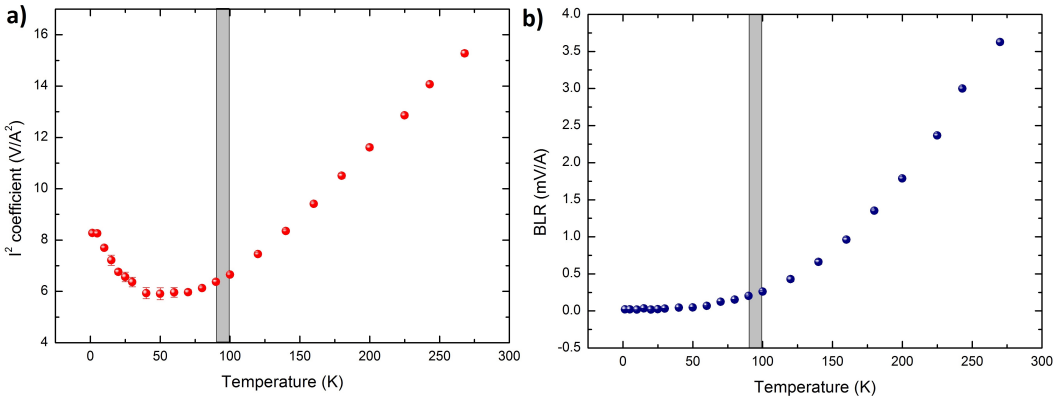

Figure 5.16: *Temperature dependence of the I^2 (a) and I (b) coefficient of a device with a separation of 1400 nm. There are two different trends combined in the response of the quadratic one. An exponential decay one at low temperatures and a linear one at higher ones while for the same temperature range the response of the Peltier term is close to zero and then increases with temperature.*

sensitivity to detect it is increasing and so does the detected signal.

For the BLR, the signal is increasing as a function of temperature for T >100 K (high temperature regime) and is approaching zero for T <100 K (low temperature regime). The heat generation is due to the aforementioned Peltier effect and equals to the product of the temperature T, multiplied by the effective Seebeck coefficient of the junction S_{eff} multiplied by the applied charge current I, $Q_{Peltier}$ = TSI. As said before, in the high temperature regime the signal is increasing as a function of temperature. The reason for that is because the thermopower of Ag and Py at temperatures above 100 K are increasing, in absolute values, as well leading to higher heat dissipation [94]. At lower temperatures the Seebeck coefficients of Py and Ag for the detection are getting close to zero and so although the detection efficiency is increased because of the increase in the thermal conductivity of Ag, the heat generation tends to a constant.

The full set of devices measured, with Py as ferromagnetic injector and detector, bridged with a nominally clean Ag normal metal channel, are summarised in the figure 5.17.

Both thermal components can be broken down into a combination of an exponential and a linear component, as shown in figure 5.18.

In the I^2 coefficient the contribution of the exponential part turns insignificant compared to the linear term close to 100 K but is a lot higher than that of the linear

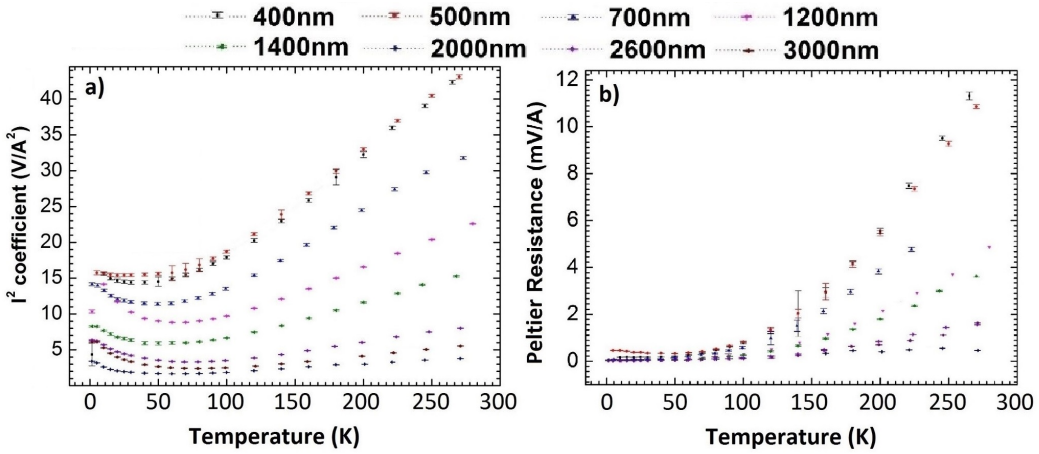

Figure 5.17: *Linear (a) and quadratic (b) field independent terms as a function of temperature for the devices measured. The are two main temperature regimes, below and above 100 K. Above that temperature both coefficients present a proportional to the T response, while below 100 K, the I coefficient signal decreases continuously whereas the I^2 decreases down to a temperature and then the trend reverses.*

term below that temperature. From 100 K upwards, the linear term takes over and since the exponential term is next to nothing, the high temperature behaviour is purely linear. On the Peltier term on the other hand, the exponential term presents a negative decay constant, leading to an increase of the exponential part at high temperatures. The linear term has a small contribution in the signal and at low temperatures up to about 100 K, the value it has is almost the same and opposite to what the exponential term presents so that the sum of these two components is zero.

There are two key temperature ranges/points in the thermal signal as a function of temperature for the two effects. The first one, related to the baseline resistance, has to do with fact that in all separations, a comparison of it with the spin signal leads to the observation that after a certain temperature the baseline resistance signal overcomes that of the spin signal.

As shown in figure 5.19, the crossover of the two signals occurs at a temperature that decreases with the ferromagnetic separation. The interesting thing in this is the fact that the critical temperature changes linearly with the L_{FM}. That result pinpoints the fact that the thermal signal generated from the Peltier effect dies off slower than the spin signal, indicating a higher diffusion length, at least in the high temperature regime.

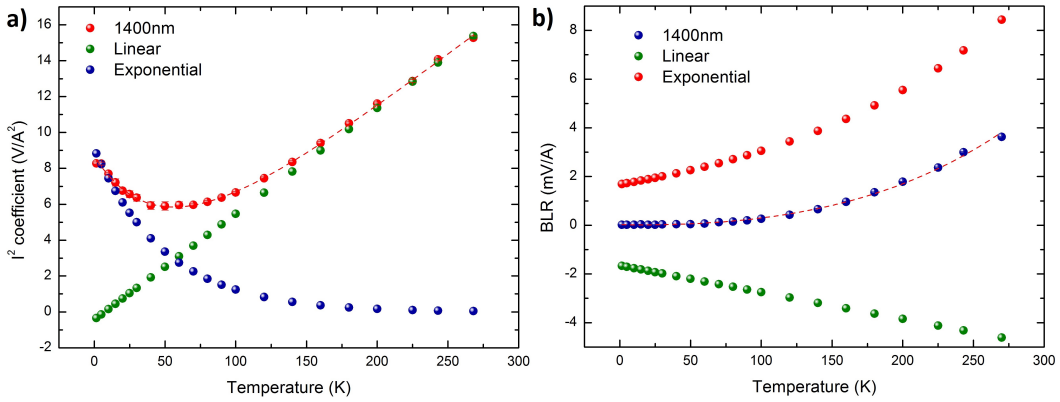

Figure 5.18: *Decomposition of the thermal effects to their individual contributions. Both can be described by a combination of a linear and an exponential term.*

The second key temperature is related to the minimum presented in the I^2 coefficient as a function of temperature. As it has already been shown, there are two distinct temperature regimes. A low temperature one that behaves exponentially-like way and the rise of the signal might be due to the increase of the thermal conductivity, and a high temperature one that behaves linearly and since the thermal conductivity of Ag is constant at this temperature regime, is ruled by the linear increase of the resistivity of Py. The temperature dependence of the thermal conductivity can be found in [93]. The temperature minimum that connects these two regimes changes with the ferromagnetic separation is presented in figure 5.20.

The data of figure 5.20, were normalised to those recorded at the highest temperature measured, 270 K, with the corresponding separations. By normalising them and thus scaling them, it can be observed that at low temperatures, the upturn is more obvious as the separation increases. In figure 5.20, it can be seen that the temperature minimum is in general increasing with separation and moreover in an almost linear way. Only the device of 1200 nm separation is slightly off the general trend (marked in red in figure 5.20). The suggested explanation for this, is based on the fact that the heat flow rate is proportional to the thermal conductivity of a material and inversely proportional to the thickness of it.

$$\frac{\Delta Q}{\Delta t} = KA\frac{\Delta T}{L} \tag{5.22}$$

Where the heat flow rate (ΔQ/Δt), is proportional to the thermal conductivity

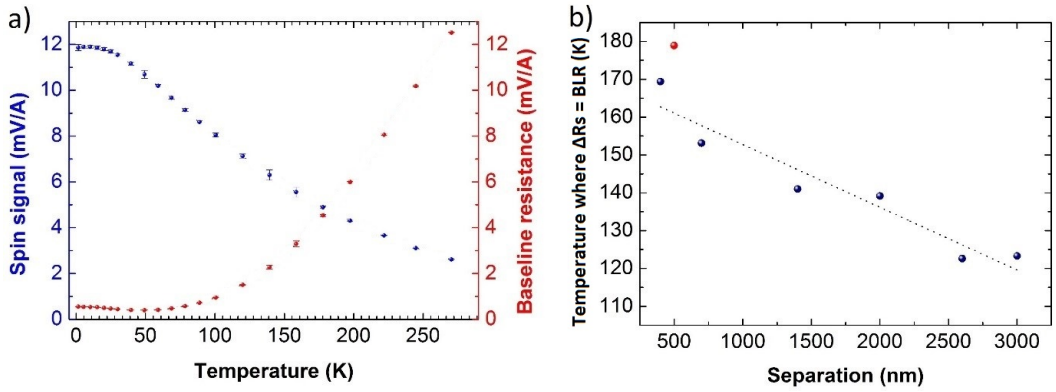

Figure 5.19: *The comparison of the spin signal and the Peltier term as a function of temperature for a device with a separation of 400 nm is in a). There is a temperature where both components are the same. In b) is the temperature where the two signals present the same value.*

(K) of the material (in this case is Ag), times the cross sectional area (A), and the temperature difference (ΔT) over the thickness (L) of the conducting surface. As the system is not in a CPP geometry but spreads laterally, L represents the ferromagnetic separation. Re-arranging the previous equation, it turns to:

$$\Delta T = \frac{\Delta Q}{\Delta t}\frac{L}{KA} \tag{5.23}$$

This can be translated in a way that if the heat flow rate is constant and the cross sectional area does not change the temperature will change in a linear way to the thickness or in this case the ferromagnetic separation, explaining why the minimum is strongly correlated to the L_{FM} and why it increases as we move on to higher distances.

5.4.3 Separation dependent analysis of the coefficients and heat diffusion lengths

Having explained the generation, diffusion and detection of these thermal effects it is a logical step forward to study their diffusion properties using the data as a function of the ferromagnetic separation.

Johnson et al [10] measured the temperature dependence of the non-local resistances and noticed that instead of getting a response of a symmetric signal for the two different states, at higher temperatures, above 100 K, a background signal was added on to the response pushing the non-local voltages to higher potentials (offset) without

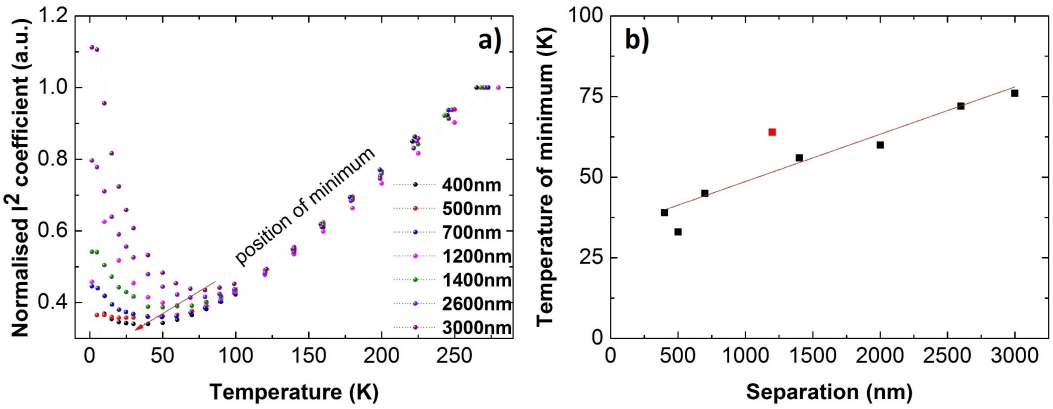

Figure 5.20: *In a) is the normalised I^2 coefficient as a function of temperature for the devices studied. As said before, below 100 K, the signal decreases but then starts to increase again. On b) is the minimum before the linear increase as a function of separation.*

changing the magnitude of the spin signal. He measured an exponential behaviour of the background signal. It was explained three years later by Bakker et [73] al as an additional potential difference due to the Peltier effect in the injector junction.

Plotting the signals using the linear and quadratic coefficients as a function of the ferromagnetic separation, the trend that is observed is a simple exponential decay, shown in figure 5.21. Johnson et al [10] measured a behaviour proportional to $e^{L/W}$, where W is the width of the Ag contact, that is in perfect agreement with our measurements and the theoretical predictions.

The results of the fittings are summarised in figure 5.22, where the Joule heating term has an increasing trend up to 30 K and then plateaus out (within the error) at 1000 nm. The Peltier term follows a similar trend as it's increasing up to around 80 K and its value is around 700 nm up to 270 K. At low temperatures the Peltier term increases rapidly, almost in a linear way from around 100 nm at 10 K to about 700 nm at 80 K. From the linear slope we calculate an increase of the decay length to be 10 nm/K. After that, the trend changes and the decay length stays almost fixed at that value up to 270 K. Finally, the spin diffusion length decreases as a function of temperature through the whole temperature range. It can clearly be seen that above 100 K the device behaviour is dominated by the heat and not the spin diffusion.

Focusing on the Joule heating diffusion length the temperature dependent response presents a trend similar to that of the thermal conductivity response of Ag. For bulk Ag,

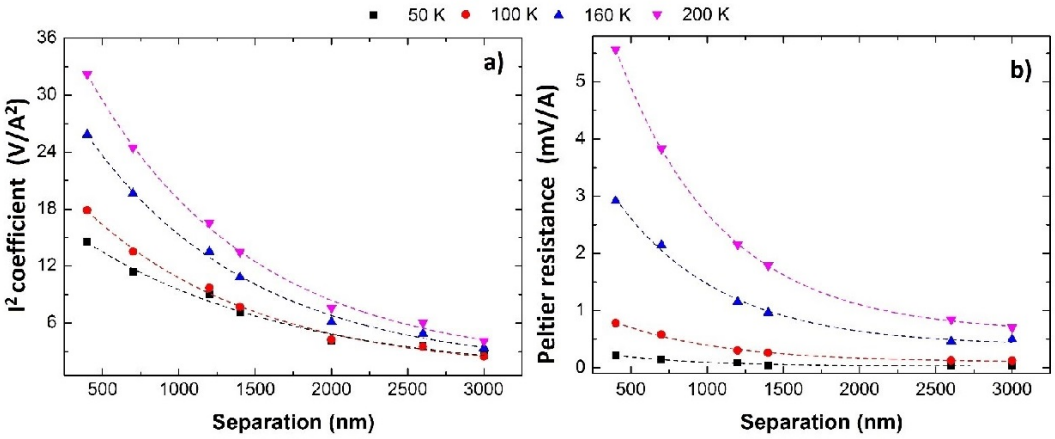

Figure 5.21: *The signal, at selected temperatures, of I^2 in a) and I coefficient in b), as measured using the non-local geometry, as a function of the ferromagnetic separation. Simple exponential decay curves were fitted to the data to obtain their decay length. The observation agrees with Johnson et al [10].*

the thermal conductivity is almost temperature independent, keeping the same value from 300 K down to about 80 K, same as the diffusion length due to Joule heating. Apart from the part that the thermal conductivity plateaus out at above 100 K, as the sample is being cooled down, it increases in a 1/T way (starts below 100 K as shown figure 5.22) until a temperature that peaks and the change is proportional to exp (Θ_D/T) (that is at 40 K for the samples measured, see figure 5.22) followed by a decrease proportional to T^3.

The diffusion length because of the Peltier term presents a similar behaviour to that of the I^2 coefficient at high temperature where its response does not change, within the error, down to 100 K. Below that temperature and although the thermal conductivity of Ag increases, the heat generation decreases. The reason why is because as the $Q_{Peltier}$ = STI, temperature is decreasing and the Seebeck coefficient of both Py and Ag decreases and tends to zero and so does the diffusion length. The interesting part is that at the temperature where the diffusion length of the I^2 coefficient peaks, the one from the Peltier term reaches the constant value of about 100 nm; value that matches the dimensions of the normal metal channel.

Assuming literature values for the Seebeck coefficients for Py and Ag, the temperature drop in the detector junction can be calculated. Using S_{Py} = -20 μV/K and S_{Ag} = 1 μV/K, [83], [77], the effective Seebeck coefficient of the junction can be calculated,

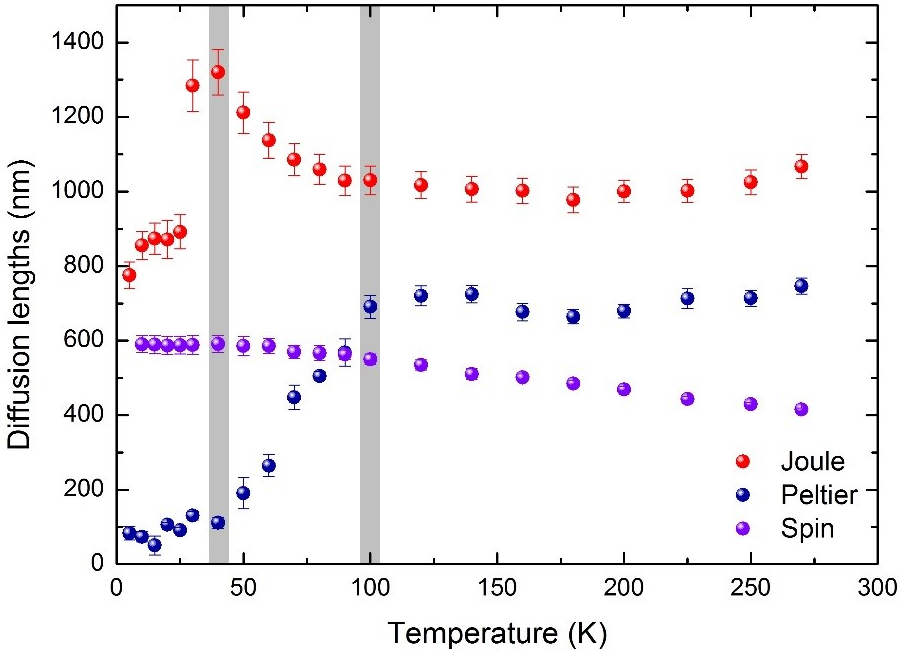

Figure 5.22: *Decay lengths of all the contributions in the non-local transport experiments as a function of temperature.*

simply by following the current (or the spin current in our case) flow.

$$S_{eff} = S_{Ag}\text{-}S_{Py} = 21\mu V/K \tag{5.24}$$

The first part of equation (5.20) is due to Joule heating in the injector junction and can be written as:

$$V_{detector} = aI^2 \tag{5.25}$$

combined with

$$a = \frac{\Delta T}{I^2} S_{eff} \tag{5.26}$$

while for the Peltier term it should be:

$$V_{detector} = bI \tag{5.27}$$

combined with

$$b = \frac{\Delta T}{I} S_{eff} \tag{5.28}$$

one can calculate the temperature rise due to the Joule heating and the Peltier effect in the detector junction combining the above with

$$V_{Seebeck} = \Delta T S_{eff} \tag{5.29}$$

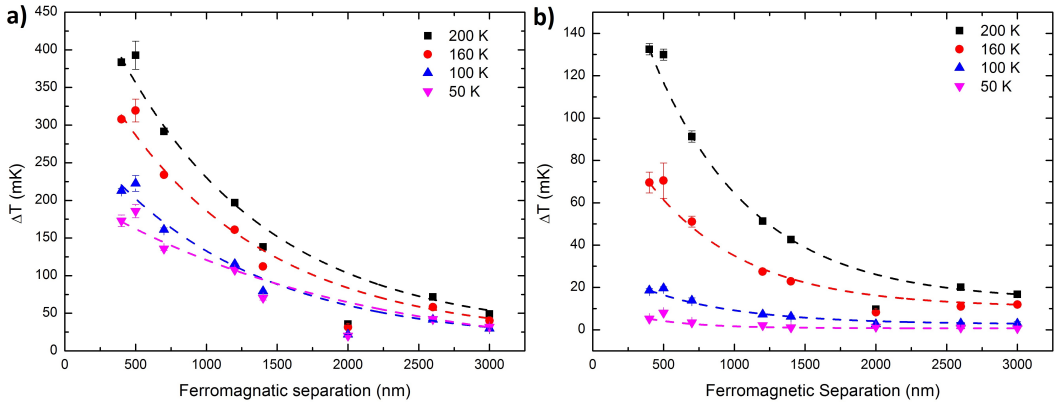

Figure 5.23: *Temperature drop in the detector junction from Ag to Py due to the heat generation because of Joule heating in a) and due to the Peltier effect in b). The temperature drop is given as a function of the ferromagnetic separation at the same four temperatures used for the calculation of the diffusion lengths in figure 5.21. There is a decreasing trend of the ΔÎ¤ as the separation increases.*

It is observed a decreasing trend in the ΔT response as the separation of the ferromagnetic electrodes increases, at all temperatures. In figure 5.23 an exponential decay is fitted as a guide for the eye (dashed lines). From the calculations can be found that a 1200 nm L_{FM} should produce a ΔV of about 6 μV that corresponds to a ΔT of 286 mK at 300 K. To get the voltage drop that would exist in the detector due to Joule heating, the I^2 coefficient as a function of temperature data were linearly extrapolated. On the other hand, from the calculations was found that a 1200 nm L_{FM} should produce a ΔV of about 2.89 μV that corresponds to a ΔT of 138 mK at 300 K for the heat generation due to the Peltier effect in the injector junction.

The value of the ΔT that is predicted is almost 90% bigger than what was measured using the SThM which was about 150 mK and about 40% bigger compared to the 90 mK for the Joule heating and the Peltier term respectively. Given that the current

magnitude used for the SThM was 3 times bigger than what used for the non-local measurements in the cryostat, one would expect that the ΔTs measured should be bigger than those calculated using the transport data. The samples were covered with a 500 nm MMA resist layer (as discussed in methods, chapter 3) that was stripped just before the measurement, but they could have been already oxidised before that. There are two different possible explanations on why there is such a difference.

First of all, the Seebeck coefficients could change since we are not using bulk materials but nanowires [95, 96] and thus that would change the outcome of the calculations. Secondly, the SThM technique is a surface imaging technique, which means that what we get from the scans is the temperature of the surface of the detector junction. This result may differ from what was calculated from the transport measurements, since the thickness of the junction is 1250 Å and may present a temperature gradient within the bar. Finally, in the case that an oxide layer exists on the junction surface, it will have a different thermal response to the bulk of the junction.

5.5 Current dependent non-local IVs analysis

5.5.1 Introduction

Since the Peltier effect is present in the measurements, it means that the BLR should get affected from the current direction. The questions that arises here are: is this experimentally observable and is it going to affect the spin transport? As a first stage to further explore the current dependence of the spin signal and the thermal components that it is accompanied with, the measured non-local IVs were fitted in the full field and temperature range in two more different current regimes for $500 \leq I \leq 0$ A (positive counterpart I_+) where the current is going from the FM to the NM and for $0 \leq I \leq$ -500 (negative counterpart I_-) where the current is going from the NM to the FM.

In figure 5.24, there is a comparison between the data obtained using this method and the fittings of the full IV curves. The IVs presented are from one of the nominally clean samples used in the previous chapters that was fabricated with a 400 nm and measured at 15 K. The full IV fittings have a very good goodness of fit value supported by the very small amount of residuals in both states. The same analysis completed in the fit depending on the current sign and the residuals were of the same order of magnitude to those obtained from the full IV fittings. The local IV of the injector was

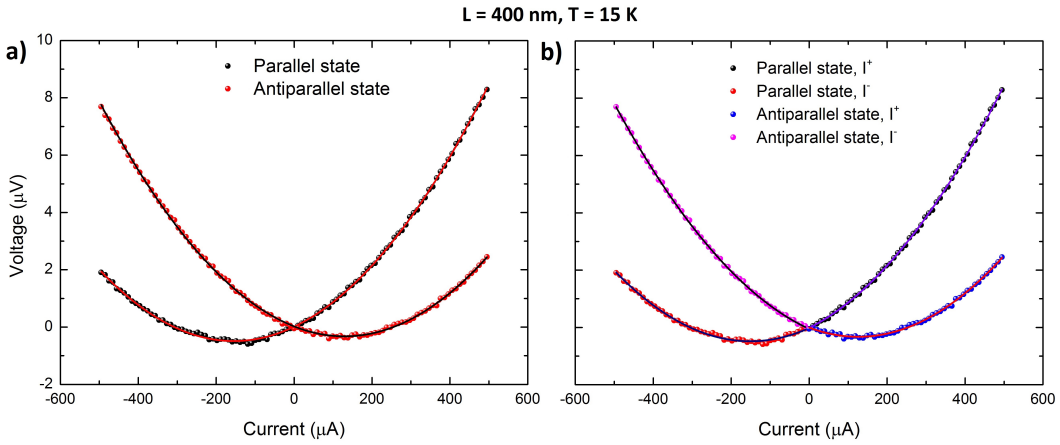

Figure 5.24: *Non-local IVs for the parallel and antiparallel states of device with a 400 nm ferromagnetic separation at 15 K with the two ways of analysis. The IVs were fitted based not only on the relative ferromagnetic orientation (a) but on the current sign as well (b).*

checked at base temperature (2 K) to make sure that it still behaved in an ohmic way.

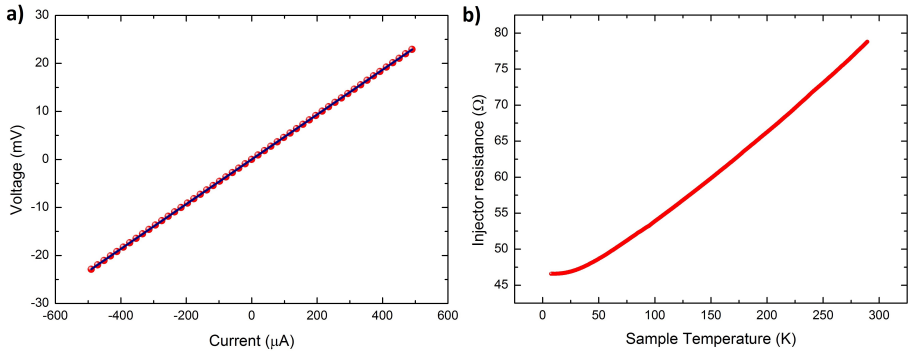

Figure 5.25: *Local IV characteristic of the injector circuit at 2 K in a)and its corresponding resistance as a function of temperature for the range used in the measurements as well in b).*

The sample used for the local resistance had a centre to centre separation of 350 nm and is presented in figure 5.25. Local IVs were measured and confirmed a linear dependency of the voltage to the current as expected for ohmic behaviour of a material. The experimental data are in red and the linear fitting is the solid blue line. The slope of the IVs returns a resistance of 46.64 Ω at 2 K. Furthermore, the local resistance of the injector circuit was measured as a function of temperature making sure that it would cover the range from 2 K up to 270 K, range of temperatures used for the non-local

measurements, and was from about 46 Ω to about 80 Ω.

5.5.2 Linear and quadratic terms

By fitting the full IVs as well as the parts of the IVs for the positive and negative current the linear and quadratic components obtained can be compared.

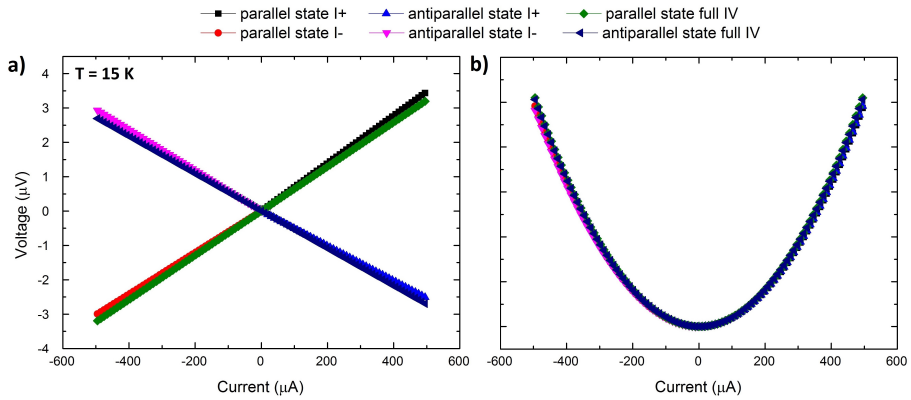

Figure 5.26: *Linear (a) and quadratic coefficients (b) of the same device with the 400 nm separation at 15 K. The deviation of the individual branches from the main one is clear in both terms.*

For a specific temperature the non-local IV data were fitted and the coefficients were extracted both for the linear and the quadratic term. In the linear component, the coefficients extracted by fitting the full IV are in green for the parallel state and dark blue for the antiparallel state, as shown in figure 5.26.

Interestingly, fitting the two states for the two different current regimes the output varies and deviates from what was calculated fitting the full IV. Four more linear coefficients presented, in black and light blue for I_+ and parallel and antiparallel state respectively, and in red and pink for I_- and parallel and antiparallel state respectively. Given that the linear and the quadratic components are related through the second order polynomial equation, that means that a change in the linear coefficient will lead to a change in the quadratic coefficient as well. Indeed, the I^2 coefficients differ to that obtained by fitting the full IV but not for the different current directions. The temperature dependence of the phenomenon for both components was measured as well in order to find out if the splitting is a feature the devices present only at low temperatures or if it persists up to room temperature as well.

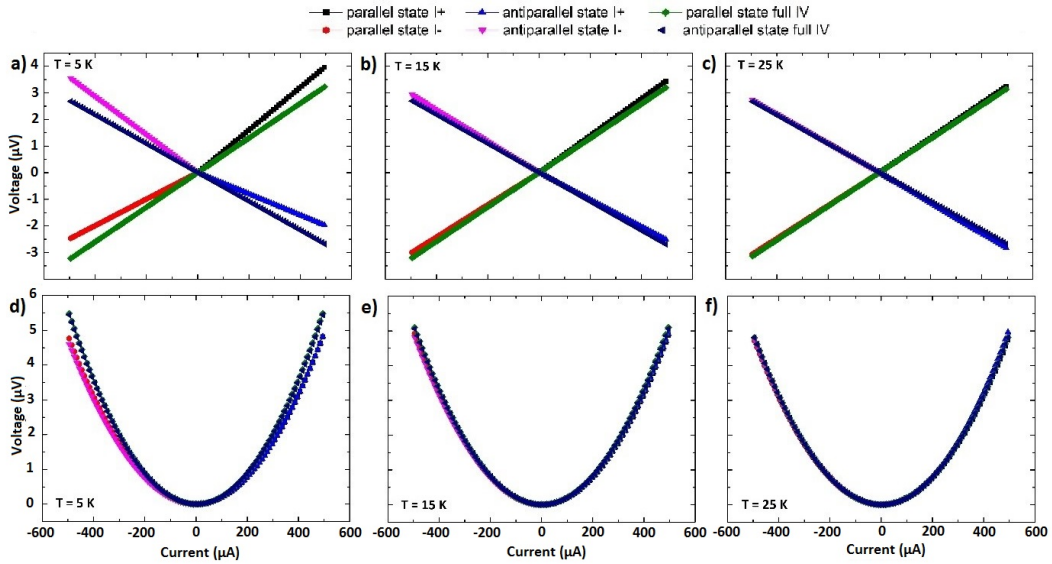

Figure 5.27: *Splitting of the linear (a, b, c) and quadratic (d, e, f) components from 5 K to 25 K. There is a obvious temperature dependence of the effect, where it gets suppressed as the temperature increases.*

The linear and quadratic components shown in figure 5.27 are for three different temperatures. Focusing on the linear part of the IVs, the gradient of the component for the parallel (black and red) and antiparallel state (magenta and blue) for both current regimes at low temperatures diverge from that obtained by fitting the full IV(dark green for the parallel state and dark blue for the antiparallel state). As the temperature increases the difference in the gradient is getting smaller and at about 30 K it seems that all the different curves collapse in a universal one that matches the one obtained from fitting the full current regime. The quadratic component exhibits a similar behaviour by diverging from the trend of the component of the full IV. Analogous to the linear component, all different curves for the quadratic component seem to collapse into one at 30 K, and will be shown in 5.33 later on . The reason why the quadratic term changes lies in the fact that the linear term is changing leading to the change in the quadratic term, being coupled through the second order polynomial used for the fittings. The only difference here is that there are two different curves that only depend on the current regime and not in the relative orientation of the ferromagnetic electrodes, as it has already mentioned that the quadratic component is field independent.

Simply by changing the current direction there is a clear change in the response

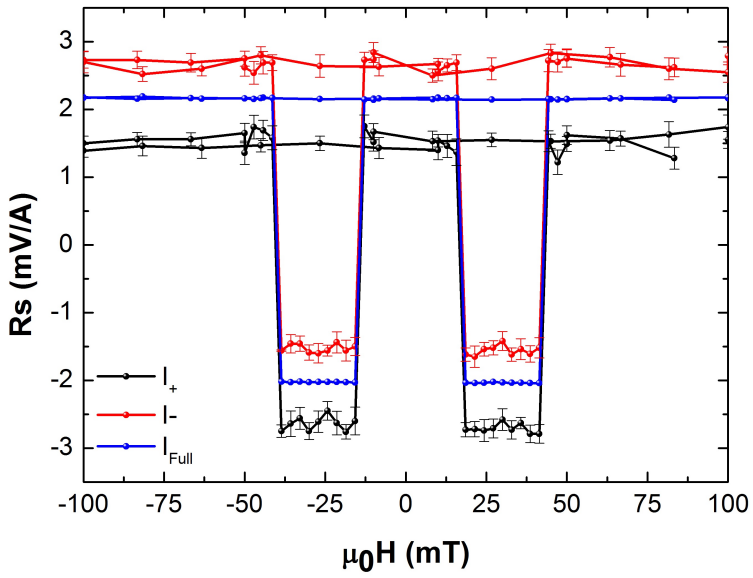

Figure 5.28: *Change in the response of the non-local resistance as a function of field at 5 K for positive and negative current direction. The change of the Rs between these and the* $Rs_{I\ full}$ *is quite large. The data for* I_+ *and* I_- *were produced by fitting the corresponding parts of the NLIVs.*

of the R_s as a function of external magnetic field, illustrated in figure 5.28. As it will be shown later in this chapter, the spin signal is the same within the error and what differs is the offset, related to the baseline resistance. By changing the gradient of the linear component and the curvature of the quadratic component, one would expect a modification of the baseline resistance and I^2 coefficient as a function of temperature depending on the sign of the current.

Before exploring these questions, it is vital to confirm that this behaviour is not a result of an artefact.

5.5.3 Confirmation of the splitting.

Before we move on the temperature dependence of the different coefficients, to confirm that the change is real and not faulty fittings, the non-local measurements were repeated in a different way to decrease the incoming error, by improving the statistics. In all the measurements so far, one non-local IV per field point would be recorded. The number of repetitions was increased to be between 10 and 15.

Furthermore instead of fitting the same IV data and fitting the I_f, I_+ and I_- of the

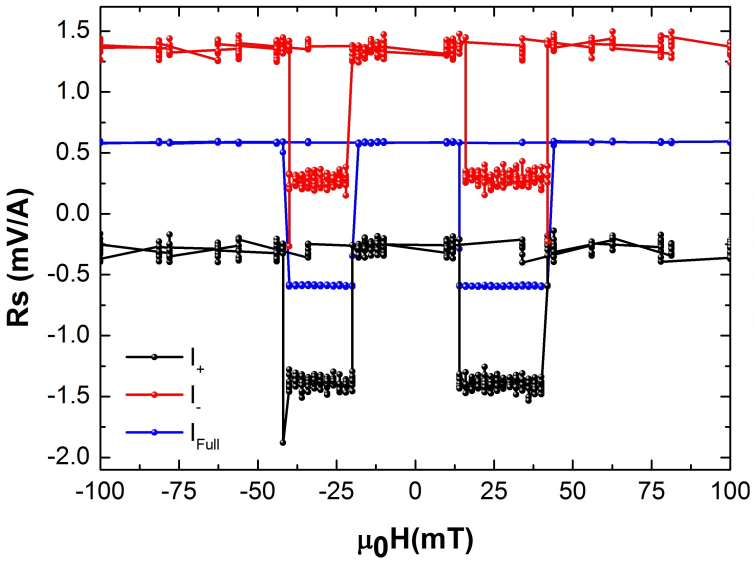

Figure 5.29: *The splitting in non-local resistance depending on the current sign is confirmed, as the data for I_+ and I_- were produced by recording NLIVs in the corresponding current directions. The measurement was performed at 5 K, with a temperature stability of about 4 mK.*

IVs, the measurement at the same temperature was repeated from -500 μA to 500 μA, 0 μA to 500 μA and -500 μA to 0 μA. The non-local resistance as a function of field at 5 K with the increased number of repetitions is presented in figure 5.29.

There is indeed a splitting in the non-local resistance measurement as a function of field in the parallel and antiparallel state depending on the current direction. Furthermore, the splitting in the signal should also be observed in the baseline resistance as by definition it is the average of the parallel and antiparallel state [73], [83].

5.5.4 Field sign dependency

The next step after checking the current sign dependency is to see if there is a dependence of the phenomenon on the external field direction. Since there are eight different combinations of how the spins should be aligned.

As shown in figure 5.30, depending on which direction the current is flowing (from the ferromagnet to the normal metal or the opposite) and if the device is in the parallel (both injector and detector are aligned to the external magnetic field pointing upwards or downwards) or antiparallel state (only the injector or the detector is aligned to the

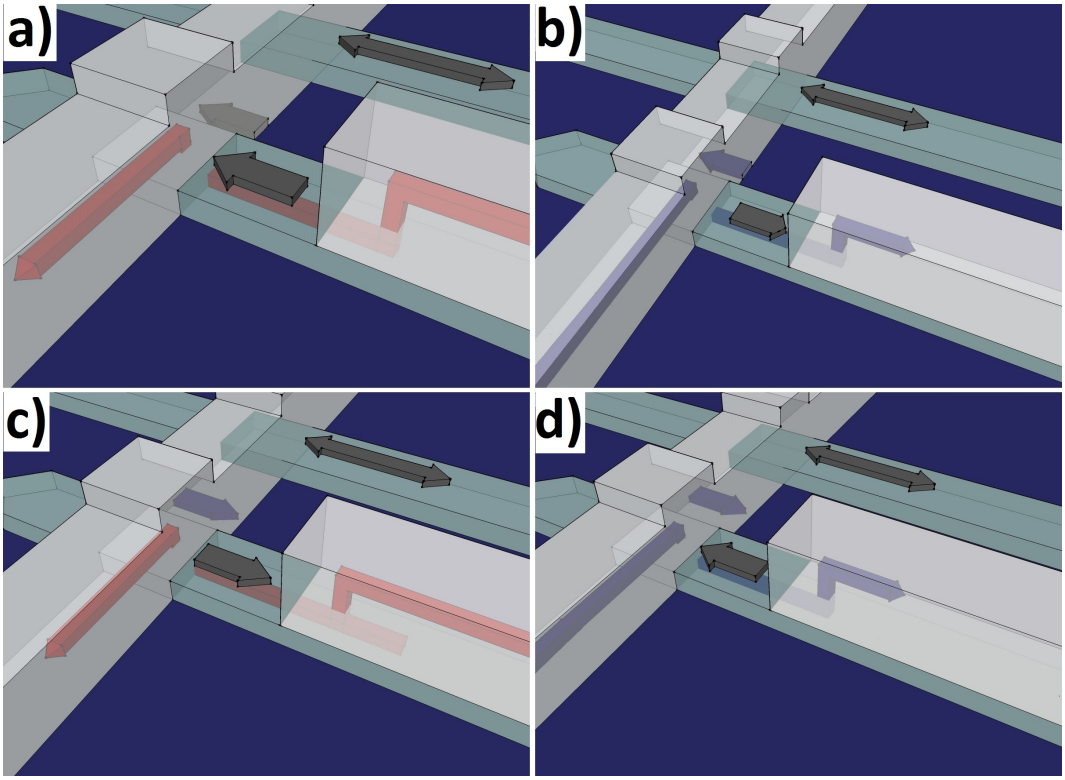

Figure 5.30: *There are eight different cases depending on the current direction and the relative magnetisation orientation.*

external magnetic field), there are eight different cases rising plus one more, in the absence of magnetic field. The sample used for this test was a Py/Ag/Py lateral spin valve, with the difference that a thin layer of Fe (0.5 Å) was deposited at the SiO_2/Ag interface for experiments that will be analysed in chapter 6.

What was observed and depicted in figure 5.31 was that the non-local resistances group independent to the field direction and they depend only on the current direction.

5.6 Temperature dependence of the non-local resistance, non-local signal and baseline resistance

Figure 5.32 is the plot of the non-local resistance for the parallel and antiparallel state as a function of temperature for a sample with 400 nm separation. The positive and negative current sign fitting analysis was applied and the baseline resistance along with

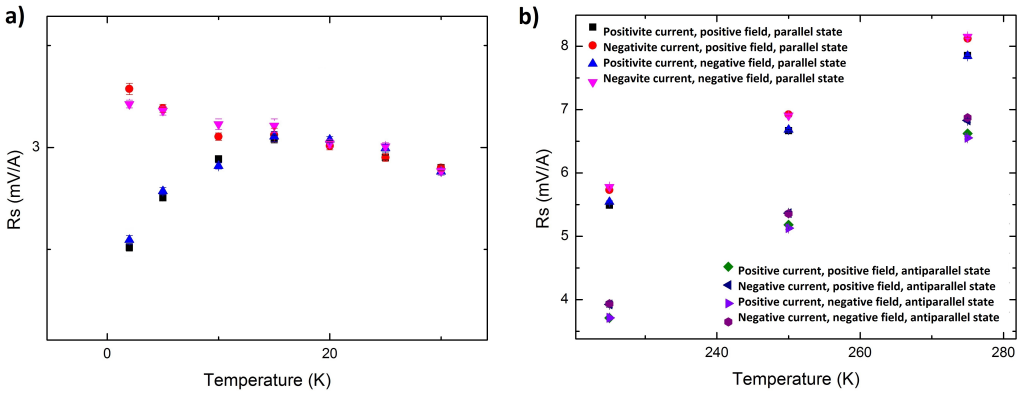

Figure 5.31: *An 800 nm separation device where the different combination of field and current orientations were measured. In a) are the low temperature data and in b)the high temperature data. It can be seen that the direction of the magnetic field has no effect to the splitting as the data both in (a) and (b) group depending only on the current direction.*

the spin signal for the three different regimes was calculated.

The change in the baseline resistance for I± is small at high temperatures, but non-zero. Its magnitude though, becomes larger when T > 30 K. This anomalous behaviour of the BLR leads to a similar splitting in the $R_{s\ P}$ and $R_{s\ AP}$. As the change in the Rs_P and Rs_{AP}, with respect to the current sign, is the same, the ΔR_s presents no alteration in its temperature response. In the non-local resistance as a function of temperature data it can be seen that at temperatures higher than 30 K, independent to the relative magnetisation orientation of the FMs, there is a small difference for the two current signs, as shown in the difference of the signals. The change is the same within the error. Given that the ΔR_s by definition it is the difference of the non-local resistance between the states that means that it not should be affected by the current sign, confirmed in figure 5.32. For precision, the change in the spin signal for the two current signs is around zero leading to the conclusion that the effect is not spin-dependent.

Moreover, the baseline resistance should present a splitting, since by definition is the average of the non-local resistance signals. The calculated difference in the baseline resistance has the same trend with that of the non-local resistances. To check that by analysing the data fitting the full IV and the two parts of it should make any difference in the output, the data were averaged for the non-local resistance, ΔR_s and BLR for I+ and I- and were compared with the full range. The results are in a great agreement supporting that the analysis technique does not introduce artefacts.

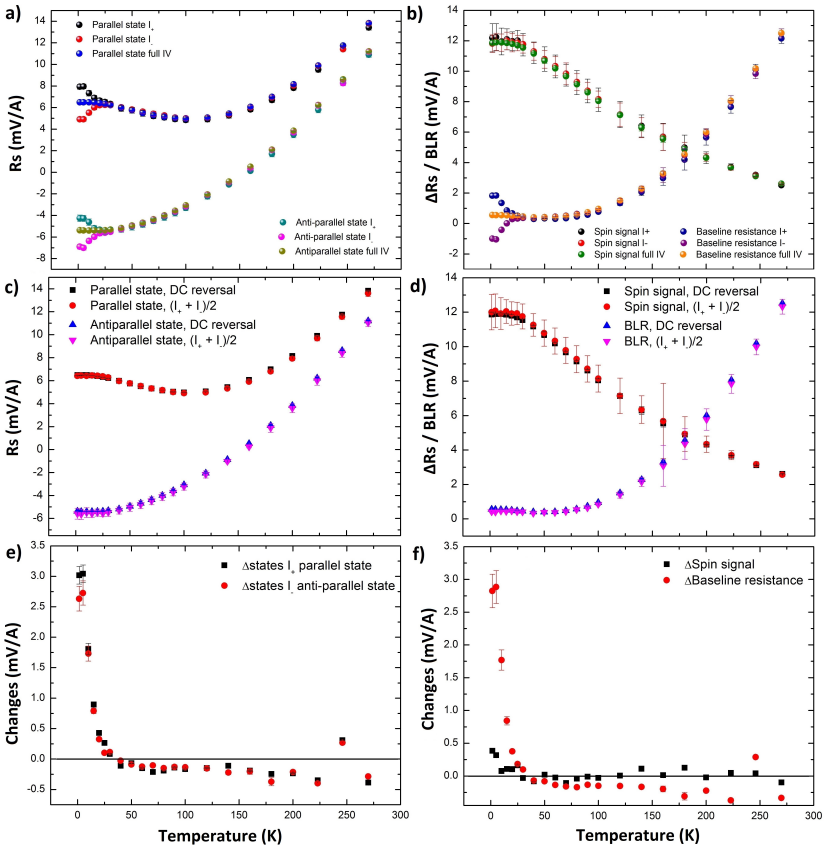

Figure 5.32: *In a) is the non-local resistance as a function of temperature and in e) is the difference of the signal in the two current signs for the two states. In b) is the calculated spin signal and baseline resistance from a), along with the difference of the outcome for the different current sign in f). Comparison of the R_s, ΔR_s and BLR both for the I_{full} and the average of the branches for the I± is in c) and d) respectively.*

The I^2 coefficient as a function of temperature is depicted in figure 5.33. The response of this thermal component is pretty much the same as it would be by fitting the full IV range down to about 30 K. From that temperature downwards, the response changes dramatically. This is not unexpected since, as said before, the linear and quadratic components are related through the second order polynomial. Since the change in the linear term increases below that temperature, so does the I^2 coefficient. Interestingly, the shape of the I^2 coefficient trend is following that of the temperature dependence of the Seebeck coefficient of Ag. In the bulk it presents a dip in the signal at about 120 K (instead of the 50 K in the 500 nm separation sample) and then peaks

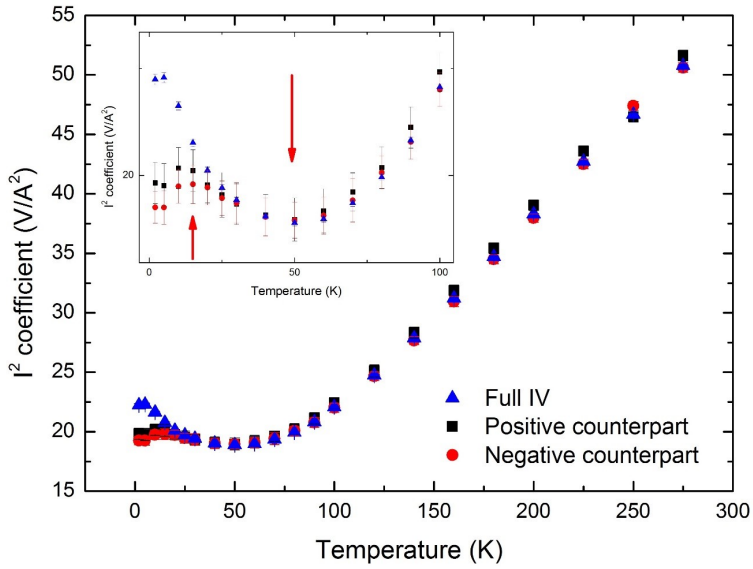

Figure 5.33: *The I^2 coefficient as a function of temperature, where its response deviated from the main one below 30 K.*

at about 30 K (instead of the 15 K for the device).

Given that the injector is at a higher temperature than the rest of the circuit, phonons are accumulated at the injector junction and diffusing down to the detector junction giving enough energy to more electrons to move down the normal metal channel.

5.6.1 Material combination and temperature dependence of the effect.

Another test to solidify the response of the splitting effect is to test the evolution of the spin signal and baseline resistance at different temperatures for different FM/NM combinations. The systems that were tested were $Co_{70}Fe_{30}$/Cu/$Co_{70}Fe_{30}$ (top row), Py/Ag(Fe)/Py (middle) and Py/Cu/Py (bottom row) apart from the Py/Ag/Py. The Ag(Fe) system is a Ag channel doped with a 0.5 Å of Fe in a horizontal position and will properly analysed in chapter 6.

Figure 5.34 is the temperature dependence of the ΔRs and BLR signal of the 3 different systems on the left column. The right hand side column is the difference between the signals for I_+ and I_-. The three different systems present some common characteristics with what has been presented for the clean Ag channel in the Py/Ag /Py LSV of figure 5.32. First of all, the spin signal is the same within the error for the

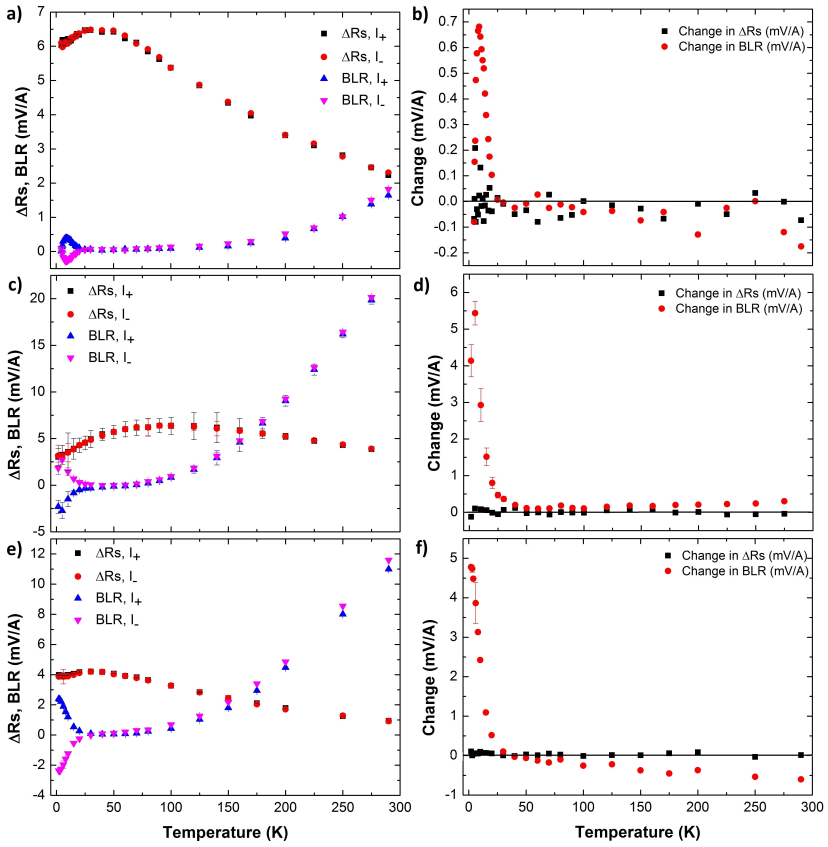

Figure 5.34: *Spin signal and baseline resistance as a function of temperature for 3 different FM/NM combinations in a) ($Co_{70}Fe_{30}$/Cu), c) (Py/Ag(Fe)), e) (Py/Cu) and the difference between the I± for the corresponding effects in b), d) and e).*

two different current directions. It is easier to be seen in the right hand side column where the ΔRs I_+ and I_- change is level to zero.

The BLR change on the other hand presents a completely different behaviour. The splitting for I_+ and I_- is apparent even at temperatures close to 300 K. The difference for the two current directions is getting smaller and gets its minimum absolute value at about 30 to 40 K. Below that temperature the difference is increasing and close to 3 K the trend starts to reverse.

The splitting in the BLR depends strongly on the combination of materials used. This was not unexpected since the effective Seebeck coefficient of the different detector junctions depends on the actual materials. Furthermore, the Peltier effect is linear to the Seebeck coefficient and hence the change in BLR magnitude dependence on the

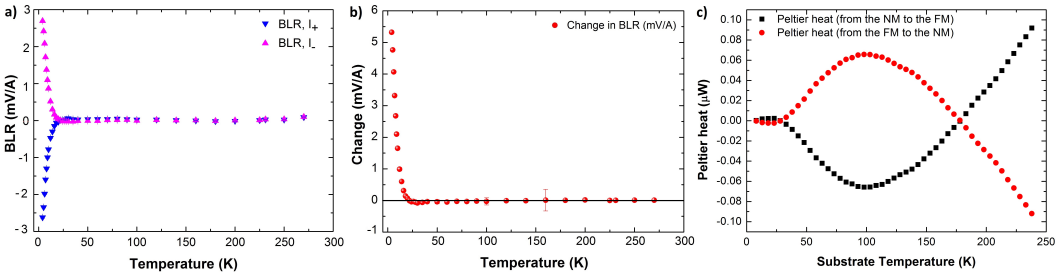

Figure 5.35: *In a) is the splitting in the blr of a V/Ag device. The splitting seems to start increasing again at about 20-30 K. Same temperature with the rest of the devices. In b) is the difference between the blr branches for I_+ and I_-. In c) is the heat produced by the Peltier effect depending on the direction of the current.*

materials system.

Moreover, the change for each of the systems is almost separation independent for L_{FM} up to 2600 nm.

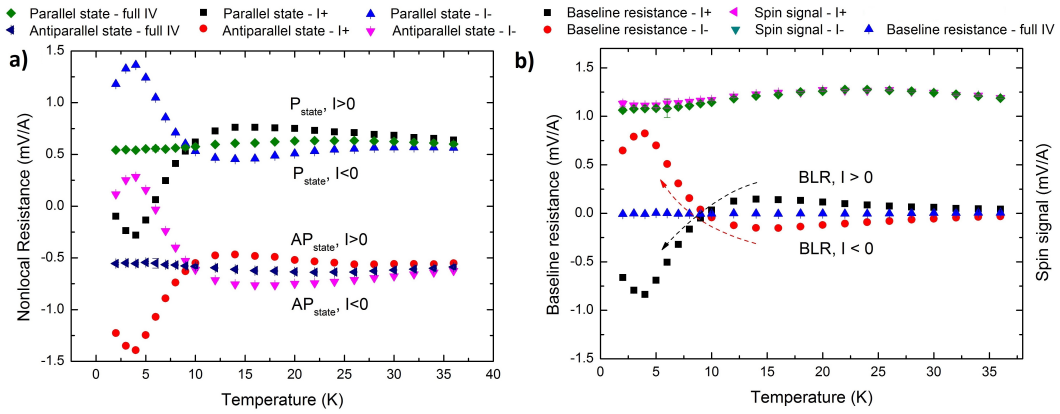

Figure 5.36: *In a) is the non-local resistance as a function of temperature for a device with a L_{FM} of 2400 nm. In b) is the spin signal and baseline resistance calculated from the non-local resistances of the device.*

Below 10 K, in some case it was observed that the non-local resistance independent to the state the system is, interchanges the positive and negative current sign response, mainly in higher separations. As shown in figure 5.36, the response of the non-local resistance changes drastically as it splits and crosses over below 10 K at 2400 nm. Since the baseline resistance is the average of the two states, it follows exactly the same trend for the two different separations. The spin signal on the other hand does not present

any new features with the increased temperature density points.

Some interesting features derive from the V/Ag devices, shown in figure 5.35. First of all, the common feature irrespective to the combinations of materials, is that the splitting acquires significant magnitude below 30 K. The Peltier heat (figure 5.35 c) clearly predicts the crossover of the two branches at about 30 K. As the temperature keeps decreasing, the heating presents a maximum/minimum at about 20 K and then the two branches start to get closer. A similar behaviour to that is observed in figures 5.32 a 5.34 a 5.36 c. The reason why this is not observable to all the devices, may be due to the fact that temperature was not low enough to observe this response.

5.7 Conclusions

The physical characteristics of the metals used are what rule the thermal response of the lateral spin valves in the current study. The fact that charge current is needed in order to give rise to the pure spin currents, is responsible for the generation of the thermal effect presented in the system. The latter, combined with the fact that the injector and detector junctions are bimetallic gives rise to Joule heating and the Peltier effect. The heat they produce, diffuse along the normal metal bar along with the pure spin current. The fact that the thermal conductivity of Ag at all temperatures used to measure the samples, is higher than that of the SiO_2 substrate allowed the biggest part of the heat to flow along the metallic part of the device and not dissipated through the substrate.

The voltage drop due to temperature difference between the silver and permalloy is picked up due to the Seebeck effect. The voltage drop decreases in an exponential way as a function of the ferromagnetic separation as already suggested from Johnson and Silsbee in 2007, depending on the cross sectional area of the junction. A simple exponential decay fitting of the data revealed that above 100 K, the device's behaviour is strongly affected by the contribution of the thermal effects. Below that temperature, the I^2 coefficient term diffusion length increases to about 50 K and drops down as the temperature decreases to 2 K. On the other hand, the Peltier diffusion length drops in a linear way to about 50 K. From that temperature downwards the diffusion length is about 100 nm to 150 nm suspiciously close to the device width and thickness.

The Scanning Thermal Microscopy was employed to map the temperature distribution of the individual thermal components as by locking in the first and second

harmonics of the current we could observe the heating because of the Joule effect and the temperature dipole created in the injector junction because of the bipolar behaviour of the Peltier effect, depending on the current sign. The temperature drops in the injector and detector junctions were measured and the heat dissipation mapping was performed experimentally for the first time on lateral spin valves.

Using the voltage drops due to the thermal effects picked up from the transport measurements presented in chapter 4, we managed to calculate the expected temperature drops across the detector junction. Unfortunately the calculated values did not match those measured experimentally using the SThM, indicating that either the bulk values of the Seebeck coefficients used for the calculations are out by a factor of two for our nanowires or that as the SThM is a surface technique indicated that there is a temperature gradient along the normal metal channel normal to the device's substrate.

In the current dependent analysis of the IVs, it was expected that the output due to Joule heating should be independent of the current sign since the heat dissipation is proportional to I^2R. On the other hand, the Peltier effect is linear to the current and so the direction should make a difference.

What was found is that the non-local resistances were affected as well. No matter if the system was in the parallel or antiparallel state, from 270 K down to 2 K, the non-local resistances separated from the main branch. The splitting seems to happen at the same temperature of 30 K, independent to the material combination. To our surprise, by increasing the density of temperature points for the measurements taken, the two branches not only completely split, but presented features as well. The response would increase and decrease in a non-periodical way and the two branches would cross as well. The magnitude of the effect is field independent, was found to have a very small correlation to the FM separation, if any, and strongly depends on the FM and NM combination

The above lead to the conclusion that the cause of the splitting in the baseline and non-local resistance is thermal and not spin dependent.

A possible explanation could be hidden in the increase of the thermal conductivity of Ag at low temperatures. The reason why the effect is being maximised in that range, could probably be due to the fact that the heat transfer is more effective at low temperatures. Moreover, the bulk thermal conductivity, is maximised at about 4 K and then decreases as the temperature keeps dropping, a feature that could justify the

decrease of the baseline resistance of the long channels below 5 K.

Overall it is a new effect that has never been observed or studied at all in the literature.

Chapter 6

Pure spin currents and delta layers

Over the past few years, extensive research has been done on the unexpected decrease of the spin signal at low temperatures. This has been shown to be the result of Kondo scattering from magnetic impurities in the normal metal (NM) channel of a lateral spin valve. Studies have mostly focused on the origin of these and suggested that they either pre-exist in the source material or get incorporated in the NM channel during its deposition. There remain interesting details in the nature of the scattering that have yet to be understood. A prediction was made some years ago [97] that the spin Hall angle (SHA) could be enhanced by choosing the position at which impurities were embedded in a sample. Here we explored this idea by varying the position of impurities and their effect on the spin-dependent scattering in the transport of a pure spin current.

6.1 Introduction

When impurities are introduced in a NM they can modify the behaviour of a pure spin current or the spin hall angle in the material (SHA), related to the conversion of the charge to spin current. Martin Gradhand et al in 2010 [98] studied the tailoring of the SHA and spin diffusion length (sdl) based on the introduction of dilute amount of impurities such as C, N and Bi in Cu, Au or Pt. They found that they were able to modify the SHA and sdl in light host materials such as Cu and Au but not in Pt. The reason behind that was that the role of impurities in materials with strong spin-orbit interaction is minor.

Niimi et al [99] in 2011, used a lateral spin valve of Py/Cu that had a spin sink of a CuIr alloy as a nanowire positioned perpendicularly to the Cu channel. They found that by changing the concentration of the Ir impurities in CuIr from 1% to up to 12%, the SHA would increase from 2.1% to 2.6%.

In the same year, Mihajlovic et al [100], using a set of Py/Ag lateral spin valves, measured a magnetic field induced enhancement of the spin signal when measured in the Hanlé geometry. They attributed this behaviour to magnetic impurities that resided in the vicinity of the Py/NM interface due to the shadow deposition. The impurities magnetisation would be random at zero field and they would act as scattering centres leading to a decrease of the ΔRs. By increasing the external magnetic field the impurities would polarise resulting to a recovery of the ΔRs.

In 2012, Christian Herschback at al [97] theoretically predicted that it was possible to enhance the SHA angle in Au by introducing Pt impurities-adatoms. The key factors

for their calculations were two. The first one was the thickness of the host material that varied from 1 to 32 monolayers and the second one was the position of the Pt impurities within the Au. They found that the SHA would strongly be affected by both factors. More specifically it was observed a V shaped dependence of the SHA to the position of the adatoms with the minimum occurring with the Pt impurities in the middle of the film.

In 2014 Niimi et al [101] performed a similar to the [99] experiment but this time the SHE nanowire was either Bi or Pb doped Cu, or Bi doped Ag. Amongst the different combinations, the CuBi alloy presented the biggest SHA of -0.24 followed by the CuPb alloy with s SHA of -0.13.

Focusing more on the scattering from dilute magnetic impurities in the NM channel, it was found that when they were randomly dispersed [64], or when they were hosted in the FM/NM interface [60] or even when they were on the NM side walls [51, 52] it only led to a decrease of the ΔRs.

In 2016 and 2017 two studies published from the C. Leighton group from L.O'Brien et al [102] and Watts et al [103] found that by annealing the lateral spin valves at temperatures between 80 ^{o}C and 500 ^{o}C they could introduce magnetic impurities into the NM, suppressing thus the ΔRs. In [102] it was also found from calculations that the concentration of impurities would move from areas near the FMs to closer to the centre of the channel by increasing the annealing temperature.

In 2017, Hamaya et al, [104], studied the effect of a pure spin current on the Kondo effect using a Cu(Fe) transport channel. The found that by changing only the FM separation, would result in a linear change of the temperature where the ΔRs peaks. That contradicts the Kimura et al [51], where their data presented a change of the ΔRs_{max} only a function of thickness of the NM channel.

From the literature mentioned, it seems that the impurities in general should be able to modify the behaviour of the spin currents as a function of temperature. The question that most studies were focusing using the lateral spin valve geometry was where do these MI derive from, as it was discussed in chapter 4 as well. The main finding was that by introducing MI in the NM deliberately or accidentally through the FM/NM interface, or the through the host material, or even because of the shadow deposition, that would result in a suppression of the initial spin accumulation in the FM/NM vicinity.

What is missing so far, is an experimental study of the theoretical predictions of the modification of the sdl as a function of the MI position. Chapter 7 is focused on this missing piece of the impurities puzzle.

6.2 Sample fabrication

The devices were fabricated in the cleanroom using a combination of conventional optical lithography, electron beam evaporation through a shadow mask, defined by electron beam lithography on a MMA/PMMA resist bilayer, and lift-off techniques. The samples where patterned on a JBX-6300FS JEOL scan electron beam lithography system with a resolution of 10 nm, on a 100 nm thick thermally oxidised SiO_2. More about the device fabrication can be found in chapter 3.

For the reference devices, two Py electrodes, 30 nm thick and 100 nm and 150 nm wide injector and detector respectively, were e-beam evaporated at an angle of 45^o to the substrate plane. This step was followed by the e-beam evaporation of 0.5 Å of Fe normal to the sample plane. The final step was the thermal evaporation of 100 nm thick Ag normal to the sample plane as well, in a 100 nm wide channel, under the pressure of mid to low 10^{-9} mbar. The ferromagnetic separation varied from 350 nm up to 3000 nm and the purity of the materials was 99.95 % for the Py source, 99.99% for Fe and 99.99% for the Ag source.

For the doped devices, the Py electrodes were deposited the same way as the reference devices. The difference was in the deposition of the normal metal channel. Depending on the position of the delta layer, a percentage of the Ag channel would be deposited and the growth would be interrupted by the e-beam evaporation of 0.5 Å of Fe and resumed for the rest of the channel so as to reach 1000 Å. Given that the deposition rate of the deposited Fe delta layer was between 0.06 Å/s to 0.1 Å/s, the thickness of the 0.5 Å could be easily controlled with a mechanical shutter. Five horizontal positions were used for the δ layer, at the 10%, 25%, 50%, 60% and 75% of the full channel thickness, as shown in the figure 6.1 for two positions. For the rest of the chapter, the six positions will be represented as $\delta Fe_{1/10}$, $\delta Fe_{1/4}$, $\delta Fe_{1/2}$, $\delta Fe_{3/5}$ and $\delta Fe_{3/4}$. The reason why was not attempted growth of a doped device with the delta layer closer to the top surface was to avoid possible oxidation of the magnetic layer. A typical device like that is depicted in figure 6.1.

The measurements and analysis of the IVs, in order to extract the spin diffusion

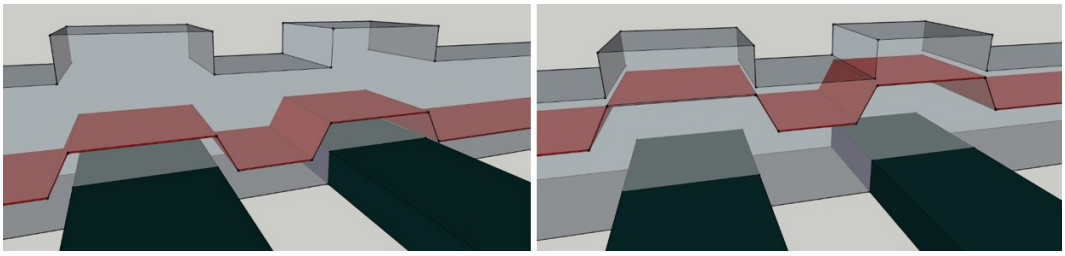

Figure 6.1: *Magnetic impurities in two different horizontal positions in the normal metal channel. The dark green nanowires are the Py wires, grey is the Ag bar and the pink is the 0.5 Å Fe layer.*

properties, was a combination of the analysis followed in chapters 4 and 5. The low temperature behaviour of the non-local IVs presented interesting features as a function of temperature and could not be fitted using the normal second order polynomial equation. What was used instead was the current sign dependent analysis and after a specific temperature where the effect would disappear, the IV data could be properly fitted using the polynomial fitting.

6.3 Electron transport measurements and non-local IVs

Before the spin transport measurements, the resistance as a function of temperature of the normal metal channel was measured. Since magnetic impurities were introduced into the NM channel, an upturn in the resistance at low temperature was expected, shown in figure 6.2, despite the fact that the impurities layer is concentrated in one level of the bar and not homogeneously dispersed.

The upturn in the resistance data was present in all separations and horizontal positions of the impurities layer. The temperature minimum does not vary with the position of the delta layer and averages to 8.0 $\pm$ 0.5 K. Since the temperature minimum of the resistance is related to the concentration of the magnetic impurities [38], a small variation in the T_{min} is an indication of a repeatable thickness of the δ layer across the different separations and sets of devices. The local IVs of the different part of a device were linear, presenting an ohmic behaviour. The non-local IVs behaviour was on the one hand normal at the high temperature regime, but changed completely at low temperatures. They presented an increase of the voltage at low currents that followed a Gaussian shape, as it will be shown later, and then at larger currents it followed the

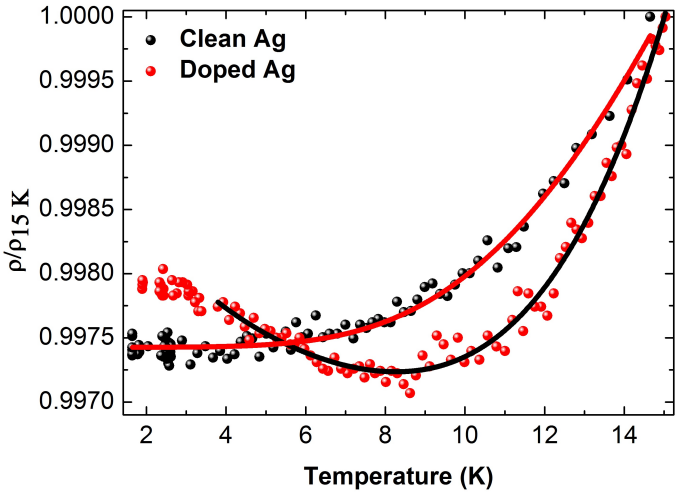

Figure 6.2: *A comparison of the resistivities of a nominally clean and a doped silver channel. To make the upturn more obvious, the data were normalised to the resistivity at 15 K.*

normal non-local IV quadratic shape.

6.4 W-shaped non-local IVs

6.4.1 W-shaped IVs as a function of temperature

What was noticed while measuring the Fe-doped devices, was that no matter where the impurities were placed into the NM channel, at temperatures below 20 K, the shape of the non-local IV would change to a combination of two second order polynomials for each current sign, as shown in figure 6.3.

The difference of this type of IV compared to all the non-local IVs recorded so far was that by increasing the current (absolute value) from zero μA, the voltage decreases. The decrease continued with the increase of the current to about ± 300 μA. After that point the trend of the voltage would reverse and start increasing.

The way to analyse these non-local IVs and extract the spin dependent component was the one that was already used in chapter 5 in order to compare the different components depending on the current direction. The two different current branches of the non-local IVs were fit using a second order polynomial, and then the output was averaged for the linear component. The presented effect has a temperature dependence since the zero bias increase of voltage decreases as the temperature increases, and is

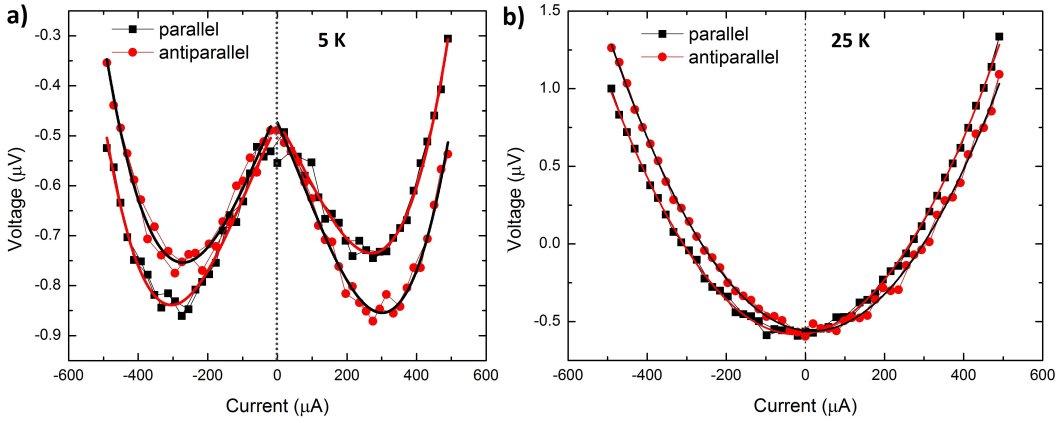

Figure 6.3: *a) W-shaped IV in the parallel and antiparallel state and at 5 K. The solid lines are second order polynomial fittings for each current direction. In b) is the normal non-local IVs for parallel and antiparallel state at 25 K. The solid lines are the second order polynomial fittings.*

shown in figure 6.3.

To calculate the magnitude of the zero bias effect to see if it's related to the magnetic impurities that were introduced, on the other hand, the following method was employed. A second order polynomial was used to fit only the high current data of the IVs (above ± 300 μA, where the detected voltage had a normal increasing trend with the current) and produce the conventional quadratic shape. The data of the measured IV were subtracted from those that resulted from fitting the high current regime. The described method was summarised in figure 6.4.

For a better understanding of the evolution of the magnitude of the signal as a function of temperature, the values of V_{0min} at zero current, were subtracted from those for V_{0max} at zero current as shown in figure 6.4. This ΔV decreased with temperature in a linear way from 5 up to about 10 K. After that it decayed and reached a point where the second order polynomial describes perfectly the non-local IV, close to 20 K. A summary of that is in figure 6.5.

Unfortunately the effect fades out at temperatures almost four times higher than the calculated, from Costi et al [105], Kondo temperature of Fe in Ag (27 ± 3 ppm and 67.5 ± 7.0 ppm was used for experiment and calculations) of 5 K. Moreover the 20 K limit is about 2.5 times larger than the Kondo minimum measured in the resistance as a function of temperature for the samples used. That makes it harder to directly

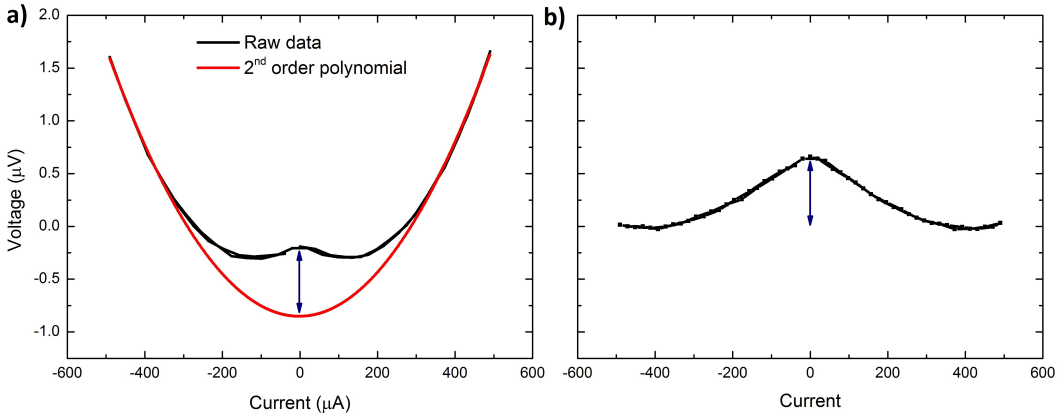

Figure 6.4: *W-shaped non-local IV along with the second order polynomial fitting, using only the high current regime. On the right is the resulted difference between the fitting based on the high bias data and the actual data.*

attribute the effect to the magnetic impurities.

Since the presented effect is new, it was necessary to analyse it as a function of ferromagnetic separation and external magnetic field before continuing to the spin diffusion properties of the devices with the δ layers.

6.4.2 W-shaped IVs as a function of separation and external magnetic field

While measuring the devices with the Fe doping layer, it was noticed that the peak in the centre of the NLIV was increasing in size as the separation was increasing. As shown in figure 6.6, it was not true and caused because of a decrease in the spin dependent component with respect to the magnitude of the peak. To further study this behaviour, the procedure followed was the same as in the last paragraph, using the high current data, fit them and extract the two signals depending on the current direction. The results were summarised in figure 6.6 were for separations of 350 nm up to 1800 nm. That includes the measured separations of all the devices with the δ layer within the Ag channel at all 5 different positions.

Apparently from the fittings and subtractions, it was concluded that the magnitude of the remaining signal was almost the same across the different separations for the different positions. In more detail, for the $\delta Fe_{1/10}$ was 0.24 $\pm$ 0.04 μV, for the $\delta Fe_{1/4}$ was 0.57 $\pm$ 0.06 μV, for the $\delta Fe_{1/2}$ was 0.51 $\pm$ 0.03 μV, for the $\delta Fe_{3/5}$ was 0.32 $\pm$ 0.03

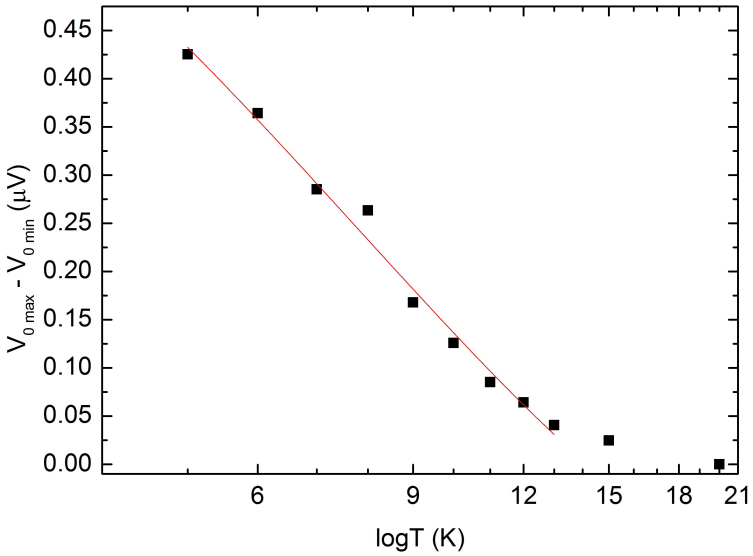

Figure 6.5: *Difference of the voltages at zero current between the W-shaped IVs and the second order polynomial fitting. The change of the difference is linear between 5 and 11 K and then decays to reach a temperature where the difference is zero at 20 K.*

μV and finally for the $\delta Fe_{3/4}$ was 0.55 $\pm$ 0.04 μV. The value of the voltage signal was the mean value across the separations and the error the standard error on the mean. In figure 6.6 the mean value is represented as the coloured solid line, colour-coded the same way as the voltage signals recorded for the different positions.

To further study the behaviour of the IVs, they were tested as a function of external magnetic field. The field used was from -3T up to 3T. The recorded measurement is presented in figure 6.7.

The presented signal had no field dependency. The magnitude of the zero bias voltage was almost fixed at 0.52 $\pm$ 0.02 μV. To make sure that the doped devices had not formed a spin glass, the spin signal as a function of temperature was measured by cooling without an external magnetic field.

Once the measurements finished, a 5 T field was applied along the easy axis of the Py electrodes and the sample was cooled down to repeat the non-local resistance measurements. The temperature behaviour of the Δ Rs was exactly the same.

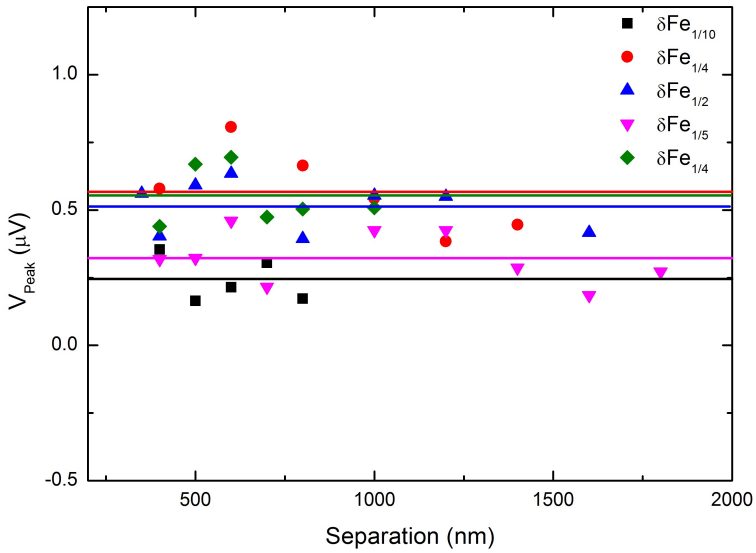

Figure 6.6: *Magnitude of the zero bias peak across the different separations and δ layer positions measured and at 5 K. Across the different separations for each δ layer position, the magnitude fluctuates around a constant value, represented by the solid lines, colour-coded to the MI position.*

6.5 Spin diffusion properties

6.5.1 Dependency of the spin signal on the position of the delta layer

Doping the devices at different horizontal positions of the normal metal channel, led to changes in the spin transport properties of the devices. Apart from the shape of the non-local IVs, the temperature response of the spin signal was modified as well, as depicted in figure 6.8.

The reference devices with the doping layer at the bottom interface presented a mild downturn at 15 K. By introducing the magnetic impurities layer in the Ag channel, the maximum of the spin signal moved closer to 100 K. Finally the set of devices with the doping in the $\delta Fe_{3/4}$ (75% from the top interface) presented their maximum signal up to almost 250 K.

In figure 6.8 a, is the temperature where the maximum of the spin signal is observed across the different positions and separation. The inset of 6.8 a includes all the different positions of the magnetic impurities layer in the Ag channel. Focusing on the extreme positions, even when the impurities are are the bottom interface, a small downturn

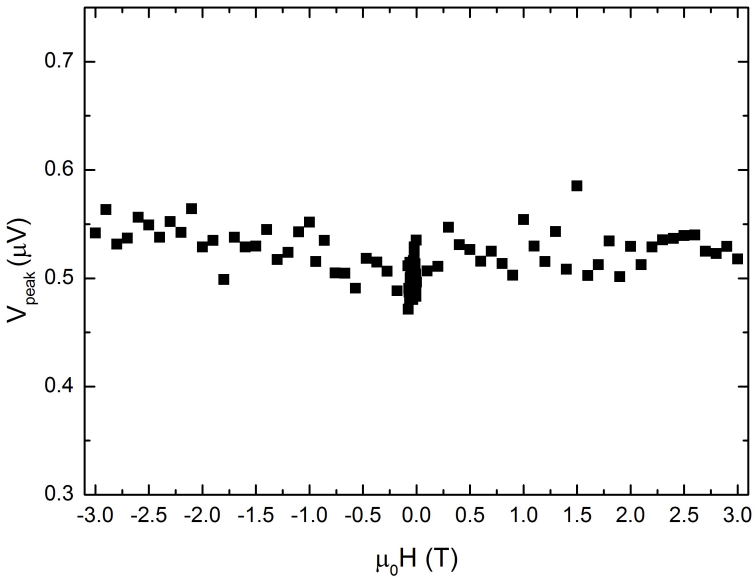

Figure 6.7: *Magnetic field dependence of the V_{0max} - V_{0min} for one of the devices with a separation of 1200 nm, at 5 K.*

was observed (position of impurities was at 0%) at 18.5 ± 2.5 K. On the other hand, having the impurities at the 75% position of the full thickness, pushed the maximum temperature for the ΔRs to 240 ± 14 K.

In the four different positions with the MI within the channel the maximum temperature presents a mild increase until the $\delta Fe_{1/2}$ and then starts to drop again. For the $\delta Fe_{1/10}$ position the maximum was at 100 K and then increases with the position to 103 ± 8 K, 111 ± 7 K and finally 98 ± 4 K.

Figure 6.8 b is the spin signal as a function of temperature and MI position for the 400 nm separation. In general, the spin signal of the reference device is the higher one at all temperatures. The interesting thing is that the device with the MI in the middle of the channel and for temperatures $\geqslant$ 60 K exhibits a ΔRs that is greater than that of the nominally clean NM. At higher separations the effects disappears but the trend of the spin signal of the devices with MI within the channel remains the same with that presented in figure 6.9.

In figure 6.9 is shown the ΔRs as a function of position at 400 nm and for five different temperatures. The symbols are the values of the ΔRs and are colour-coded with respect to the position of the impurities. In contrast to the temperature dependence of the maximum ΔRs where there is a mild dependence of the position of the MI, in the

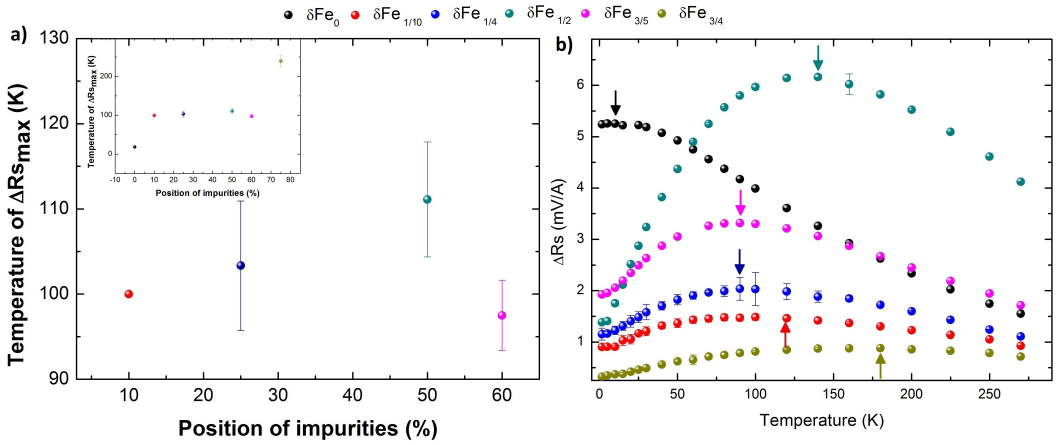

Figure 6.8: *In (a) is the temperature where the ΔRs gets its maximum value across the different separations and positions of the δ layer. The inset of 6.8 is focused on the δRs_{max} for the layers between $\delta Fe_{1/10}$ and $\delta Fe_{3/5}$ that presents a mild increase up to $\delta Fe_{1/2}$ and then drops. The error bars come from the standard deviation of the means. In (b) is presented the ΔRs as a function of temperature for all the δ layer positions at a L_{FM} of 400 nm.*

actual temperature dependence of the ΔRs, the trend is a lot clearer.

The spin signal increases with the position of the MI presenting a maximum when the impurities are in the middle of the transport channel and then decreases moving towards either end of the NM channel. The observation agrees with [97] where it was theoretically predicted that the spin Hall angle by introducing impurities, Pt in Au for their calculations, will vary with the positions of the impurities layer (IL). More specifically, the SHA_{xx} would increase by adding ad-atoms closer to the centre of the film. An increase in the SHA means that the scattering from impurities is larger.

In the spin current part, on the other hand, larger scattering leads to smaller spin signal. In [97] they calculated a large SHE in the centre of the channel that reduces moving away from that area, which agrees with the measurements using the pure spin currents.

6.5.2 Spin diffusion length as a function of the position of the impurities

The spin diffusion length in the normal metal channel is related to how fast the spin signal decays across the different separations and not on the magnitude of it.

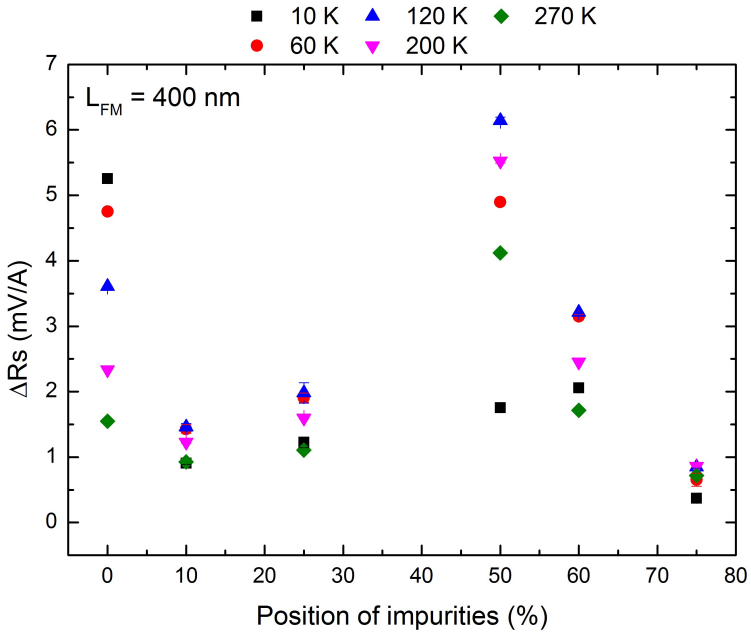

Figure 6.9: *ΔRs as a function of MI position at five different temperatures for a separation of L_{FM} = 400 nm. The spin signal decreases moving the IL from the reference device (δFe_0) to the first position closer to the bottom interface ($\delta Fe_{1/10}$). After that, an increase was observed while moving the IL closer to the centre ($\delta Fe_{1/2}$). After that point and as the IL was moved closer the top interface, the ΔRs kept decreasing.*

Given that the mean free path of the electrons is bigger than the device's cross sectional area, which means that the electrons will get scattered from the MI no matter where they were placed; it would be expected that the spin signal should not be affected from the position of the δ layer. The results presented in 6.4.1 suggested a behaviour that does not agree with that though. The ΔRs is strongly correlated to the position of the MI as it has already been shown in figures 6.8 and 6.9.

The diffusive behaviour of the spins further supports it. The spin diffusion length of all the devices was calculated using the same method as in chapter 4 and for the different MI positions it is summarised in figure 6.10.

It can be seen that the response of the sdl length is strongly correlated to the position of the magnetic impurities as it increases by moving it from the bottom Py/Ag interface to the centre of the channel. Moving the position of the δ layer from that point and closer to the top interface, the sdl started to decrease giving an inverted V-shaped behaviour as a function of the position. Interestingly the sdl of the devices with the

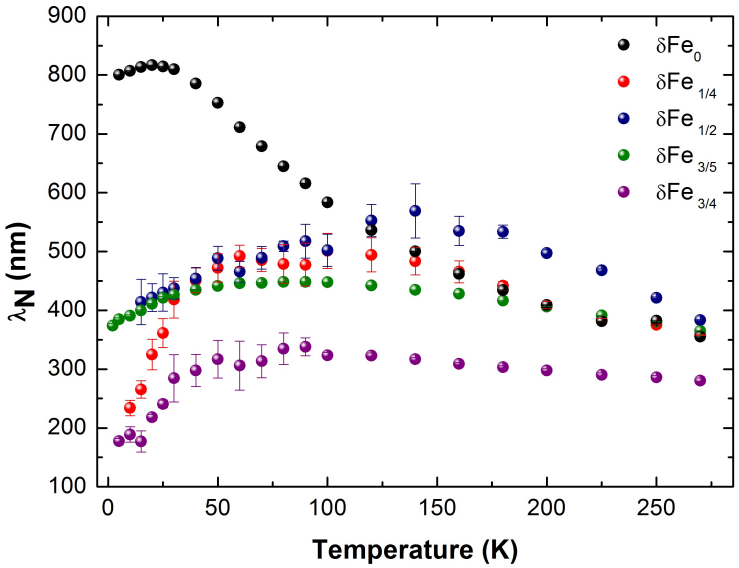

Figure 6.10: *Spin diffusion length as a function of temperature and δ layer position. Although below 100 K the reference device presents the maximum diffusion length, the behaviour is more complicated for temperatures above 140 K, where the $\delta Fe_{1/2}$ dominates. The reference device along with the $\delta Fe_{3/5}$ and $\delta Fe_{1/4}$ present the same diffusion length.*

δFe$_(1/2)$ exceeded that of the reference device for temperatures above 100 K and up to room temperature. That was not unexpected because the ΔRs of this set of devices had a relatively low decay as a function of temperature after peaking at about 110 K.

6.6 Conclusions

Chapter 6 summarises results acquired from lateral spin valves where magnetic impurities where deliberately placed in the normal metal channel. The idea behind this experiment was to study how the pure spin current behaviour could be affected by introducing less than a monolayer of magnetic impurities at different horizontal positions of the normal metal channel. A study from Herschbach et al [97] suggested that the positions of the impurities in a host material could heavily affect the response of the SHA.

The case in the current study is slightly different since the thickness of the transport channel was 1000 Å of Ag and quantum confinement calculations were based in a few monolayers. Nonetheless the experiment was fruitful and interesting conclusions were

drawn from it.

First of all, by introducing magnetic impurities in the transport channel, the Kondo upturn in the resistance as a function of temperature measurements appeared, for T < 10 K, as expected when introducing Fe in Ag. The MIs layer resulted in a non-local IV shape different from the normal quadratic shape that presented a zero bias anomaly.

The zero bias anomaly was studied as a function of temperature, separation and external magnetic field to find that it only depends on the temperature. The maximum of it was found to be independent to the separation and magnetic field but decayed as the temperature increased from about 2 K to 20 K, where the NLIV obtained its characteristic response. Unfortunately the 20 K temperature mark is far away from the Kondo minimum presented in the resistivity of the devices at about 8.0 ± 0.5 K but still not in the linear regime of the resistivity where the phonon scattering is responsible for the biggest part of the signal. That could attribute the NLIV response to impurities in the channel but unfortunately there is no other study that could support it.

Furthermore, the position of the δ layer affected the spin signal picked up at the detector junction. It was found that the ΔRs would increase as the Fe impurities layer would be placed closer to the centre of the Ag channel and then drop at positions closer to the top interface. The ΔRs as a function of temperature revealed that the maximum signal would be obtained for temperatures above the usual 30 K mark of the literature for MI randomly dispersed in the NM, and in some cases would be above 250 K ($\delta Fe_{3/4}$). One other interesting feature was that the response was modified in such a degree that the ΔRs of the $\delta Fe_{1/2}$ and for low separations, presented a higher value than that of the reference device with MI at the bottom interface.

Finally, the spin diffusion length as a function of temperature for the different devices was calculated as well. The decay of the spin signal with the separation was found to present a similar to the spin signal trend with sdl of the $\delta Fe_{1/2}$ to exceed that of the reference device at high temperatures. Moreover the position of the MI layer affected the sdl of the rest of the devices where it increased by moving it from the bottom interface to the centre and then decreased moving closer to the top interface.

The observed effect is new and further experiments required in which Ag is doped with different and possibly non-magnetic materials. Ideally all the different separations and doping positions would be deposited within one vacuum cycle. The samples used for this chapter, were deposited within a period of 10 months.

Chapter 7

Conclusions

This thesis is focused on the spin (chapters 4 and 6) and heat (chapter 5) diffusion properties of Ag, measured using the lateral spin valve geometry.

7.1 Conclusions

In chapter 4, two sets of lateral spin valves were grown using Permalloy for the FM channels and Ag for the NM channel. The same 0.1Å/s deposition rate was used for the Py electrodes, whereas for the Ag channel was used 0.2 Å/s and 0.4 Å/s respectively. The devices were grown under similar conditions of pressure, using the same source material. It was found that the change in the deposition rate had strongly affected the spin transport properties in the NM as the characteristic downturn in the spin signal was absent in the 0.4 Å/s set. In addition to that, the spin diffusion length of the 0.4 Å/s devices was more than twice as long as what was calculated using the 0.2 Å/s devices, following a trend similar to the mean free path of the electrons.

The resistance as a function of temperature measurements for the NM channels revealed that none of the devices presented a Kondo upturn at low temperatures and also that the resistivity of the device with the fast grown Ag was lower. Using XRD and SEM, it was shown that the grain size in the c axis doubled and laterally was increased by almost a factor of 10, after doubling the deposition rate.

That leads to the conclusion that the deposition rate can strongly affect the spin transport properties through the grain boundaries in such a degree that the downturn of the spin diffusion length at low temperatures was not apparent for the devices grown with a bigger deposition rate.

Chapter 5 was focused on the thermal effects presented when using the lateral spin valve geometry as Joule heating and the Peltier effect contribute to the detected non-local voltage. The detector junction works effectively as a thermocouple and hence the voltage in the detector can provide information about the thermal effects as well. It was found that the signal of the aforementioned effects has a strong temperature dependence and their behaviour can be explained taking into account the competition of the thermal conductivity of the substrate and the normal metal, combined with the temperature dependence of the thermopowers of the materials used in the bimetallic junctions.

The Scanning Thermal Microscopy was employed to map the temperature distribution of the individual thermal components for the first time in literature on a LSV.

The temperature decay in the NM channel was measured along with the temperature drops in the injector and detector junctions. The experimentally measured temperature decay along the normal metal channel was fitted using the analytical model that was developed. In addition, the temperature drop in the detector junction was calculated using the transport data and assuming bulk values for the Seebeck coefficient of Py and Ag.

Furthermore, in order to focus purely on the thermal signals rising from the injector junction, V replaced Py as thermal injector/detector. The combination of Ag and V leads to an effective Seebeck coefficient that has a transition from positive to negative values. That resulted to a change in the sign in the non-local IVs and in extension, at the temperature where $S_{effective}$ was zero, no detection of thermal effects at all.

As the Peltier effect is linear to the applied currentit affects the BLR depending on the charge current direction in the injector junction. For the positive and negative current sign, the BLR splits from 270 K down to 2 K. The difference between the two branches starts to increase significantly below 30 K. The non-local resistance in the parallel and antiparallel state, were affected as well. The splitting in these though, was the same within the error as a function of temperature and so the spin signal, defined as the difference between the non-local resistance in the parallel and antiparallel state, remained unaffected.

The effect was tested on five different combinations of materials, 3 cryostats, 3 transport sticks and 2 sample holders in total, to confirm the absence of artefacts. It was found that at 5 K the magnitude of the splitting was independent to the separation, for L_{FM} between 350 nm and 1600 nm, but was related to the material combination. To confirm that the effect was purely thermal, the Py electrodes were replaced with V and was found was that the splitting in the baseline resistance branches was still present.

The last experimental part of the thesis, in chapter 6, was focused on the interaction between the pure spin currents and magnetic impurities. It was inspired by a theoretical studies where it was predicted that the spin Hall angle and the spin diffusion should be affected by both the presence and the position of impurities in a host material. The impurities would form a delta layer (discontinuous-dusting layer) and depending on its horizontal position in the host material and due to quantum confinement, it would modify the spin Hall angle in the host.

For this experiment six sets of devices were prepared. The difference of these to the rest used in the other studies included, was that 0.5 Å of Fe was deposited at different horizontal positions in the normal metal channel. The positions varied from the bottom Py/Ag interface, up to close to the top surface of the Ag channel. A Kondo upturn appeared in the resistivity measurements at 8.0 ± 0.5 K. Apart from that, the non-local IVs presented a kink at low biases and below 15 K, that was attributed to the existence of impurities in the NM. The magnitude of this zero bias anomaly was proportional to logT, behaviour that can confirm to rise from magnetic impurities. The zero bias magnitude was also measured as a function of separation and magnetic field, but presented no correlation.

The spin signal of the devices had an interesting behaviour as a function of position. Firstly the temperature where the ΔR_s was maximised, had a mild impurities position dependence apart from the reference (impurities below the Ag channel) and the extreme top end device. The actual signal though had a very clear position dependence as it would increase as the impurities layer would move closer to the middle of the channel and would start reducing after that.

A similar behaviour was observed for the calculated spin diffusion lengths. At low temperatures, T > 100 K, the reference device presented the longer diffusion length by at least 400 nm, followed by the λ of the devices in the centre and close to the centre of the NM channel. At high temperatures, the trend was significantly modified, since the λ of the device with the impurities in the centre of the channel prevailed with a maximum at 140 K. It was shown that the spin diffusion length can be significantly altered by engineering the position of the MI instead of trying to avoid having them in the first place.

7.2 Outlook

The lateral spin valve geometry can be useful for a big variety of experiments, only a small part of which, was studied in this thesis. From the experiments performed there were some interesting results that came up, included in chapters 5 and 6. Unfortunately, as most of these results are new, further studing is required in order to fully understand them.

The future experiments suggested are based on these. The first one is related to the analytical model developed for the calculation of the injector and detector junction

temperature. The model predicts a continuous increase of the junctions' temperature with a decrease of the substrate temperature below 80 K. To confirm if that is true, a junction with a normal metal and a superconductor (as and thermal injector/detector) is needed. The critical temperature for one of the electrodes can be measured using the local geometry. After that, non-local IVs of the detector should be recorded at a temperature below the critical temperature that was measured. The transition from a NLIV at the SC state to a normal NLIV at different currents will resolve this issue directly.

The second experiment is about the observed splitting in the baseline resistance. Given that the effect is visible even at room temperature, using the SThM one could map the change in the temperature difference due to the change in the current direction and confirm with a different to the transport measurements approach, that the effect is real.

Finally, in the last experiment, in chapter 6, it was observed that the position of the impurities layer affects the response of the NLIV at temperature below 10 K and also the temperature dependence of the ΔR_S and λ. To confirm that the change of the signal is not only because of the magnetic impurities, a similar experiment with non-magnetic impurities could be performed, making sure that the atomic weight of the impurity is quite different to the host material.

References

[1] F. Casanova, A. Sharoni, M. Erekhinsky, and I. K. Schuller, "Control of spin injection by direct current in lateral spin valves," *Physical Review B*, vol. 79, no. 18, p. 184415, 2009.

[2] E. L. Villamor, *Injection, transport and manipulation of pure spin currents in metallic lateral spin valves.* PhD thesis, University of the Basque Country, 2014.

[3] P. Laczkowski, *Spin currents and spin Hall effect in lateral nano-structures.* PhD thesis, University of Grenoble, 2012.

[4] Y. Ji, A. Hoffmann, J. Jiang, and S. Barder, "Non-local spin injection in lateral spin-valves," *Applied Physics Letters*, vol. 40, no. 5, pp. 1280–1284, 2007.

[5] R. Barnard, *Thermoelectricity in metals and alloys.* Taylor and Francis Ltd, 1972.

[6] J. Batley, "Pure spin currents." Transfer report, 2012.

[7] K. Shigeto, T. Shinjo, and T. Ono, "Injection of a magnetic domain wall into a submicron magnetic wire," *Applied Physics Letters*, vol. 75, p. 2815, 2009.

[8] T. Kimura, Y. Otani, I. Yagi, K. Tsakagoshi, and Y. Aoyagi, "Suppressed pinning field of a rapped domain wall due to direct current injection," *Journal of Applied Physics*, vol. 94, no. 11, 2003.

[9] F. Menges, H. Riel, A. Stemmer, and B. Gotsmann, "Nanoscale thermometry by scanning thermal microscopy," *Review of Scientific Instruments*, vol. 87, no. 87, pp. 74902–114901, 2016.

[10] M. Johnson and R. H. Silsbee, "Calculation of nonlocal baseline resistance in a quasi-one-dimensional wire," *Physical Review B - Condensed Matter and Materials Physics*, vol. 76, no. 15, pp. 1–4, 2007.

[11] C. Chappert, A. Fert, and F. Nguyen van Dau, "The emerge of spin electronics in data storage," *Nature Materials*, no. 6, pp. 813–823, 2007.

[12] M. Baibich, J. Broto, A. Fert, F. Nguyen Van Dau, F. Petroff, P. Eitenne, G. Creuzet, A. Friederich, and C. J., "Giant magnetoresistance of (001)Fe/(001)Cr magnetic superlattices," *Physical Review B*, vol. 61, no. 21, pp. 2472–2475, 1988.

[13] G. Binasch, P. Grunberg, F. Saurenbach, and W. Zinn, "Enhanced magnetoresistance in layered magnetic structures with antiferromagnetic interlayer exchange," *Physical Review B*, vol. 39, no. 7, pp. 4828–4830, 1989.

[14] J. Nogues and I. Schuller, "Exchange bias," *Journal of Magnetism and Magnetic Materials*, no. 192, pp. 203–232, 1999.

[15] E. Masourakis, L. Arzubiaga, G. Mihajlović, E. Villamor, R. Llopis, F. Casanova, and L. Hueso, "Modulation of spin accumulation by nanoscale confinement using electromigration in a metallic lateral spin valve," *Nanotechnology*, vol. 27, p. 095201, 2016.

[16] M. R. Kaspers, A. Bernhart, F.-J. Meyer Zu Heringdorf, G. Dumpich, and R. Möller, "Electromigration and potentiometry measurements of single-crystalline Ag nanowires under UHV conditions.," *J. Phys.: Condensed matter*, vol. 21, no. 26, p. 265601, 2009.

[17] D. Josell, S. H. Brongersma, and Z. Tokei, "Size-Dependent Resistivity in Nanoscale Interconnects," *Annual Review of Materials Research*, vol. 39, no. 1, pp. 231–254, 2009.

[18] W. Ma and X. Zhang, "Study of the thermal, electrical and thermoelectric properties of metallic nanofilms.," *International Journal of Heat and Mass Transfer*, vol. 58, no. 1-2, pp. 639–651, 2013.

[19] Q. Huang, C. M. Lilley, M. Bode, and R. Divan, "Surface and size effects on the electrical properties of Cu nanowires," *Journal of Applied Physics*, vol. 104, no. 2, pp. 1–6, 2008.

[20] K. Tsuchiya, Y. Li, and M. Saka, "Consistent melting behavior induced by Joule heating between Ag microwire and nanowire meshes.," *Nanoscale research letters*, vol. 9, no. 1, p. 239, 2014.

[21] M. Hummelgård, R. Zhang, T. Carlberg, D. Vengust, D. Dvorsek, D. Mihailovic, and H. Olin, "Nanowire transformation and annealing by Joule heating," *Nanotechnology*, vol. 21, no. 16, p. 165704, 2010.

[22] S. Takahashi and S. Maekawa, "Spin current, spin accumulation and spin Hall effect," *Sci. Technol. Adv. Mater.*, vol. 9, no. 1, p. 014105, 2008.

[23] T. Yang, T. Kimura, and Y. Otani, "Giant spin-accumulation signal and pure spin-current-induced reversible magnetization switching," *Nature Physics*, vol. 4, no. 11, pp. 851–854, 2008.

[24] I. Žutić, J. Fabian, and S. D. Sarma, "Spintronics: Fundamentals and applications," *Reviews of Modern Physics*, vol. 76, no. 2, pp. 323–410, 2004.

[25] P. Laczkowski, L. Vila, S. Ferry, A. Marty, J. M. George, H. Jaffrès, A. Fert, T. Kimura, T. Yang, Y. C. Otani, and J. P. Attané, "Spin signal in metallic lateral spin valves made by a multiple angle evaporation technique," *Applied Physics Express*, vol. 4, no. 6, 2011.

[26] S. O. Valenzuela, "Nonlocal electronic spin detection, spin accumulation and the spin Hall effect," *Int. J. Mod. Phys. B*, vol. 23, p. 2413, 2009.

[27] Y. Ji, A. Hoffmann, J. Jiang, and S. Barder, "Spin injection, diffusion and detection in lateral spin-valves," *Applied Physics Letters*, vol. 25, no. 25, pp. 6218–6220, 2004.

[28] F. J. Jedema, M. S. Nijboer, A. T. Filip, and B. J. van Wees, "Spin injection and spin accumulation in permalloy-copper mesoscopic spin valves," *Physical Review B*, vol. 67, no. 16, p. 085319, 2003.

[29] N. F. Mott, "Electrons in transition metals," *Advances in Physics*, vol. 13, no. 51, pp. 325–422, 1964.

[30] I. Cambel, A. Fert, and A. Pomeroy, "Evidence for two current conduction in Iron," *Philios. Mag.*, no. 15, pp. 977–983, 1967.

[31] T. Valet and A. Fert, "Theory of the perpendicular magnetoresistance in magnetic multilayers," *Physical Review B*, no. 48, p. 7099, 1993.

[32] Y. Ji, A. Hoffmann, J. E. Pearson, and S. D. Bader, "Enhanced spin injection polarization in Co/Cu/Co nonlocal lateral spin valves," *Applied Physics Letters*, vol. 88, no. 5, p. 052509, 2006.

[33] F. Jedema, M. Costache, H. Heersche, J. Baselmans, and B. van Wees, "Electrical detection of spin accumulation and spin precession at room temperature in metallic spin valves," *Applied Physics Letters*, vol. 81, no. 27, pp. 5162–5164, 2002.

[34] F. Jedema, H. Heersche, A. Filip, J. Baselmans, and B. van Wees, "Electrical detection of spin precession in a metallic mesoscopic spin valve," *Nature*, no. 416, pp. 713–716, 2002.

[35] Y. Otani and T. Kimura, *Nonlocal spin valves in metallic nanostructures.* Taylor Francis Group, LLC, 2001.

[36] J. Bass and W. Pratt Jr, "Spin-diffusion lengths in metals and alloys, and spin-flipping at metal/metal interfaces: an experimentalist's review," *J.Phys.: Condens. Matter*, vol. 19, no. 19, p. 183201, 2007.

[37] S. Takahashi and S. Maekawa, "Spin injection and detection in magnetic nanostructures," *Physical Review B*, no. 67, p. 052409, 2003.

[38] J. Kondo, "Resistance minimum in dilute magnetic alloys," *Progress of Theoretical Physics*, vol. 32, no. 1, pp. 37–49, 1964.

[39] M. Johnson and R. Silsbee, "Interfacial charge-spin coupling: injection and detection of spin magnetization in metals," *Physical Review Letters*, no. 55, pp. 1790–1793, 1985.

[40] C. Kittel, *Introduction to solid state physics.* John Wiley and Sons, inc, 2005.

[41] P. Tipler, *Physics for Scientists and Engineers.* W.H. Freeman and Company, 1999.

[42] G. Mihajlovic, D. K. Schreiber, Y. Liu, J. E. Pearson, S. D. Bader, A. K. Petford-Long, and A. Hoffmann, "Enhanced spin signals due to native oxide formation in Ni80 Fe20 /Ag lateral spin valves," *Applied Physics Letters*, vol. 97, no. 11, pp. 103–106, 2010.

[43] F. Lecocq, C. Naud, I. Pop, Z. Peng, I. Matei, T. Crozes, T. Fournier, W. Guichard, and O. Buisson, "Novel E-beam lithography technique for in-situ junction fabrication: the controlled undercut," *Hybrid Open Access*, vol. 22, p. 315302, 2011.

[44] B. Cord, C. Dames, K. Berggren, and J. Aumentado, "Robust shadow-mask evaporation via lithographically controlled undercut," *J. Vac. Sci. Technol. B*, vol. 24, p. 3139, 2006.

[45] M. C. Rosamond, J. T. Batley, G. Burnell, B. J. Hickey, and E. H. Linfield, "High contrast 3D proximity correction for electron-beam lithography: An enabling technique for the fabrication of suspended masks for complete device fabrication within an UHV environment," *Microelectronic Engineering*, vol. 143, pp. 5–10, 2015.

[46] M. Costache, G. Bridoux, and I. Neumann, "Robust shadow-mask evaporation via lithographically controlled undercut," *J. Vac. Sci. Technol. B*, vol. 30, p. 043105, 2012.

[47] T. Schrefl, J. Fidler, K. Kirk, and J. Chapman, "Domain structures and switching mechanisms in patterned magnetic elements," *Journal of Magnetism and Magnetic Materials*, vol. 175, 1997.

[48] J. W. Ekin, *Experimental Techniques for Low-Temperature Measurements: Cryostat Design, Material Properties and Superconductor Critical-Current Testing.* OXFORD University Press, 2006.

[49] M. Abrecht, A. Adare, and J. Ekin, "Magnetization and magnetoresistance of common alloy wires used in cryogenic instrumentation," *Review of Scientific Instruments*, vol. 78, no. 42, p. 046104, 2007.

[50] J. Als-Nielsen and D. McMorrow, *Elemens of modern X-ray physics*. John Wiley Sons, Ltd, 2011.

[51] T. Kimura, T. Sato, and Y. Otani, "Temperature evolution of spin relaxation in a NiFe/Cu lateral spin valve," *Physical Review Letters*, vol. 100, no. 6, pp. 1–4, 2008.

[52] H. Zou and Y. Ji, "The origin of high surface spin-flip rate in metallic nonlocal spin valves," *Applied Physics Letters*, vol. 101, no. 8, p. 082401, 2012.

[53] M. Erekhinsky, F. Casanova, I. Schuller, and A. Sharoni, "Spin-dependent Seebeck effect in non-local spin valve devices," *Applied Physics Letters*, no. 100, p. 212401, 2012.

[54] G. Mihajlovic, J. Pearson, S. D. Bader, and A. Hoffmann, "Surface spin flip probability of mesoscopic Ag wires," *Physical Review Letters*, no. 104, p. 237202, 2010.

[55] Y. Otani and T. Kimura, "Manipulation of spin currents in metallic systems," *Phil. Trans. R. Soc. A*, no. 369, pp. 3136–3149, 2011.

[56] N. Poli, M. Urech, V. Korenivski, and D. Haviland, "Spin-flip scattering at Al surfaces," *Journal of Applied Physics*, no. 99, p. 08H701, 2006.

[57] H. Idzuchi, Y. Fukuma, L. Wang, and Y. Otani, "Spin relaxation mechanism in silver nanowires covered with MgO protection layer," *Applied Physics Letters*, vol. 101, no. 2, p. 022415, 2012.

[58] E. Villamor, M. Isasa, L. E. Hueso, and F. Casanova, "Contribution of defects to the spin relaxation in copper nanowires," *Physical Review B - Condensed Matter and Materials Physics*, vol. 87, no. 9, p. 094417, 2013.

[59] E. Villamor, M. Isasa, L. Hueso, and F. Casanova, "Temperature dependence of spin polarization in ferromagnetic metals using lateral spin valves," *Physical Review B*, vol. 88, no. 18, p. 184411, 2013.

[60] L. O'Brien, M. J. Erickson, D. Spivak, H. Ambaye, R. J. Goyette, V. Lauter, P. A. Crowell, and C. Leighton, "Kondo physics in non-local metallic spin transport devices," *Nature Commun.*, vol. 5, no. 3927, 2014.

[61] S. Chen, H. Zou, C. Qin, and Y. Ji, "Absence of high surface spin-flip rate in mesoscopic silver channels," *Applied Physics Express*, vol. 7, no. 11, p. 113001, 2014.

[62] L.-J. Pan, L. Wang, and L.-Y. Zhang, "Enhanced spin diffusion length by suppressing spin-flip scattering in lateral spin valves," *Rare Metals*, vol. 34, no. 3, pp. 156–159, 2015.

[63] M. Isasa, E. Villamor, L. Fallarino, O. Idigoras, A. K. Suszka, C. Tollan, A. Berger, L. E. Hueso, and F. Casanova, "Spin transport enhancement by controlling the Ag growth in lateral spin valves," *Journal of Physics D: Applied Physics*, vol. 48, p. 215003, 2014.

[64] J. T. Batley, M. C. Rosamond, M. Ali, E. H. Linfield, G. Burnell, and B. J. Hickey, "Spin relaxation through Kondo scattering in Cu/Py lateral spin valves," *Physical Review B*, vol. 92, no. 22, p. 220420, 2015.

[65] R. Hoffman and D. Turnbull, "Lattice and grain boundary self-diffusion in silver," *Journal of Applied Physics*, vol. 22, no. 5, 1951.

[66] F. Johnson and P. Larose, "The diffusion of oxygen through silver," *J. Am. Chem. Soc.*, vol. 46, pp. 1377–1389, 1924.

[67] C. Polop, C. Rosiepen, S. Bleikamp, R. Drese, J. Mayer, A. Dimyati, and T. Michely, "The STM view of the initial stages of polycrystalline Ag film formation," *New J. Phys*, vol. 9, no. 74, 2007.

[68] R. Sennett and G. Scott, "The structure of evaporated metal films and their optical properties," *Journal of the optical society of America*, vol. 40, no. 4, 1950.

[69] L. Van der Pauw, "A method of measuring the resistivity and the Hall coefficient on lamaellae of arbitrary shape," *Philips Technology Review*, vol. 26, no. 8, pp. 220–224, 1959.

[70] M. J. Erickson, *Surface and interface effects in nanoscopic metallic spin transport devices*. PhD thesis, University of Minesota, 2013.

[71] F. J. Jedema, A. T. Filip, and B. J. van Wees, "Electrical spin injection and accumulation at room temperature in an all-metal mesoscopic spin valve," *Nature*, vol. 410, no. 6826, pp. 345–348, 2001.

[72] M. Erekhinsky, A. Sharoni, F. Casanova, and I. K. Schuller, "Surface enhanced spin-flip scattering in lateral spin valves," *Applied Physics Letters*, vol. 96, no. 2, p. 022513, 2010.

[73] F. L. Bakker, A. Slachter, J.-P. Adam, and B. J. Van Wees, "Interplay of Peltier and Seebeck Effects in Nanoscale Nonlocal Spin Valves," *Physical Review Letters*, vol. 10, no. 105, 2010.

[74] D. McLean, *Grain boundaries in metals*. OXFORD at the Clarendon Press, 1957.

[75] F. Völklein, H. Reith, T. W. Cornelius, M. Rauber, and R. Neumann, "The experimental investigation of thermal conductivity and the Wiedemann-Franz law for single metallic nanowires.," *Nanotechnology*, vol. 20, no. 32, p. 325706, 2009.

[76] K. Tauber, M. Gradhand, D. V. Fedorov, and I. Mertig, "Extrinsic spin nernst effect from first principles," *Physical Review Letters*, vol. 109, no. 2, pp. 1–5, 2012.

[77] A. Slachter, F. L. Bakker, J.-p. Adam, and B. J. van Wees, "Thermally driven spin injection from a ferromagnet into a non-magnetic metal," *Nature Physics*, vol. 6, 2010.

[78] J. Flipse, F. L. Bakker, A. Slachter, F. K. Dejene, and B. J. van Wees, "Direct observation of the spin-dependent Peltier effect," *Nature Nanotechnology*, vol. 7, no. 3, pp. 166–168, 2012.

[79] F. K. Dejene, J. Flipse, G. E. W. Bauer, and B. J. Van Wees, "Spin heat accumulation and spin-dependent temperatures in nanopillar spin valves," *Nature Physics*, vol. 9, 2013.

[80] F. L. Bakker, J. Flipse, and B. J. Van Wees, "Nanoscale temperature sensing using the Seebeck effect," *Journal of Applied Physics*, vol. 111, no. 101, pp. 105119–17, 2012.

[81] A. Hojem, D. Wesenberg, and B. L. Zink, "Thermal spin injection and interface insensitivity in permalloy/aluminum metallic nonlocal spin valves," *Physical Review B*, vol. 94, no. 2, p. 024426, 2016.

[82] S. Garzon, I. Žutić, and R. A. Webb, "Temperature-dependent asymmetry of the nonlocal spin-injection resistance: Evidence for spin nonconserving interface scattering," *Physical Review Letters*, vol. 94, no. 17, pp. 1–4, 2005.

[83] S. Kasai, S. Hirayama, Y. K. Takahashi, S. Mitani, K. Hono, H. Adachi, J. Ieda, and S. Maekawa, "Thermal engineering of non-local resistance in lateral spin valves," *Applied Physics Letters*, vol. 104, no. 16, 2014.

[84] S. Hu and T. Kimura, "Anomalous Nernst-Ettingshausen effect in nonlocal spin valve measurement under high-bias current injection," *Physical Review B*, vol. 87, 2013.

[85] A. Pfeiffer, S. Hu, R. M. Reeve, A. Kronenberd, M. Jourdan, T. Kimura, and M. Klaui, "Spin currents injected electrically and thermally from higly spin polarized Co2MnSi," *Applied Physics Letters*, vol. 107, p. 082401, 2015.

[86] K. Das, F. Dejene, B. van Wees, and I. Vera-Marun, "Anisotropic Hanle line shape via magnetothermoelectric phenomena," *Physical Review B (R)*, vol. 94, p. 180403, 2016.

[87] V. Kuryliuk, A. Nadtochiy, O. Korotchenkov, C. Wang, and P. Li, "A model for predicting the thermal conductivity of SiO2-Ge nanoparticle composites," *Phys. Chem. Chem. Phys.*, vol. 17, pp. 13429–13441, 2015.

[88] F. Menges, *Scanning probe thermometry of nanosystems*. PhD thesis, ETH, 2015.

[89] F. Menges, H. Riel, A. Stemmer, and B. Gotsmann, "Quantitative Thermometry of Nanoscal Hot Spots," *Nano letters*, vol. 12, pp. 596–601, 2012.

[90] F. Menges, P. Mensch, H. Schmid, H. Riel, A. Stemmer, and B. Gotsmann, "Temperature mapping of operating nanoscale devices by scanning probe thermometry," *Nature Communications*, vol. 7:10874, 2016.

[91] A. Brown, M. W. Zemansky, and H. Boorse, "The superconducting and normal heat capacities of Niobium," *Physical Review*, vol. 91, no. 1, pp. 52–58, 1953.

[92] R. Worley, M. W. Zemansky, and H. Boorse, "Theoretical and experimental heat capacities of superconducting metals," *Physical Review*, vol. 87, no. 6, pp. 1142–1143, 1952.

[93] J. Jensen, W. Tuttle, R. Stewart, and H. Brechna, "Brookhaven national laboratory selected cryogenic data notebook, thermal conductivity of some solids," tech. rep., Brookhaven National Lab, 1980.

[94] F. Blatt, P. Schroeder, C. Foiles, and D. Greig, *Thermoelectric power of metals*. Plenum Press, New York, 1976.

[95] V. Das and N. Soundararajan, "Size and temperature effects on the Seeeck coefficient of thin bismuth films," *Physical Review B*, vol. 35, no. 12, pp. 5990–5996, 1987.

[96] D. Thornburg and C. Wayman, "Quantum and classical size effects in the thermoelectric power of bismuth films," *Philosophical magazine*, vol. 20, no. 168, pp. 1153–1161, 1969.

[97] C. Herschbach, M. Gradhand, D. V. Fedorov, and I. Mertig, "Enhancement of the spin Hall angle by quantum confinement," *Physical Review B - Condensed Matter and Materials Physics*, vol. 85, no. 19, p. 195133, 2012.

[98] M. Gradhand, D. V. Fedorov, P. Zahn, and I. Mertig, "Spin Hall angle versus spin diffusion length: Tailored by impurities," *Physical Review B*, vol. 81, no. 24, p. 245109, 2010.

[99] Y. Niimi, M. Morota, D. H. Wei, C. Deranlot, M. Basletic, A. Hamzic, A. Fert, and Y. Otani, "Extrinsic spin Hall effect induced by iridium impurities in copper," *Physical Review Letters*, vol. 106, no. 12, p. 126601, 2011.

[100] G. Mihajlovic, S. Erlingsson, K. Vyborny, J. E. Pearson, S. D. Bader, and A. Hoffmann, "Magnetic-field enhancement of nonlocal spin signal in $Ni_(80)Fe_(20)$/Ag lateral spin valves," *Physical Review B*, vol. 84, p. 132407, 2011.

[101] Y. Niimi, H. Suzuki, Y. Kawanishi, Y. Omori, T. Valet, A. Fert, and Y. Otani, "Extrinsic spin Hall effects measured with lateral spin valve structures," *Physical Review B*, vol. 89, p. 054401, 2014.

[102] L. O'Brien, D. Spivak, J. Jeong, K. Mkhoyan, P. Crowell, and C. Leigthon, "Interdiffusion-controlled Kondo suppression of injection efficiency in metallic nonlocal spin valves," *Physical Review B*, vol. 93, p. 014413, 2016.

[103] J. Watts, J. Jeong, L. O'Brien, K. Mkhoyan, P. Crowell, and C. Leigthon, "Room temperature spin Kondo effect and intermixing in Co/Cu non-local spin valves," *Applied Physics Letters*, vol. 110, p. 222407, 2017.

[104] K. Hamaya, T. Kurokawa, S. Oki, S. Yamada, T. Kanashima, and T. Taniyama, "Direct evidence for suppression of the Kondo effect due to pure spin current," *Physical Review B*, vol. 94, no. 14, p. 140401, 2016.

[105] T. Costi, L. Bergquvist, A. Weichselbaum, J. von Delft, T. Micklitz, A. Rosch, P. Mavropoulos, P. Dederichs, F. Mallet, L. Saminadayar, and C. Bäuerle, "Kondo decoherence: Finding the right spin model for Iron impurities in Gold and Silver," *Physical Review Letters*, no. 102, p. 056802, 2009.